VTT RESEARCH NOTES 2464

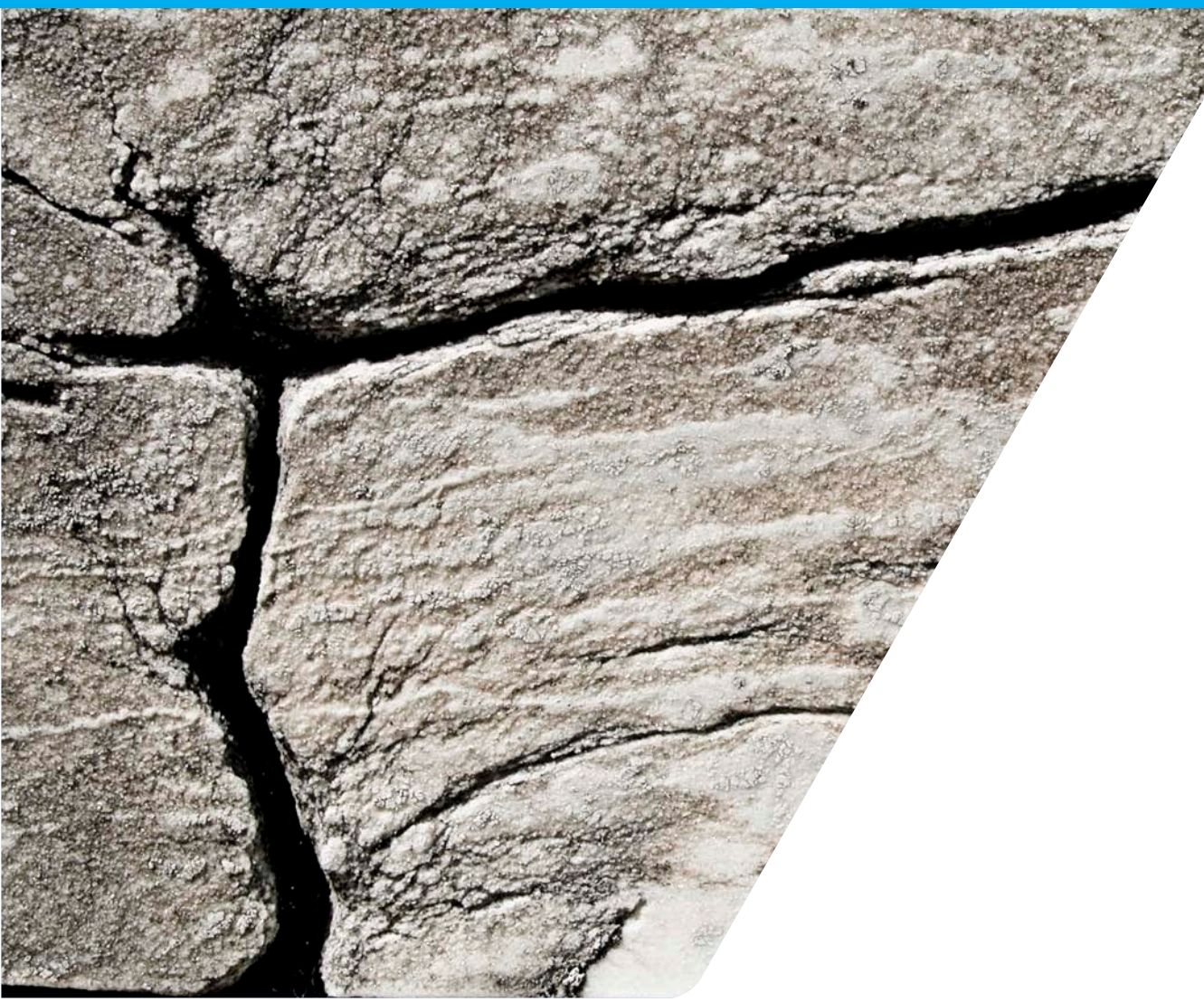

Antti Poteri

Solute transport and retention in fractured rock

VTT TIEDOTTEITA – RESEARCH NOTES 2464

Solute transport and retention in fractured rock

Antti Poteri

ISBN 978-951-38-7262-5 (soft back ed.)
ISSN 1235-0605 (soft back ed.)

ISBN 978-951-38-7263-2 (URL: http://www.vtt.fi/publications/index.jsp)
ISSN 1455-0865 (URL: http://www.vtt.fi/publications/index.jsp)

JULKAISIJA – UTGIVARE – PUBLISHER

VTT, Vuorimiehentie 5, PL 1000, 02044 VTT
puh. vaihde 020 722 111, faksi 020 722 7001

VTT, Bergsmansvägen 5, PB 1000, 02044 VTT
tel. växel 020 722 111, fax 020 722 7001

VTT Technical Research Centre of Finland, Vuorimiehentie 5, P.O. Box 1000, FI-02044 VTT, Finland
phone internat. +358 20 722 111, fax +358 20 722 7001

Text preparing Tarja Haapalainen

Edita Prima Oy, Helsinki 2009

Antti Poteri. Solute transport and retention in fractured rock [Aineiden kulkeutuminen ja pidättyminen rakoilleessa kalliossa]. Espoo 2009. VTT Tiedotteita – Research Notes 2464. 141 p.

Keywords solutes, transport, retention, flow path, bedrock, fractured rock, rock matrix, porosity, tracer tests, modelling, matrix diffusion

Abstract

This work reviews and compiles the analysis of tracer tests that were performed in the Äspö Hard Rock Laboratory in Sweden over a period of several years. The tracer tests were carried out in fractured rock at a depth of about 400 metres below the ground surface. The experimental programme progressed from a simple flow path in a single fracture to multiple flow paths through a network of fractures.

The modelling of the tracer tests on different scales shows that matrix diffusion is an important retention process of solute transport in fractured rock. The tracer breakthrough curves show indications of the diffusive mass exchange between mobile and immobile zones, although in many cases in situ tracer tests should be performed under boundary conditions that favour advective solute transport.

The analysis of the flow paths in a single fracture and in a network of fractures indicates that an increase in the complexity of the flow field and extending flow paths over several fractures does not introduce new retention processes. The same retention processes that are applicable for a single fracture can be applied over longer pathways that are composed of several different fractures. Modelling the tracer tests on a block scale indicates that this is the case even when the hydraulic structures along the flow path are geologically of different origin. Ultimately, the retention properties are governed by the average properties along the flow path.

The main outcome of the study is that the assessment of in situ solute retention properties requires adequate information on the immobile zones and flow paths. The heterogeneity of the immobile zone retention properties affects the effective tracer retention properties. The retention properties estimated for a given tracer test set-up cannot be directly transferred to another flow field without considering how the changes in the flow field will affect the contributions of the different immobile zones to the overall retention.

Antti Poteri. Solute transport and retention in fractured rock [Aineiden kulkeutuminen ja pidättyminen rakoilleessa kalliossa]. Espoo 2009. VTT Tiedotteita – Research Notes 2464. 141 s.

Avainsanat solutes, transport, retention, flow path, bedrock, fractured rock, rock matrix, porosity, tracer tests, modelling, matrix diffusion

Tiivistelmä

Tässä työssä analysoidaan Äspön kalliolaboratoriossa Ruotsissa usean vuoden aikana tehtyjä merkkiainekokeita. Merkkiainekokeet suoritettiin rakoilleessa kalliossa noin 400 metrin syvyydellä. Merkkiainekokeissa tutkittiin erilaisia virtausreittejä rakoilleessa kalliossa alkaen virtausreiteistä pitkin yksittäistä vettäjohtavaa rakoa ja päätyen virtausreitteihin useiden rakojen muodostamassa rakoverkostossa.

Merkkiainekokeiden mallinnus osoitti, että matriisidiffuusio on tärkeä pidättymismekanismi aineiden kulkeutumisessa rakoilleessa kalliossa. Merkkiaineiden läpitulokäyristä voidaan tunnistaa piirteitä, jotka viittaavat diffusiiviseen vuorovaikutukseen virtaavan ja paikallaan pysyvän huokoisveden välillä. Useissa tapauksissa kokeet jouduttiin kuitenkin suorittamaan pumppausnopeuksilla, joissa advektiivinen kulkeutuminen oli hallitsevaa.

Yksittäisessä raossa ja rakoverkostossa tapahtuneen kulkeutumisen analysointi osoittaa, että monimutkaisempi virtauskenttä tai kulkeutuminen usean raon kautta ei sinällään aiheuta kulkeutumiseen uusia pidättymismekanismeja. Samoja pidättymismekanismeja voidaan käyttää kuvaamaan kulkeutumista sekä yksittäisessä raossa että useista raoista koostuvalla pidemmällä reitillä. Lohkomittakaavassa tehdyt merkkiainekokeet osoittivat tämän olevan mahdollista, vaikka raot olisivat geologiselta alkuperältään erilaisia. Perimmiltään pidättymisominaisuudet voidaan kuvata keskimääräisillä ominaisuuksilla koko reitille.

Työn päätulos on havainto, että aineiden pidättymisen arviointi vaatii riittävän yksityiskohtaista tietoa itse virtausreitistä ja huokoistilavuuksista kulkeutumisreitin varrella. Heterogeenisuus huokoistilavuuden ominaisuuksissa vaikuttaa efektiivisiin pidättymisominaisuuksiin. Yhdelle kokeelliselle virtauskentälle määritettyjä pidättymisominaisuuksia ei voi soveltaa toisiin virtausoloihin ilman, että erikseen arvioidaan virtauksen vaikutusta pidättymiseen eri huokoisvyöhykkeissä.

Preface

This work is compiled from the modelling of three different tracer test campaigns carried out in the Äspö Hard Rock Laboratory, Sweden. The tracer tests studied include: Tracer Retention Understanding Experiments (TRUE) on a detailed scale (Poteri, 2001); TRUE Block Scale (Poteri, 2005), and TRUE Block Scale Continuation (Poteri, 2006).

The work has been carried out at VTT Technical Research Centre of Finland within the Nuclear Energy Research Field. I want to thank my present and former colleagues within the Nuclear Waste Management Research Group for numerous inspiring discussions. Especially I am grateful to Dr. Aimo Hautojärvi for his guidance and valuable comments. I also want to thank Professor Rainer Salomaa for his patience and encouragement during this work.

Espoo, October 2008 Antti Poteri

Contents

1. Introduction

Solute transport and retention in fractured rock has lately been under intensive study in many countries. Attention to transport phenomena in fractured crystalline rock has arisen mainly in connection with research into the geological disposal of nuclear waste.

The present plan for the geological disposal of spent nuclear waste is based on the encapsulation of the waste into corrosion-resistant copper canisters that are deposited in holes in the bedrock at a depth of approximately 500 m below the ground surface (Figure 1-1). The tunnels and the void spaces between the waste canisters and the walls of the deposition holes will be sealed with buffer and backfill materials that are based on clays, which will swell when saturated by water.

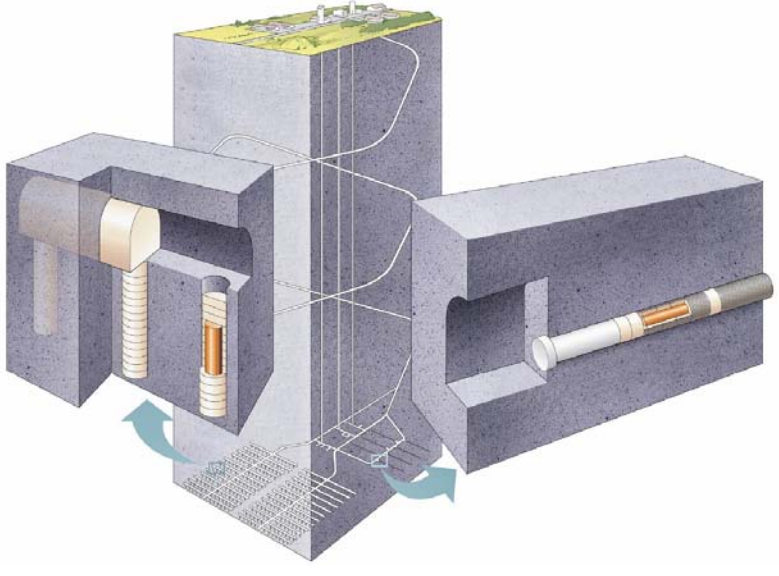

Figure 1-1. Illustration of the possible repository layout for a deep geological nuclear waste repository (from Posiva, 2008).

Advection along the groundwater flow is the only transport mechanism for radionuclides to escape from the underground repository. This means that an understanding of solute transport through fractures in rock and networks of fractures is the basis for the assessment of radionuclide migration through the geosphere.

This work summarises the modelling of tracer migration tests in natural fractures and fracture networks. The experimental data are based on a large number of tracer tests performed in in situ conditions in an underground research laboratory, the Äspö Hard Rock Laboratory, in Sweden. The Äspö Hard Rock Laboratory is located on the south-eastern coast of Sweden, close to the city of Oskarshamn (Figure 1-2). The experimental site is located in granitic fractured rock at a depth of about 400–500 m below the ground surface.

Groundwater flow in fractured rock takes place along the fractures. The rock between fractures is porous and saturated with groundwater, but in practice impermeable. Solute transport along fractures takes place by advection, but it is retarded by the interactions of the solute particles with the surrounding geological materials. The main retardation processes, which are also considered in this work, are sorption on the rock walls and diffusion into the immobile pore space between the fractures. Sorption is modelled as a reversible and linear equilibrium process. This is quite a simplified model of sorption, which is a collection of chemical and physical interactions between solute ions and rock walls. However, the modelled tracer tests were carried out using very dilute tracer solutions and the simplified sorption model based on the tracer-specific distribution coefficients has been verified by laboratory tests. Diffusion is modelled by a Fickian model, although the detailed structure of the immobile pores in the rock matrix is not completely known. The applicability of these basic assumptions is judged in the light of the modelled tracer tests.

The series of tracer experiments cover different levels of complexity, starting from a simple flow field in a single fracture over a short transport distance and ending in a complicated heterogeneous flow path through a network of fractures. All the experiments were conducted in the tracer test programme TRUE (Tracer Retention Understanding Experiments), which was initiated in 1994. The goal of the tracer test programme was to study processes in fractured rock that retard the transport of dissolved species. All the tracer tests were modelled, partly also as tasks of the international task force on groundwater flow and the transport of solutes of the Äspö HRL. The tracer tests were also modelled as blind predictions, so that the modellers were not aware of the experimental results

during the modelling. This approach highlights uncertainties that are connected to the modelling of the geosphere transport.

The first stage of TRUE (TRUE-1) was performed in a simple flow geometry and over a short transport distance (Winberg et al., 2000). Tracer tests were performed in a single fracture over a distance of about 5 m. Several different sorbing and non-sorbing tracers were used.

The second stage of TRUE (TRUE Block Scale) was carried out in a fracture network and over much longer transport distances than in TRUE-1 (Winberg et al., 2002). Path lengths calculated along the fracture planes of the local hydro-structural model vary from 16 m to about 97 m. One of the tests is also assumed to take place in a single fracture over a transport distance of 35 m. Generally, flow paths were estimated to involve at least 2–3 different fractures.

The third stage of TRUE (TRUE Block Scale Continuation) is a continuation of the second-stage tracer tests, but in another fracture network (Andersson et al., 2007). The overall objective of the third stage was to improve understanding of transport pathways on a block scale and to assess the effects of heterogeneity.

This work is organised in such a way that Section 2 gives the general characteristics of groundwater flow and solute retention in fractured rock and presents the physical and mathematical framework of the transport modelling. Section 3 gives experimental data and modelling results for the detailed scale tracer tests performed in a single fracture during the TRUE-1 phase of the tracer test programme. The modelling was carried out as blind predictions, applying site-specific laboratory data to the tracer retention properties. Section 4 discusses the modelling results and experimental data of the tracer tests performed in a network of fractures in transport paths measuring from ten or so to a hundred metres long. The modelling of this section aims to evaluate the tracer tests by applying alternative concepts of the immobile pore spaces and flow paths and taking advantage of the parameter variation in the modelling. Section 5 presents the modelling and experimental data from the last phase of the TRUE tracer tests. The experimental set-up repeats the tracer tests over a fracture network and long flow paths, but using another experimental site. The modelling of the tracer tests was focused to account for the influence of immobile zone heterogeneities on tracer retention. Finally, Section 6 summarises the results of the modelling of the tracer test on different scales.

Figure 1-2. Äspö Hard Rock Laboratory.

2. Transport characteristics of fractured rock

2.1 Groundwater flow

The nature of groundwater flow through fractured rock is determined by the structure of the rock. Fractured rock displays great heterogeneity in local permeability, and, correspondingly, great variability in local flow rates. Groundwater flow in fractured rock is characterised by three main properties: flow takes place mainly along the fractures, there are distinct flow paths, and the flow is channelised. Distinct flow paths follow from the large spread in hydraulic properties between different fractures. Channelling is governed by the heterogeneity of the local hydraulic conductivity inside the fractures. Figure 2-1 shows a conceptual illustration that is based on careful fracture conceptualisation and classification work performed in the Äspö Hard Rock Laboratory, Sweden (Mazurek et al., 2003).

The chances of collecting information on the properties of the fracture network are much better than those of collecting data on the individual fractures. Therefore, heterogeneity inside the fractures is usually treated by generic models and data. The parameterisation of the fracture network is based on measured data on the average properties of the fractures.

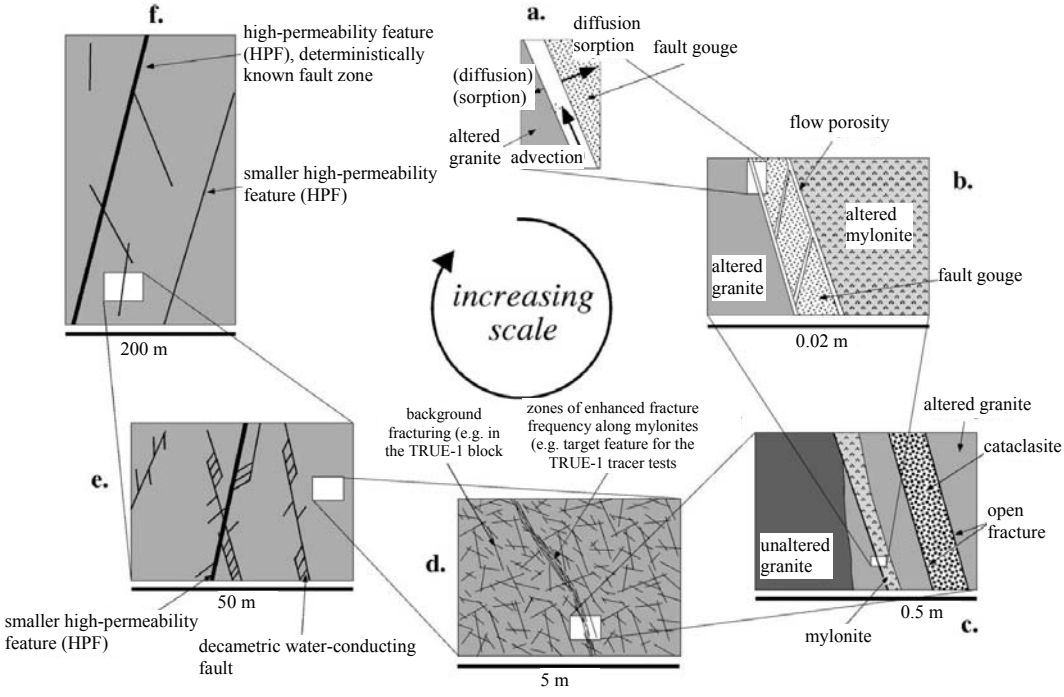

Figure 2-1. Conceptual illustration of the hydraulic features of fractured rock on different scales (from Mazurek et al., 2003).

Many in situ tracer experiments have been carried out in fractured rock during recent years. In many cases the flow cannot be described accurately without considering distinct flow paths. It also seems that the description of the solute transport and retention properties is even more dependent on the description of the preferential flow paths and dominant flow channels. Tracer experiments usually show fast initial arrival times, more than one peak in the breakthrough curves, and/or long tails and strong dependence on scale (Becker and Shapiro, 2000; Nordqvist et al., 1996; Tsang et al., 1991). Modelling has shown that the preferential flow and transport paths run over long distances and reduce mixing, especially in the case of high transmissivity variance (Nordqvist et al., 1996). All these observations underline the central role of the heterogeneity of fractured rock as a governing feature of the flow and transport properties.

In spite of the intensive work on in situ tracer experiments, there are untested properties that are important for the performance assessment of an underground repository. Many tests typically involve injection and pumping rates which are considerably higher than the flow rates occurring under natural conditions. The

transport distances of the tests are also much smaller than is required in the performance assessment. In practice, this kind of deficiency in the experimental work cannot be avoided, because the collection of the tracer in in situ experiments is not possible unless the experimental flow field does not exceed the natural background flow field. For the same reason tracer tests need to be carried out in well-conducting hydraulic features and over short distances, although retention takes place mainly in low-transmissive fractures in the performance assessment conditions.

2.1.1 Dual porosity

Fractured rocks are composed of porous but, in practice, impermeable rock matrix and water-conducting fractures. Groundwater flow takes place along fractures and networks of fractures are also the main transport pathway for the possible contaminants of groundwater. Impermeable but porous rock matrix is available for solute particles by diffusion (Neretnieks, 1980). The diffusion of the solute particles to the rock matrix can cause significant retention in the solute transport.

The Äspö TRUE project (Winberg et al., 2002) conceptualised immobile zones next to a water-conducting fracture on the basis of tracer test studies in fractured rock, field data, and numerical simulations of the tracer tests (Figure 2-2). Individual flow paths or transport channels are surrounded and filled by a multitude of different heterogeneities that will be of variable significance regarding solute retention, depending on the flow conditions.

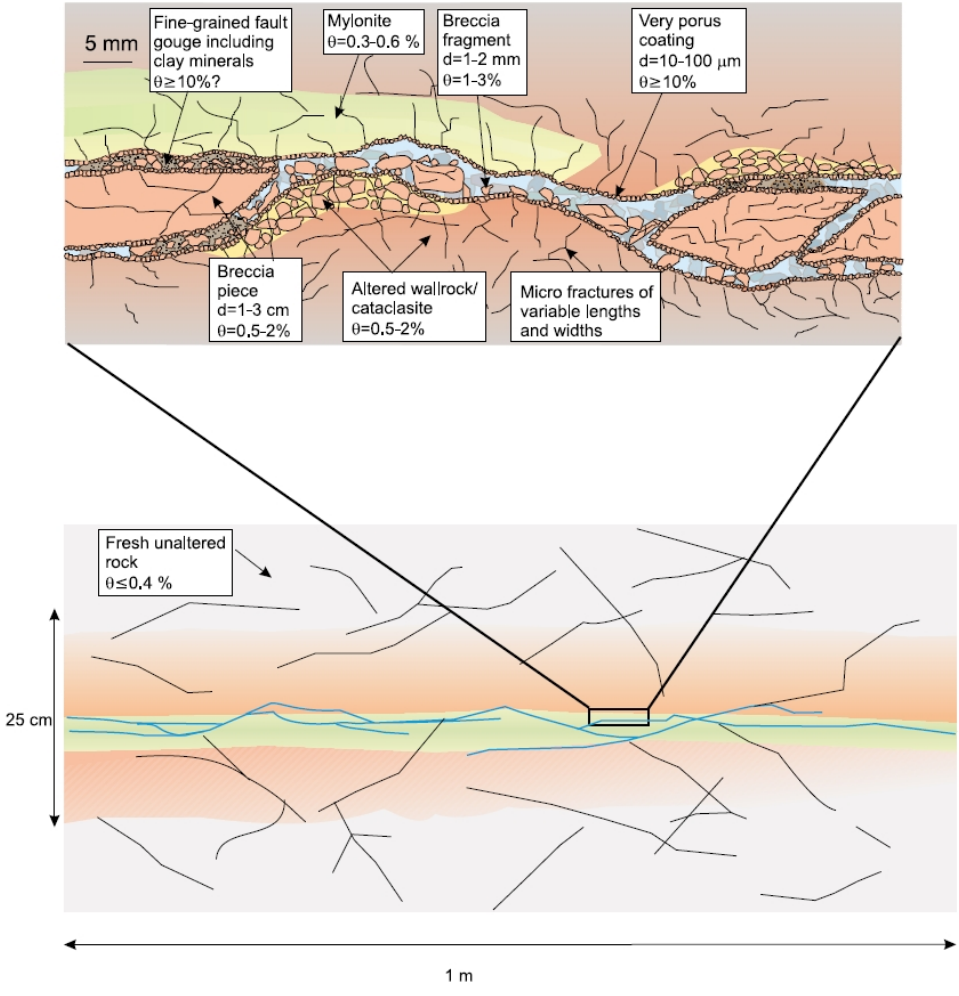

Figure 2-2. Illustration of the heterogeneity of the immobile zones next to the flow channels (from Winberg et al., 2002).

2.1.2 Distinct flow paths

There are indications that the hydraulic properties of fractured rock cannot be homogenised on any scale. Observations indicate that fractured rock follows a scaling behaviour that does not exhibit any characteristic length scale (Berkowitz, 2002). It has also been noticed that macroscopically fractured rocks are barely connected, i.e. they are close to the percolation limit, indicating that

fracture networks are fractal objects over the scale of observation (Sahimi, 1995). A geometrically well-connected network can also exhibit sparse preferential flow paths, and the network appears to be near the percolation threshold if the distribution of fracture conductivities is sufficiently broad. This gives rise to sparse networks of preferential flow paths, where only a few fractures dominate the hydraulic connection and transport properties of the rock mass (Berkowitz, 2002; Cacas et al., 1990a, 1990b). For example, at the Fanay-Augéres site in France, it was found that only about 0.1% of the fractures contributed to flow on a large scale (Long and Billaux, 1987).

Many in situ tracer experiments have been carried out in fractured rock during recent years. These experiments also indicate that solute transport cannot be described accurately without considering distinct flow paths. Tracer experiments usually show fast initial arrival times, more than one peak in the breakthrough curves, and/or long tails and strong dependence of the transport characteristics on the scale (Becker and Shapiro, 2000; Nordqvist et al., 1996; Tsang et al., 1991). Modelling has shown that preferential flow and transport paths may run over long distances and reduce mixing in the tracer plume, especially in the case of high transmissivity variance (Nordqvist et al., 1996).

2.1.3 Channelised flow

Many field experiments indicate that only a limited part of the volume within the fractures is open to fluid flow and solute transport. For example, Rasmuson and Neretnieks (1986) note that 90% of the fluid flow can occur through only 5–20% of the fracture plane. This channelling of the flow and solute transport has been proven to be true and to be an important process in fractured rock. It has been addressed by models (Bear et al., 1993; Nordqvist, 1995) and in several in situ experiments (Long and Billaux, 1987; Rasmuson and Neretnieks, 1986; Nordqvist et al., 1996). However, it is very difficult to collect site-specific quantitative data on channelling. Modelling is usually based on the prescribed degree of channelling or generic models of the fracture heterogeneity that appear to be reasonable.

2.2 Solute retention

In many cases, especially for strongly sorbing species, retention may dominate solute transport in such a way that the influence of advection on the solute

residence time distribution is negligible. The present study examines retention caused by sorption and matrix diffusion in a groundwater flow through fractured rock. The transport channels are described by streamtubes that are small enough to keep the solute concentration well mixed by molecular diffusion. Figure 2-3 shows a schematic illustration of how a flow path through the fractures is represented by a streamtube.

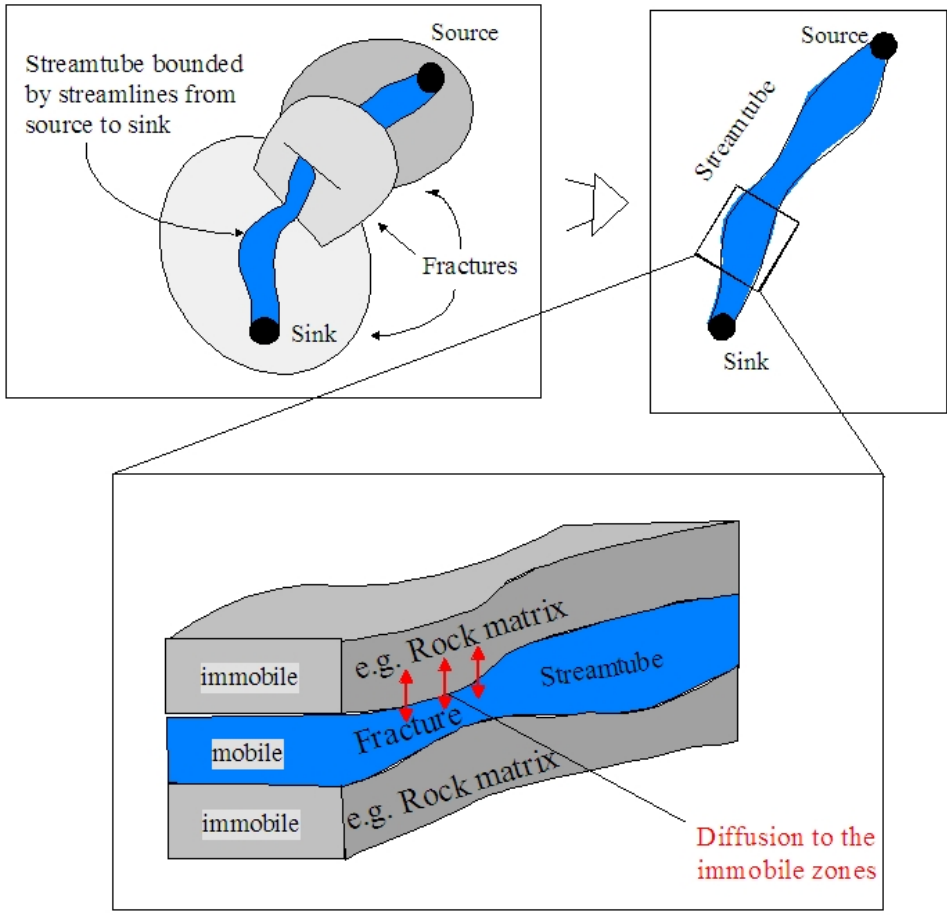

Figure 2-3. Schematic illustration of the streamtube (mobile pore space) and rock matrix (immobile pore space) next to the streamtube.

First, we consider a case of a single immobile zone along the flow path. Solute mass flux through a small control volume at an arbitrary location along the flow path is shown in Figure 2-4. The whole flow path can be envisaged as being composed of a series of successive control volumes.

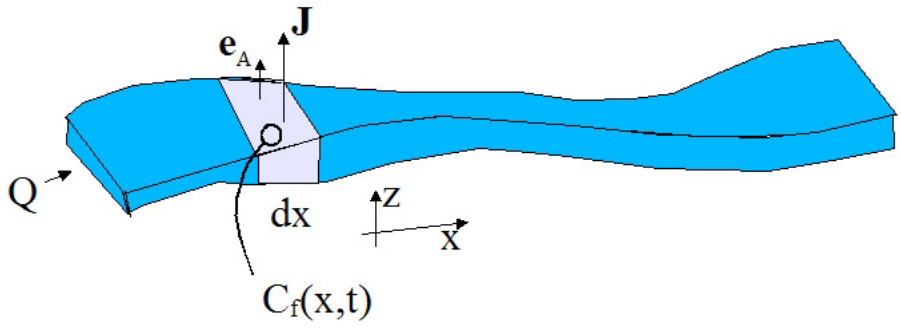

Figure 2-4. Streamtube and a control volume used to derive the solute mass balance equation along the streamtube (cf. Figure 2-3). The immobile zone is not shown in this figure in order to keep the picture clearer. Note that only one immobile zone is assumed at the top of the streamtube.

The solute mass balance equation written for the control volume in Figure 2-4 is

$$R_a \frac{\partial m(x,t)}{\partial t} = Q\left[C_f(x,t) - C_f(x+dx,t)\right] - \vec{J}(x,t;z=0)\cdot\vec{e}_A W(x)\,dx \quad (2\text{-}1)$$

where m is the solute mass in the control volume of the streamtube, C_f is the solute concentration in the control volume, the flow path (streamtube) is characterised by the width $W(x)$ and flow rate Q, and $\vec{e}_A$ is the outer normal of the control volume at the interface of the mobile and immobile pore spaces (i.e. at the diffusion interface). The factor R_a involves interactions that are described by the momentary equilibrium between the mobile and immobile phases of the solute particles (equilibrium sorption). This factor is defined by $R_a = 1 + 2K_a / 2b$, where $2b$ is the fracture aperture and K_a is the distribution coefficient of the concentration between the mobile and immobile phases. All properties may depend on the location along the flow path, except Q, which is constant, and in fact, defines the streamtube. The heterogeneity of the flow field and immobile zone properties along the flow path are taken into account.

Mass transfer by diffusion between the immobile and mobile zones is described by the mass flux $\vec{J}$ of Equation (2-2):

$$\vec{J}(x,t,z) = -D_e(x,z)\frac{\partial C_m(x,t,z)}{\partial z}\vec{e}_z, \quad (2\text{-}2)$$

where C_m is the solute concentration in the immobile pore space and D_e is the effective diffusion coefficient for the diffusion between the immobile and

mobile zones. In the immobile zone the solute mass transfer is governed by diffusion, as indicated in Equation (2-3):

$$R_p \frac{\partial C_m(x,t,z)}{\partial t} = D_p(x,z) \frac{\partial^2 C_m(x,t,z)}{\partial z^2}, \tag{2-3}$$

where D_p is the pore diffusivity and R_p is the retardation coefficient in the immobile zone. We require continuity of the solute concentration over the interface of the mobile and immobile zones. This means that

$$C_m(x,t,z=0) = C_f(x,t) \tag{2-4}$$

Note that Equation (2-4) is simplified by stating $C_m = C_f$ at $z = 0$ instead of $z = b(x)$. These are equivalent formulations because it is assumed that well-mixed conditions prevail in the fracture, i.e. C_f does not depend on z. In this case z measures the distance from the fracture wall, not from the centreline of the fracture.

Following Duhamel's theorem, the solute concentration in the immobile pore space can be written by Equation (2-5):

$$C_m(x,t,z) = \int_0^t g(x,t-\tau,z) C_f(x,\tau) d\tau, \tag{2-5}$$

where $g(x,t,z)$ is the solution for the solute one-dimensional diffusion in the immobile zone.

$$\begin{aligned} &\frac{\partial}{\partial z}\left(D_p(x,z) \frac{\partial g(x,t,z)}{\partial z} \right) = R_p \frac{\partial g(x,t,z)}{\partial t} \\ &g(x,0,0) = \delta(t) \\ &g(x,0,z) = 0, \ \ z > 0 \end{aligned} \quad . \tag{2-6}$$

Mass transfer to the immobile zone can be written using Equations (2-5) and (2-6) as

$$\begin{aligned} \vec{J}(x,t,z=0) &= -D_e(x,z) \int_0^t \frac{\partial g(x,t-\tau,z)}{\partial z} C_f(x,\tau) d\tau \ \vec{e}_z \\ &= \int_0^t j(x,t-\tau,z) C_f(x,\tau) d\tau \ \vec{e}_z \end{aligned}, \tag{2-7}$$

where

$$j(x,t,z=0) = -\varepsilon D_p(x,z)\frac{\partial g(x,t-\tau,z)}{\partial z} \quad . \tag{2-8}$$

The mass balance equation (1) can then be written using Equations (2-5) to (2-8) as

$$R_a \frac{\partial C_f(x,t)}{\partial t} = -\frac{Q}{W(x)2b(x)}\frac{\partial C_f(x,t)}{\partial x} - \frac{1}{2b(x)}\int_o^t j(x,t-\tau,z=0)\,C_f(x,\tau)\,d\tau \cdot \tag{2-9}$$

In order to examine some of the main properties of the transport equation it is not necessary to specify the structure and boundary conditions of the immobile zone, i.e. it is not necessary to solve Equation (2-3). The reason for this is that some of the main features of the solute transport (Equation (2-9) can be outlined without specifying the exact functional form of the diffusion flux, $j(x,t)$. However, we do need to take some further steps to solve Equation (2-9).

The Laplace transform of Equation (2-9) in respect of the time gives

$$R_a s\ \widetilde{C}_f(x,s) = -\frac{Q}{W(x)2b(x)}\frac{\partial \widetilde{C}_f(x,s)}{\partial x} - \frac{\widetilde{C}_f(x,s)}{2b(x)}\widetilde{j}(x,s,z=0), \tag{2-10}$$

where the tilde denotes the Laplace transformation and *s* is the variable of the Laplace transformed domain. Equation (2-10) can be solved for the initial condition of empty (no tracer) rock matrix and a sudden release of mass M_0 at the inlet of the flow path, i.e.

$$\begin{aligned} &C_f(x=0,t) = \frac{M_0}{Q}\delta(t) \rightarrow \widetilde{C}_f(x=0,s) = \frac{M_0}{Q} \\ &C_m(x,t=0,z) = C_f(x,t=0) = 0 \end{aligned} \tag{2-11}$$

Equation (2-12) gives a solution to Equation (2-10) using the initial conditions of Equation (2-11). The solute mass flux at the outlet of the flow path (x = L) is

$$\begin{aligned} \frac{\widetilde{\dot{m}}(L,s)}{M_0} &= \frac{Q}{M_0}\widetilde{C}_f(L,s) \\ &= \mathrm{Exp}\left[-s\int_0^L R_a\frac{W(x)2b(x)}{Q}\,dx - \int_0^L \frac{W(x)\widetilde{j}(x,s,z=0)}{Q}\,dx\right]. \\ &= \mathrm{Exp}\left[-s\,R_a\frac{V}{Q} - \int_0^L \frac{W(x)\widetilde{j}(x,s,z=0)}{Q}\,dx\right] \end{aligned} \tag{2-12}$$

It is noted from Equation (2-12) that, besides the advective delay (V/Q), the solution depends on the entity that is denoted here by the parameter *u*

$$u = \int_0^L \frac{W(x)\tilde{j}(x,s,z=0)}{Q} dx \,. \tag{2-13}$$

In the numerical simulations it may not be possible to follow the streamlines that bound the flow path. Instead, numerical models usually provide samples of the flow properties averaged over the model element size. In this case Equation (2-13) should be approximated by the equation

$$u = \int_0^L \frac{W'(x)\tilde{j}(x,s,z=0)}{Q'(x)} dx \,, \tag{2-14}$$

where W'(x)/Q'(x) is the measure of the local flow rate along the pathway. The accuracy of this approximation depends on the size of the model elements, i.e. the scale of the averaging. Preferably, the numerical approximation of the flow solution should not average the flow field over a much larger region than the solute particles will do by molecular diffusion along the flow path.

In the case of a homogeneous immobile zone (homogeneous rock matrix), Equation (2-14) simplifies to

$$u = \tilde{j}(s) \int_0^L \frac{W'(x)}{Q'(x)} dx \,, \tag{2-15}$$

where $\tilde{j}(s)$ describes diffusional coupling to the immobile zones and the flow-dependent part is represented by

$$u_F = \int_0^L \frac{W'(x)}{Q'(x)} dx \,, \tag{2-16}$$

where subscript "F" is used to denote the flow-dependent part of the parameter *u*. Equation (2-16) shows that the flow-dependent part is an integral along the flow path weighted by the inverse of the local 2D Darcy velocity in the fracture plane. In practice, this indicates that the individual conduits may have a significant role for the overall retention characteristics along the flow path.

3. Transport in a single fracture

3.1 Experimental site

Detailed scale tracer tests in a single fracture were performed at a depth of about 400 metres underground. The site was characterised by five cored boreholes. Four of them (KXTT1-KXTT4) were drilled from a niche made into the tunnel. The fifth borehole (KA3005A) intersects the experimental volume from a different direction (Figure 3-1). The distance from the experimental site to the tunnel of the research facility is about 20–30 m. The rock type around the experimental site is mainly Äspö diorite (Winberg, 1996).

The spatial extent of the tested fracture (denoted as Feature A) is estimated to be 10–30 m and the thickness from the borehole image processing log is 0.05–0.09 m (Winberg, 1996). Generalised radial flow analysis of the pressure-build up test data showed pseudo-spherical flow with flow dimensions of 2.4–3.0. The measured transmissivities from different boreholes intersecting Feature A vary between $1 \cdot 10^{-8}$ and $4 \cdot 10^{-7}$ m^2/s. A Leaky aquifer model applied to the interference test data gives transmissivities of between $6 \cdot 10^{-8}$ and $6 \cdot 10^{-6}$ m^2/s and shows good internal connectivity in Feature A (Winberg, 1996).

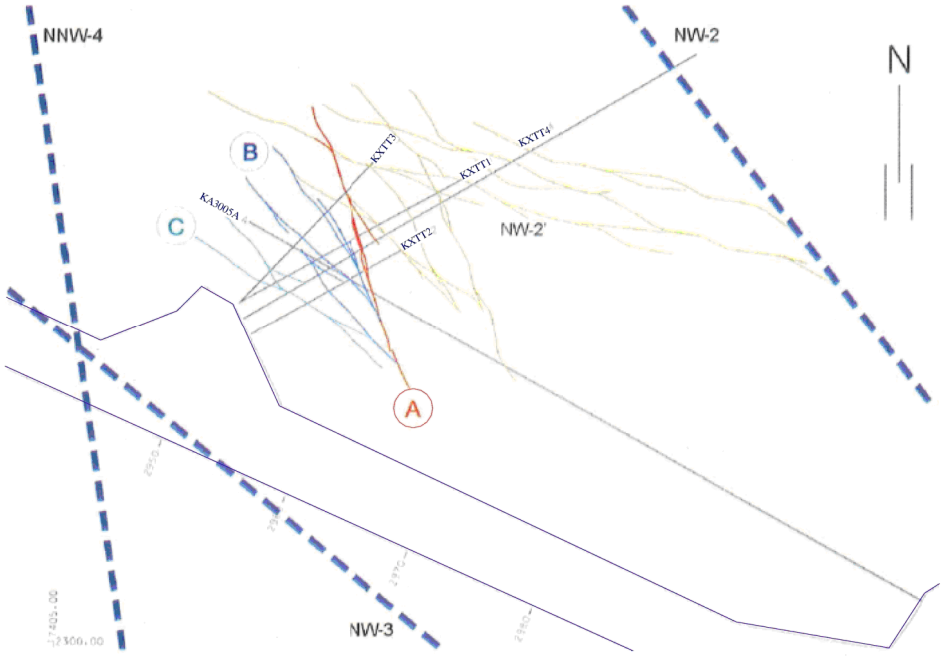

Figure 3-1. Structural geometrical model of the TRUE site (from Winberg et al., 2000, TR-00-07). The tracer tests of the TRUE 1 stage were performed in Feature A, which is indicated by the colour red.

3.2 Boundary conditions

The hydraulic head in Feature A was measured continuously. Measurements that were made before the tracer tests show a slow change in the background head field. On the average, the level of the hydraulic head decreased quite uniformly over Feature A. The head difference relative to KXTT3 (sink in the tracer tests) shows that the hydraulic head around KXTT2 decreased the most. The background head field favours using KXTT3 as the sink in the first tests. Later, the background head field is against the desired flow direction towards the sink in KXTT3.

The head differences between the instrumented parts of Feature A are quite small. They are less than 1.5 m, although the average level of the hydraulic head in Feature A decreased by about 8 m between December 1995 and 1998 (Winberg et al., 1998). The evolution of the measured head field in Feature A is presented in Figure 3-2.

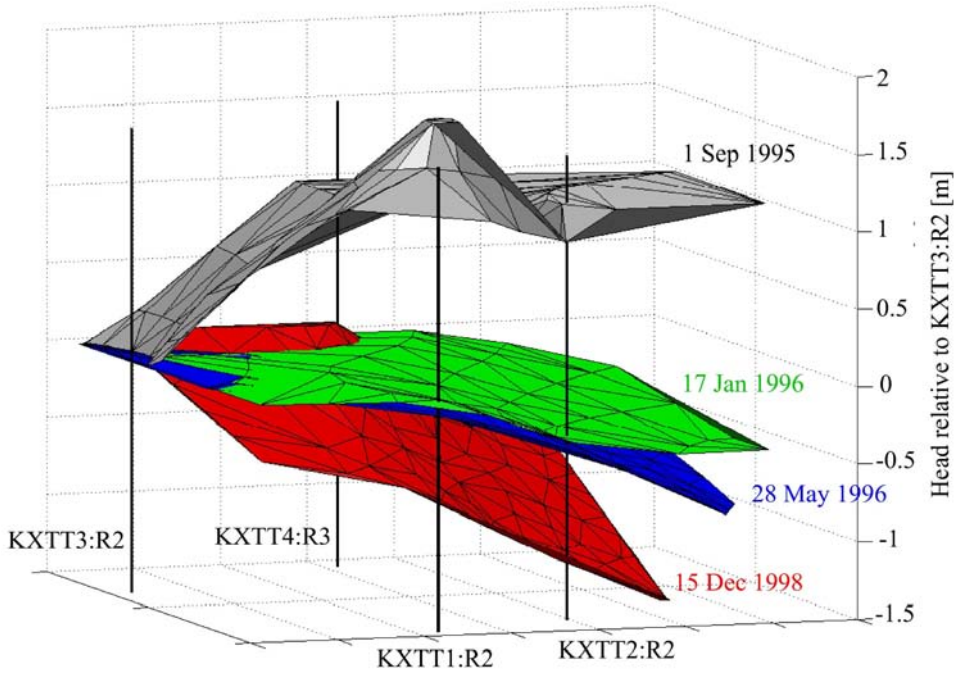

Figure 3-2. Evolution of the hydraulic head in Feature A. The hydraulic head is presented relative to the head in KXTT3:R2. The figure is based on the digitised equipotential lines from Andersson et al. (1997b) and Winberg et al. (1998).

3.3 Tracer tests

Nearly 20 different tracer tests were performed between 1995 and 1998. The majority of the tests were performed in a radially converging flow field using non-sorbing to weakly sorbing and moderately sorbing tracers (cf. Table 3-1).

The conclusion from the non-sorbing tracer tests was that the influence of the background field can be significant and the transmissivity structure of Feature A is quite complicated (Andersson et al., 1997b). The non-sorbing tracer tests were followed by sorbing tracer tests, STT-1, STT-1b, and STT-2, which were the target of the transport modelling. All the tests were performed using a large variety of different sorbing tracers. The tracers were injected simultaneously as a "tracer cocktail" and the borehole fluid was circulated internally in the injection borehole during injection. This ensured homogeneous tracer concentration in the source and enabled the tracer concentration to be monitored outside the borehole.

At the end of the injection the tracer solution in the circulation loop was replaced with unlabelled water to generate a sharp injection pulse. All the tests were performed under a radially converging flow field with no over-pressure in the tracer injection sections.

The STT-1 experiment contains 8 different tracers, both non-sorbing tracers (Uranine, HTO) and weakly to moderately sorbing tracers (^{22}Na, ^{47}Ca, ^{85}Sr, ^{133}Ba, ^{86}Rb, ^{137}Cs). Many of the tracers are radioactive, but the measurements have been corrected for radioactive decay and decay is not taken into account in the modelling.

The STT-1b experiment was performed along a different flow path to STT-1, using 10 different tracers, from non-sorbing tracers (Uranine, HTO) to weakly and moderately sorbing tracers (^{82}Br, ^{131}I, ^{22}Na, ^{42}K, ^{99m}Tc, ^{86}Rb, ^{85}Sr, ^{58}Co). All the tracers were injected simultaneously and the breakthrough curves have been corrected for radioactive decay.

The STT-2 experiment was performed in the same flow path as STT-1, but with a flow rate decreased by a factor of two to 200 ml/min. The number of different tracers was increased to 12 different simultaneously injected tracers. The tracers included non-sorbing Uranine, HTO (tritiated water), and sorbing tracers, ^{82}Br, ^{22}Na, ^{42}K, ^{47}Ca, ^{85}Sr, ^{99m}Tc, ^{131}Ba, ^{133}Ba, ^{86}Rb and ^{134}Cs. Radioactive decay was not modelled and the measurements were corrected to account for radioactive decay.

The geometry of the modelled sorbing tracer tests is presented in Figure 3-3 and technical details of the tests are presented in Table 3-2. A detailed description of the experimental set-up is given by Andersson et al. (1998) for STT-1, for STT-1b by Andersson et al. (1999a), and for STT-2 by Andersson et al. (1999b).

Table 3-1. Overview of the tracer tests performed during the TRUE-1 stage. DP tests were performed under a dipole flow geometry. All the others were performed in a radially converging flow field.

Test(s)	Date	Tracers	Reference
PTT	8/95	Uranine	Winberg (1996)
RC-1	1–2/96	Uranine Gd-DTPA Rhodamine WT Eu-DTPA Amino G Acid Ho-DTPA Eosin Y Tb-DTPA	Andersson (1996)
DP1-DP4	6/96	Uranine Amino G Acid Gd-DTPA	Andersson et al. (1997b)
RC-2, DP-5, DP-6	9–10/96	Uranine Amino G Acid	Andersson et al. (1997a)
PDT-1, PDT-2	4–5/97	Uranine Amino G Acid	Andersson and Wass (1998)
PDT-3	6–7/97	Uranine HTO ^{82}Br ^{24}Na	Andersson and Wass (1998)
STT-1	7–9/97	Uranine HTO ^{22}Na ^{85}Sr ^{86}Rb ^{47}Ca ^{133}Ba ^{137}Cs	Andersson et al. (1998)
PDT-4	11/97	Uranine	
STT-1b	12/97–3/98	Uranine HTO ^{22}Na ^{86}Rb ^{85}Sr ^{42}K ^{58}Co	Andersson et al. (1999a)
RC-3	4/98	Uranine	Andersson et al. (1998)
STT-2	5–8/98	Uranine HTO ^{22}Na ^{47}Ca ^{85}Sr ^{131}Ba ^{133}Ba ^{86}Rb ^{134}Cs	Andersson et al. (1999b)

Table 3-2. Modelled sorbing tracer tests of the TRUE-1 stage.

	Injection		Extraction		
Test	**Borehole: section**	**Injection rate [ml/min]**	**Borehole: section**	**Extraction rate [ml/min]**	**Draw-down [m]**
STT-1	KXTT4:R3	~ 0.7	KXTT3:R2	400	6–9*)
STT-1b	KXTT1:R2	~ 1	KXTT3:R2	400	9–12*)
STT-2	KXTT4:R3	~ 0.5	KXTT3:R2	200	6–8

*) Hydraulic head difference between injection and withdrawal sections.

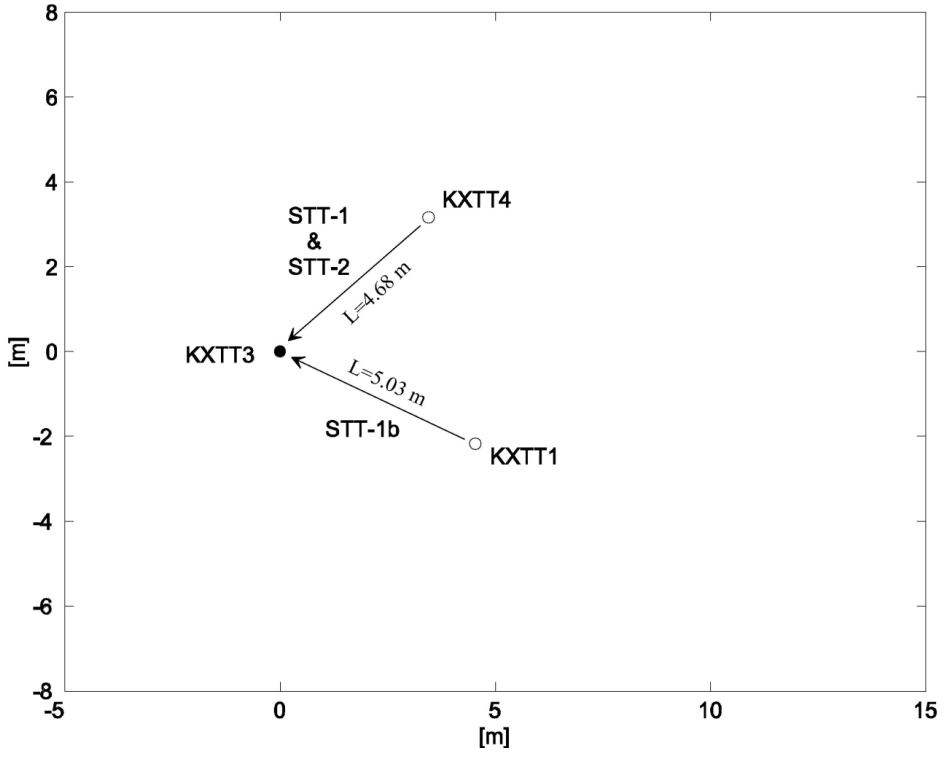

Figure 3-3. Experimental geometry of the sorbing tracer tests STT-1, STT-1b, and STT-2. Filled circle indicates tracer withdrawal borehole and open circles indicate tracer source boreholes.

3.4 Modelling

Two different models were applied to model advection. Both models share the same retention model based on sorption and matrix diffusion. The first two tests, STT-1 and STT-1b, were modelled by assuming flow along a two-dimensional heterogeneous fracture (the fracture model). The last test, STT-2, was modelled by assuming solute transport through an explicit transport channel (the channel model).

All the STT tracer tests were modelled as blind predictions. The advective field in the STT-1 and STT-1b tests was calibrated using data from earlier non-sorbing tracer tests. The blind predictions in STT-1 and STT-1b were based on commonly applied values for the rock matrix porosity (0.005) and density (2300 kg/m^3). Sorption properties and diffusion coefficients were selected on the basis of the recommented values for the Äspö conditions (Andersson et al., 1997c). The advective field for the STT-2 test was scaled from the advective field of the STT-1 test. The retention data applied in the STT-2 predicitions were calibrated using the results from STT-1 and STT-1b and they were not based on laboratory data on the rock matrix properties.

3.4.1 Advective transport using the fracture model

The fracture model is a two-dimensional numerical model for a planar and hydraulically heterogeneous fracture. Tracer advection is calculated by particle tracking in the numerically solved flow field. Retention processes (matrix diffusion, diffusion into stagnant zones of the flow field, and sorption) are modelled analytically, using the particle tracked advective residence time distribution as a basis.

The fracture model was applied to predict the outcomes of the STT-1 and STT-1b tests. The model includes only Feature A, i.e. the fracture used in the tracer test. The influence of all the surrounding fractures is taken into account by the boundary conditions at the boundary of the modelled fracture. The following assumptions were applied in the modelling:

- The flow field is two-dimensional and the tracer concentration is well mixed over the aperture of the fracture.
- The tracer tests take place under steady state flow conditions.
- The tracer retention processes are matrix diffusion and sorption.

- Other fractures that possibly intersect the tested fracture do not directly influence tracer transport or retention.
- The background flow field is represented by a constant gradient of the hydraulic head that is applied at the outer boundary of Feature A.
- The transmissivity of Feature A is represented by a heterogeneous log-normal transmissivity field with an isotropic and constant correlation length.
- The transport aperture is scaled from the local hydraulic aperture by a constant factor (C_v). Small-scale heterogeneity and diffusional mixing in the flow field are represented by hydrodynamic dispersion. Hydrodynamic dispersion and C_v were calibrated on the basis of the earlier non-sorbing tracer tests (Poteri and Hautojärvi, 1998).

The spherical correlation function of the transmissivity distribution is defined by Equation (3-1):

$$r(x) = \begin{cases} 1 - \dfrac{3|x|}{2l} + \dfrac{1}{2}\left(\dfrac{|x|}{l}\right)^3 & 0 \le x \le l \\ 0 & \text{otherwise,} \end{cases} \qquad (3\text{-}1)$$

where $r(x)$ is the correlation coefficient between two points, x is the distance between the points, and l is the correlation length. Detailed data on the correlation structure of the transmissivity in the tested fracture are not available. The correlation length of 0.4 metres applied in the modelling is based on interpretations of other fractures that are like the tested Feature A (Winberg, 1996).

The transmissivity field was calibrated using drawdown data from ten different tracer tests: RC-1, DP-1, DP-2, DP-3, DP-4, RC-2, DP-5, DP-6, PDT-1, and PDT-2. The mean $\log_{10}$ transmissivity is $\mu = -6.67$ and the variance of the $\log_{10}$ transmissivity is $\sigma = 1.0$. The experimental results of the PDT-3 test were used to calibrate the ratio of the transport aperture to the flow aperture to $C_v = 11$ and the dispersion coefficient to $D = 10^{-4}$ m^2/s. The applied hydraulic and transport properties of Feature A are collected in Table 3-3.

The particle tracking is based on the fixed spatial step length and the varying length of the step in the time domain. Hydrodynamic dispersion is modelled as a random Brownian motion in two dimensions. The length of the dispersion step is calculated according to the equation

$$\delta = N(0,1)\sqrt{2D\Delta t}\ , \tag{3-2}$$

where *N(0,1)* is the normal probability function of zero mean and unit variance, D is the dispersion coefficient, and Δt is the length of the time step.

Both the STT-1 and STT-1b tests were simulated using 30 different realisations of the fracture transmissivity field. The 30 simulated realisations were selected from among 799 tested realisations, using the drawdown data of the earlier tracer tests as a criterion. The modelling domain is 11 by 15 metres and the mesh contains 15,120 square elements that are about 0.1 x 0.1 m^2 in size. The modelling region is positioned in such a way that the distance from the pumping borehole to the boundary of the model is at least 5 metres (see Figure 3-4).

The advective residence time distributions are based on particle tracking simulations using 2000 different particles. The breakthrough curves for different tracers are calculated by completing advective residence time distributions analytically with retention by sorption and matrix diffusion and convoluting the solute residence time distribution with the measured tracer injection source term.

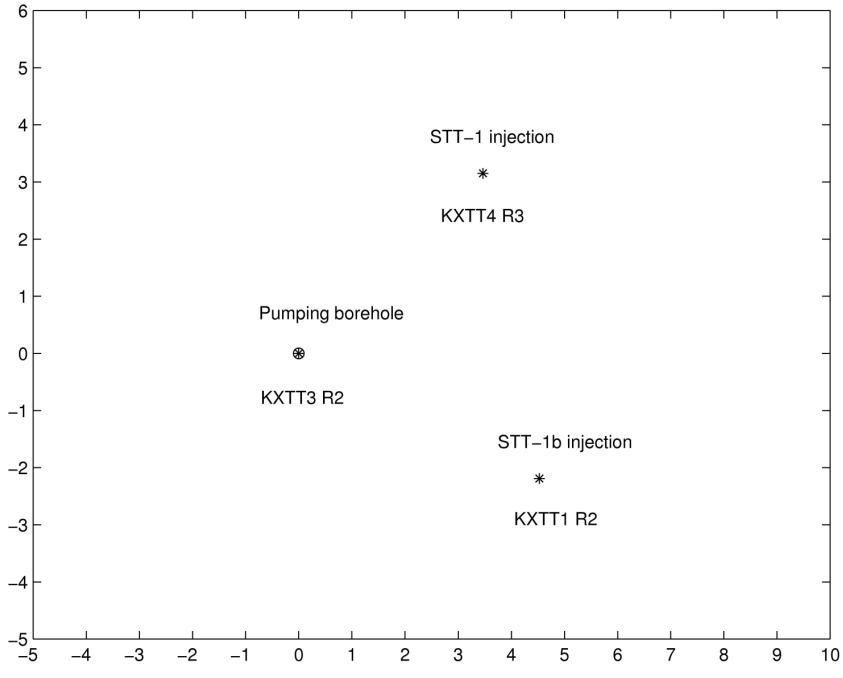

Figure 3-4. Modelling domain applied in the numerical simulations of the STT-1 and STT-1b tests.

Table 3-3. Hydraulic and transport properties of Feature A applied in the modelling of the STT-1 and STT-1b tests.

Parameter		Value	
Correlation length of the transmissivity distribution		0.4	m
Transmissivity distribution (log-normal)	mean log10(T)	-6.67	m^2/s
	std log10(T)	1.0	m^2/s
Transport vs. hydraulic aperture ratio (Cv)		11	
Hydrodynamic dispersion		10^{-4}	m^2/s

3.4.2 Advective transport using the channel model

The modelling of the advective transport in the STT-2 test was based on the assumption that only a few flow channels will dominate the tracer transport. The transport processes considered in the channel model were advection and diffusional mixing in the flow field. It is assumed that tracer concentration is well mixed in the direction of the fracture aperture. However, a concentration gradient may exist in the fracture plane, i.e. transverse to the transport channel in the direction of the channel width. A triangular velocity profile is assumed over the channel width (cf. Figure 3-5).

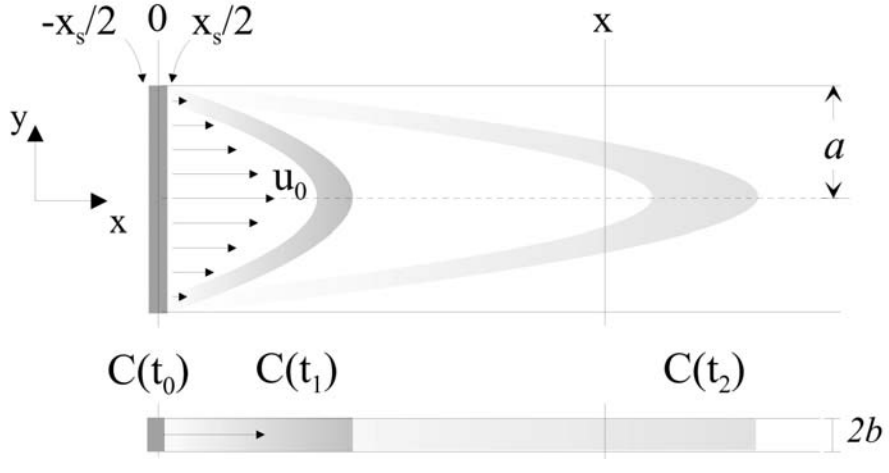

Figure 3-5. Advection and diffusion of solute in the transport channel. Width of the channel is 2*a* and aperture of the fracture is 2***b*** (from Hautojärvi and Taivassalo, 1994).

The mean concentration across the transport channel can be solved analytically. Hautojärvi and Taivassalo (1994) give the mean concentration

$$C_m = \frac{1}{2}\left(erf\left[\frac{\frac{1}{2}X_S + X + \xi_1}{2\sqrt{\xi_2}}\right] + erf\left[\frac{\frac{1}{2}X_S - X - \xi_1}{2\sqrt{\xi_2}}\right]\right);$$

$$\xi_1 = -\frac{1}{2}\tau; \quad \xi_2 = \left(\frac{1}{(Pe)^2} + \frac{1}{120}\right)\tau - 8\sum_{n=0}^{\infty}\frac{1 - e^{-(2n+1)^2\pi^2\tau}}{(2n+1)^8\pi^8}; \tag{3-3}$$

$$\tau = \frac{D\,t}{a^2}; \quad X = \frac{D\,x}{a^2 u_0}; \quad X_S = \frac{D\,x_S}{a^2 u_0}; \quad Pe = \frac{a\,u_o}{D}$$

where D is the molecular diffusion coefficient, a is the width of the velocity profile, x_S is the initial width of the tracer plume (see Figure 3-5), u_0 is the maximum flow velocity, t is the time, and x is the position along the channel. The hydraulic and geometrical properties of the flow channel that were applied in the modelling are collected in
Table 3-4.

Table 3-4. Hydraulic and geometrical properties of the transport channel used in the simulation of the STT-2 test.

Parameter	**Value**	
Flow rate through the transport channel (fitted from the injection curve)	25	ml/h
Maximum transport velocity in the channel	$5.6\cdot10^{-4}$	m/s
Channel length	4.68	m
Channel width	0.05	m
Coefficient of the molecular diffusion	$2.4\cdot10^{-9}$	m^2/s

3.4.3 Modelling of retention

The retention processes under consideration, sorption and matrix diffusion, were taken into account analytically. Equation (2-16) shows that retention depends on the average of the inverse of the two-dimensional Darcy velocity along the flow path, i.e. WL/Q, where L is the length of the transport path, Q is the flow rate,

and W is the average width of the path. The distribution of the WL/Q over the transport path was estimated on the basis of the simulated advective water residence time distribution. It is assumed that variability in the advective water residence times is caused by variation in the flow rate in the transport channel of the fracture plane. The tracer residence time distribution in the case of an infinite immobile zone and an advective water residence time of t_w can be written as

$$\dot{m}_{MD}(t,t_w) = \frac{U\,t_w}{\sqrt{\pi(t-R_a t_w)^3}} e^{-\frac{U^2 t_w^2}{t-R_a t_w}}, \tag{3-4}$$

where

$$U = \frac{\sqrt{D_e \varepsilon R_p}}{2b}, \tag{3-5}$$

D_e is the effective diffusion coefficient for diffusion to the immobile zone, ε is the immobile porosity, R_p is the retention coefficient in the immobile zone, R_a is the surface sorption, and $2b$ is the fracture aperture. Integrating over the advective water residence time distribution, $f_{AD}(t)$, gives the tracer residence time distribution:

$$\dot{m}_{tot}(t) = \int_0^t f_{AD}(t_w)\dot{m}_{MD}(t,t_w)dt_w, \tag{3-6}$$

where $\dot{m}_{MD}(t,t_w)$ is defined in Equation (3-4).

The STT-2 model (the channel model) applied a slightly different approach to the STT-1 and STT-1b models. The same retention processes were considered, but it was assumed that the immobile zones are in the stagnant pools of the flow field, whereas the modelling of the STT-1 and STT-1b tests assumed that the immobile zones are in the rock matrix (Figure 3-6). This means that matrix diffusion is represented by a constant $u = \sqrt{D_e \varepsilon R_p}\,WL/Q$ instead of the varying u-value (Equation (3-5)) applied in the modelling of the STT-1 test.

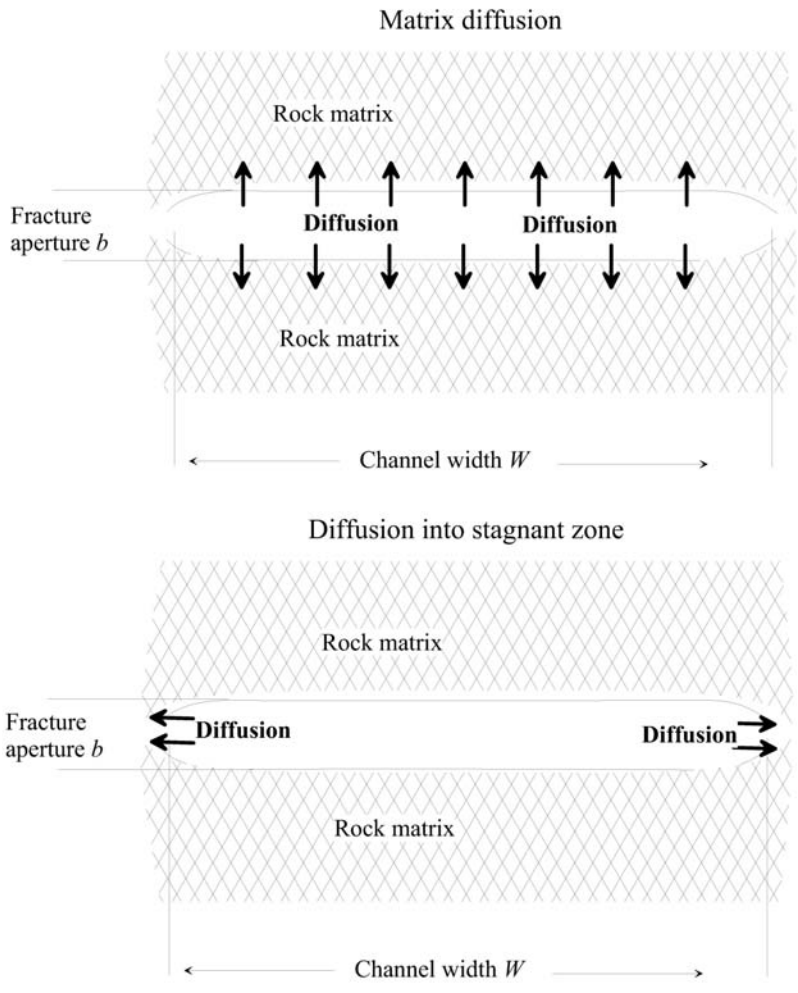

Figure 3-6. In the STT-1 and STT-1b models diffusion is to the rock matrix. In the STT-2 model diffusion is to the stagnant zones of the flow field.

All the STT tracer tests were modelled as blind predictions. The modelling of the STT-1 and STT-1b tests was performed by using commonly applied values for retention properties, e.g. rock matrix porosity and K_d's. The STT-2 modelling was based on retention parameters that were calibrated using the measured breakthrough curves of the preceding STT-1 test. The STT-1 test was performed in the same flow path as the STT-2 test, but using a different flow rate. The calibrated retention parameters include the surface retardation coefficients (R_a) and the *u*-parameter values (Equation (5-6)) that control the strength of the matrix diffusion.

The results of the calibration are presented in Figure 3-7 and Figure 3-8. The pumping flow rate of the STT-2 test was only half of the pumping rate applied in the STT-1 test. The fitted *u*-parameter values of the STT-1 test were scaled to represent the flow conditions of the STT-2 test before they were applied in the modelling. The decay of the tracer concentration in the injection borehole section indicates that the flow rate in the transport channel was about 40 ml/h in the STT-1 tests and, correspondingly, it was about 25 ml/h in the STT-2 test. On the basis of the difference in the flow rates, the fitted *u*-parameters of the STT-1 test were multiplied by a factor of 40/25 before they were applied in the modelling of the STT-2 test. The retardation coefficients, *u*-parameter values, and the termination times of the tracer test simulations used in the modelling of the STT-2 test are presented in Table 3-5.

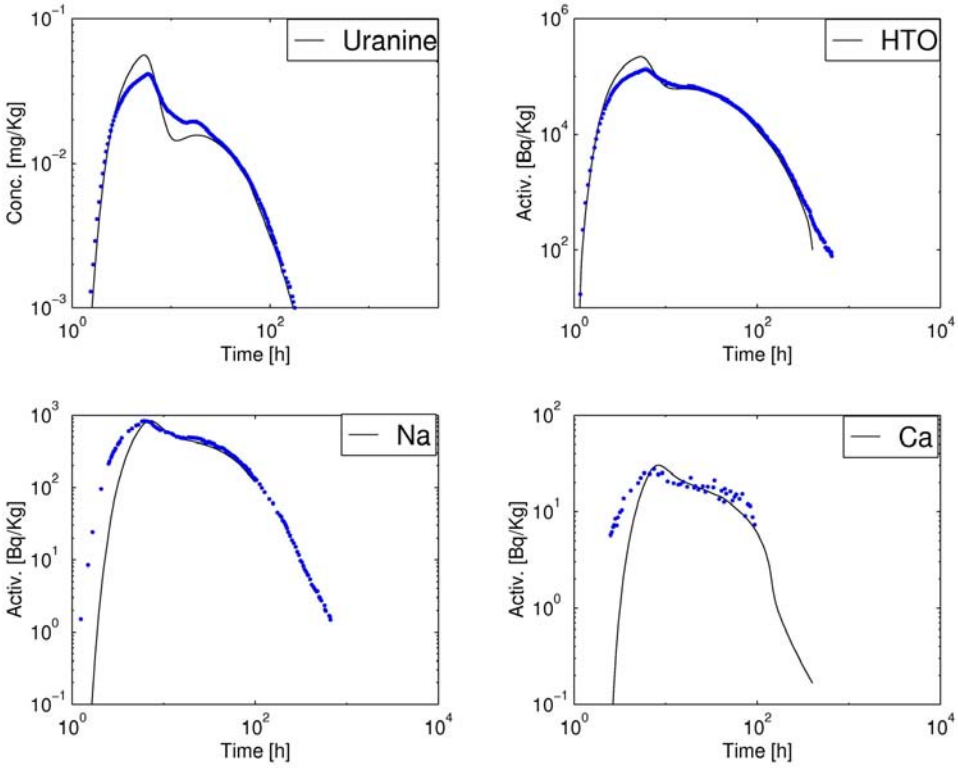

Figure 3-7. Simulation of the STT-1 test for Uranine, HTO, Na-22, and Ca-47 with the channel model to calibrate the transport parameters of the STT-2 test. Simulation results are presented using solid lines and experimental results using dots.

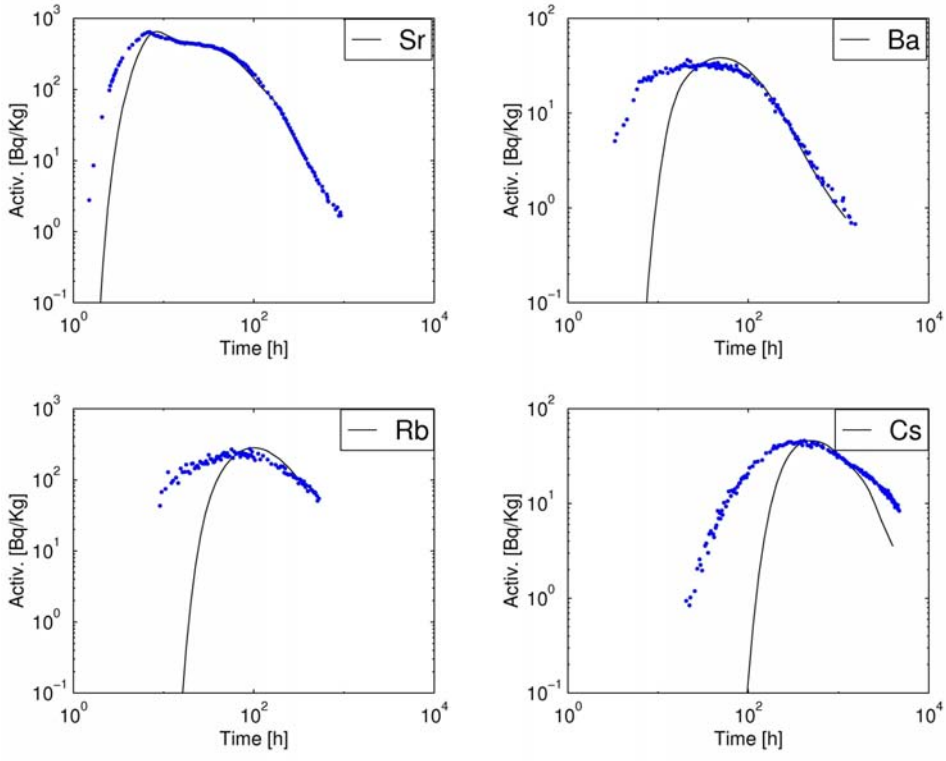

Figure 3-8. Simulation of the STT-1 test for Sr-85, Ba-133, Rb-86, and Cs-137 with the channel model to calibrate the transport parameters of the STT-2 test. Simulation results are presented using solid lines and experimental results using dots. The flow field is described by one effective u-parameter value and flow velocity that is not able to fully reproduce the very early parts of the breakthrough curves.

Table 3-5. Surface retardation coefficient R_a, *u*-parameter values, and termination times of the simulations that were applied in the modelling of the STT-2 test.

Tracer	*u* [sqrt(h)]	R_a [-]	Termination time [h]
HTO	0.28	1	641
Uranine	0.28	1	886
Na-22	1.8	1.1	3078
Ca-47	1.9	1.4	458
Sr-85	2.6	1.1	3078
Ba-131	6.1	3.0	1130
Ba-133	6.1	3.0	3078
Rb-86	9.6	8	1322
Cs-134	21	46	3078

3.5 Modelling results

STT-1 test

Simulation results are presented for the median breakthrough curves of the simulated 30 different realistions. The simulated and experimental breakthrough curves are presented in Figure 3-10 and Figure 3-11. The tracers can be divided into three different classes: non-sorbing tracers (HTO, Uranine, Na-22, Ca-47, and Sr-85), weakly sorbing tracers (Rb-86 and Ba-133), and a strongly sorbing tracer (Cs-137). Generally, the model predictions show a steeper rise and sharper peak in the tracer residence times than was observed in the experiment. The modelled tracer residence time distributions show less retention than the experimental tracer residence time distributions, especially for the sorbing tracers. The greatest discrepancy between the simulations and experimental results is for Rb-86.

A comparison of the tracer retention and corresponding sorption data indicates that the deviations between different tracers could be caused by surface sorption. The tailings of the measured breakthrough curves do not show the $\sim t^{-3/2}$ slope that is characteristic of matrix diffusion. The tracer source terms are truncated after a few hours, but full control of the tailings of the source terms has not succeeded (Figure 3-9). It is possible that the some of the retention characteristics cannot be seen because of the dispersed tailings of the source terms.

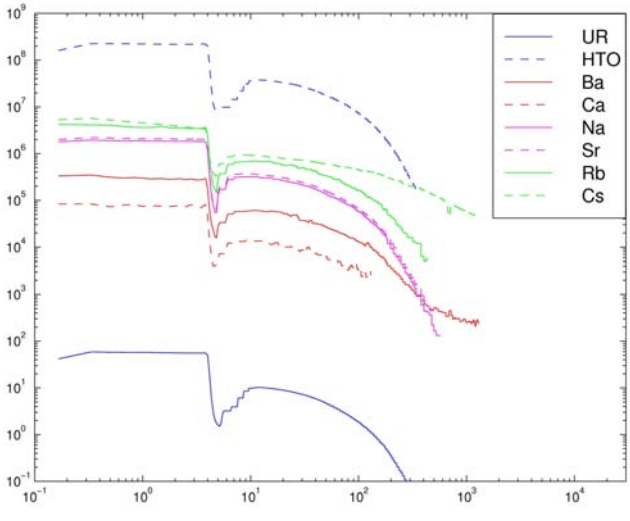

Figure 3-9. Measured tracer source functions at the beginning of the STT-1 flow path.

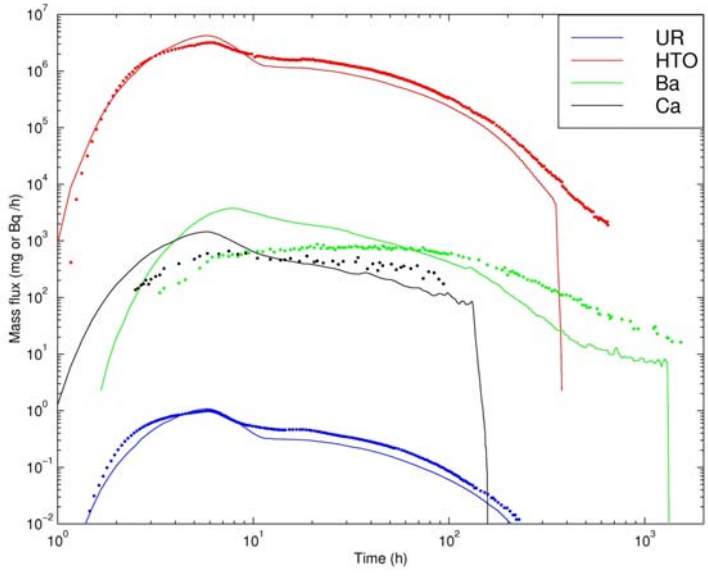

Figure 3-10. Measured breakthrough curves for Uranine, tritiated water (HTO), Ba-133, and Ca-47 in the STT-1 test. Simulation results are presented with solid lines and the corresponding measured breakthrough curves with dots.

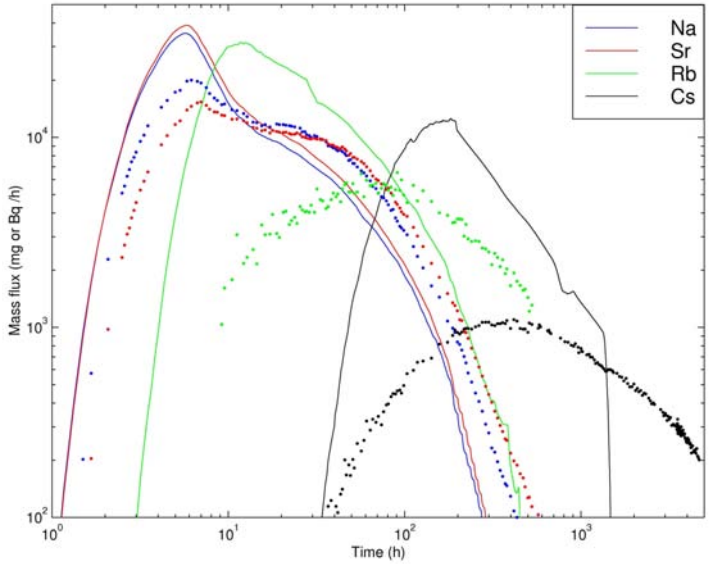

Figure 3-11. Measured breakthrough curves for Na-22, Sr-85, Rb-86, and Cs-137 in the STT-1 test. Simulation results are presented with solid lines and the corresponding measured breakthrough curves with dots.

STT-1b test

The modelling does not show any great difference between the STT-1 and STT-1b tests. There are good reasons for this. The same sorption data were applied in the modelling of both tests, the transmissivity and flow fields are the same, the lengths of the flow paths are also approximately the same (the distances between the injection and withdrawal boreholes are 4.68 m and 5.08 m), and the boundary conditions applied are the same in both tests.

Measured tracer residence time distributions show that only the transport of Rb-86 is retarded. The residence times for all the other tracers are more or less similar. The greatest discrepancy between the simulated and experimental results is for Rb-86. It seems that the sorption applied in the STT-1 and STT-1b tests does not provide as much retention as was measured in the tests. However, the tailings of the breakthrough curves do not show a $\sim t^{-3/2}$ slope, as was also the case in the STT-1 test. This can be an indication that the flow rates were too high in the STT-1 and STT-1b tests and matrix diffusion is not able to provide much retention in these tests. The tailing of the tracer source term at the beginning of the flow paths is also quite dispersed in the STT-1b test and this may complicate the observation of the retention processes (Figure 3-12 and Figure 3-13).

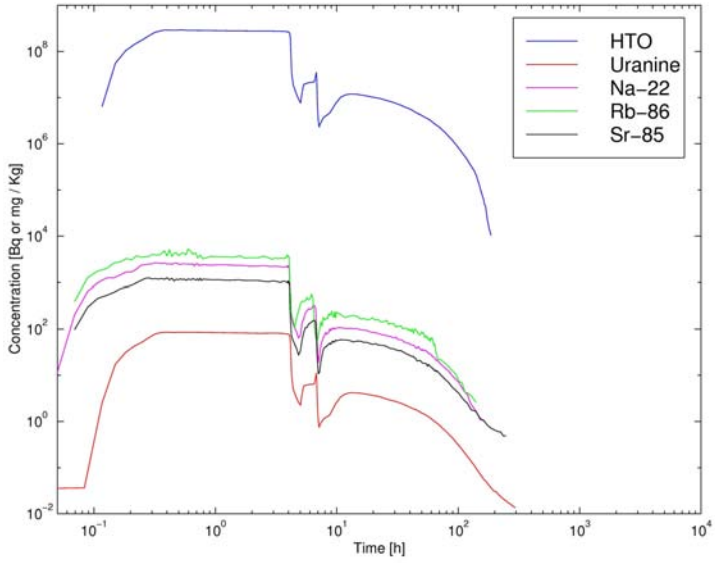

Figure 3-12. Measured tracer source functions at the beginning of the STT-1b test.

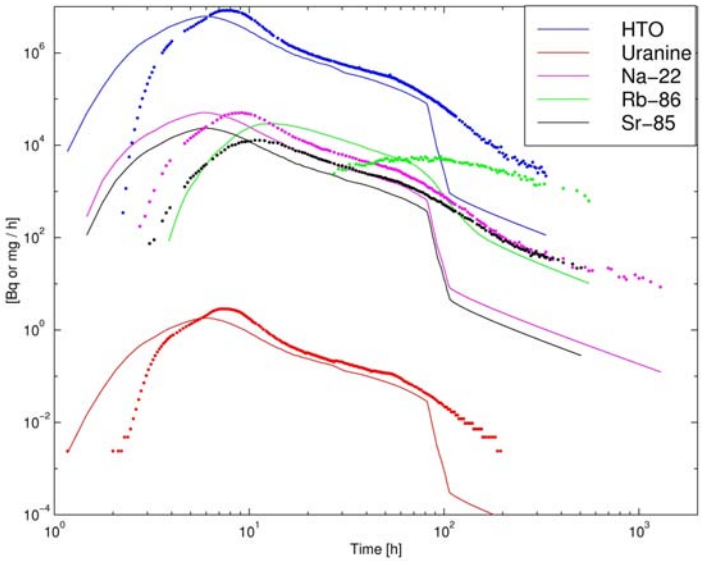

Figure 3-13. Measured breakthrough curves in the STT-1b test. Simulation results are presented with solid lines and the corresponding measured breakthrough curves with dots.

STT-2 test

The modelling of the STT-2 test took advantage of the experimental results of the preceding STT-1 test. This resulted in a wider spread of modelled tracer residence time distributions in the STT-2 test than in the STT-1 and STT-1b tests. The lower flow rate in the STT-2 test has a clear influence on the observed transport characteristics. The tracer recoveries in the STT-2 test were clearly lower than in the STT-1 and STT-1b tests. The measured breakthrough curves of the STT-2 test also show double peak behaviour, which was not observed in the STT-1 tests (Figure 3-15 and Figure 3-16). The activation of two parallel flow channels has been proposed as an explanation for the double peaks (Andersson et al., 1999b).

The modelling of the STT-2 test is based on a single transport channel. The simulated breakthrough curves are not accurate in the early parts of the breakthrough curves, but the tailings and later breakthrough times are better reproduced by the simulations (see e.g. Uranine, Sodium).

The lowered flow rate in the STT-2 test clearly affects the behaviour of the simulated breakthrough curves. For example, the tailings of the simulated breakthrough curves for Uranine and HTO follow the $\sim t^{-3/2}$ slope, indicating that

retention by matrix diffusion is conceivable under the flow conditions of the STT-2 test.

In many cases the experimental results show lower recoveries, e.g. the measured recovery of Caesium is only about 11%. The low observed recovery might result from tracer retention and the short experimental time scale. However, it is also possible that some of the injected tracer could be lost as a result of the background flow field. Therefore, the shape of the modelled breakthrough curves is more interesting than the correctness of their levels.

The tracer source terms at the beginning of the flow paths show similar tailing to the earlier STT-1 tests (Figure 3-14) and this may have influenced the tailings of the non-sorbing tracers.

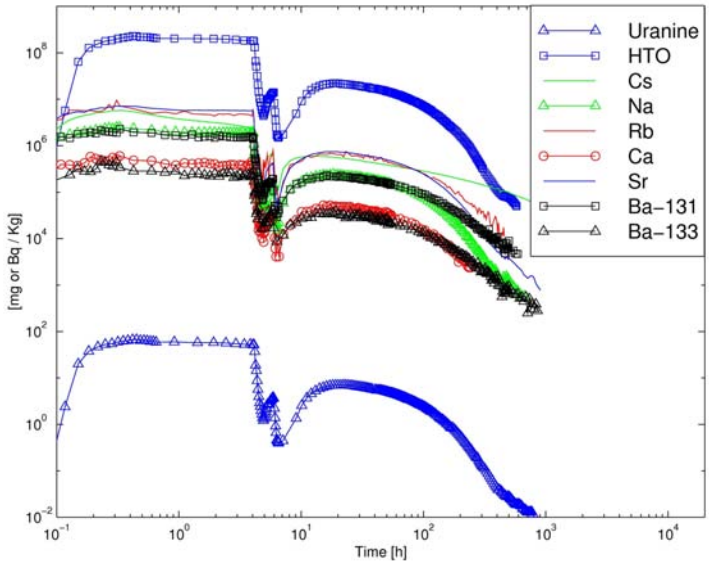

Figure 3-14. Measured tracer source functions at the beginning of the STT-2 test.

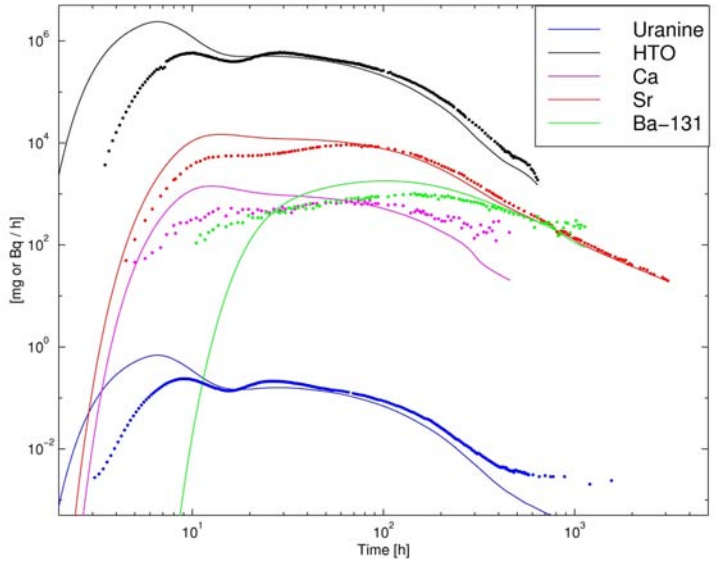

Figure 3-15. Measured breakthrough curves for Uranine, tritated water (HTO), Sr-85, Ba-131, and Ca-47 in the STT-2 test. Simulation results are presented with solid lines and the corresponding measured breakthrough curves with dots.

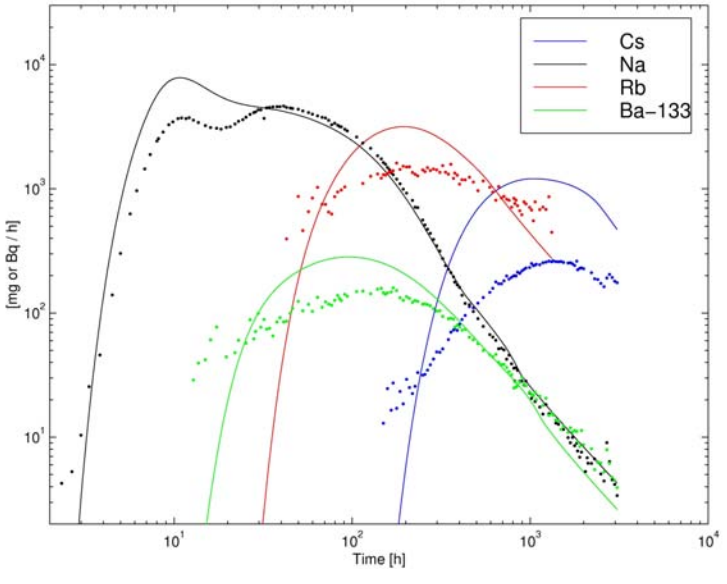

Figure 3-16. Measured breakthrough curves for Cs-134, Na-22, Rb-86, and Ba-133 in the STT-2 test. Simulation results are presented with solid lines and the corresponding measured breakthrough curves with dots.

3.6 Conclusion

Accurate modelling of the tracer transport for sorbing tracers requires the immobile pore structure and sorption properties along the tested flow path to be known. This is especially true for strongly sorbing tracers. The stagnant pools of the flow field, fracture-filling materials, and the rock matrix itself have to be quantified in terms of their retention properties, i.e. porosity, pore diffusivity, and sorption. It is a difficult task to identify geological materials along the flow path and estimate their in situ retention properties. Rough estimates are usually made using typical laboratory data on tracers and retention properties in different geological materials. This was also the approach in the first prediction for the STT-1 and STT-1b tests, which applied laboratory data to the unaltered rock matrix. The poor fit of the blind predictions for sorbing tracers suggests that using laboratory data in in situ transport modelling requires careful identification of the major immobile zones that are active in the flow conditions being studied.

The time span of the TRUE tracer test was five years. This means that the hydraulic conditions in experimental site have also changed. The hydraulic head in KXTT3 (the pumping borehole of the STT-1, STT-1b, and STT-2 tests) was at a higher potential compared to the boreholes used as sources for the tracer tests. At the end of the STT-2 test the head difference was reversed. However, the differences in the hydraulic head levels between the borehole sections used are of an order of one metre, compared to the drawdowns of about ten metres induced by the pumping in KXTT3. This means that it is likely that the pumping in KXTT3 dominates the local flow field of the tracer tests and that the conditions for the tracer tests remained reasonably stabile.

Attempts were made to take the heterogeneity of the hydraulic properties of the fracture being tested into account in the STT-1 and STT-1b models. The STT-2 model is a channel model that does not directly quantify fracture in-plane heterogeneity. To some extent heterogeneity affects the geometry of the flow paths that dominate transport in the STT-1 and STT-1b models. However, the modelling of the non-sorbing tracer tests that was performed earlier indicated clearly that a radially converging flow field leads to a single flow path in the majority of the simulations (Poteri and Hautojärvi, 1998).

The experimental data show a weak double peak breakthrough in STT-1 and a very clear double peak breakthrough in STT-2. Both tests were performed between the same source and sink, but using a lower flow rate in the STT-2 test. The breakthrough curves indicate that two flow paths were active in STT-2 and

one flow path dominated in the STT-1 test. This indicates that the background flow field can be an important factor in the in situ tracer test and changes in the strength of the tracer test sink easily lead to a completely different flow path.

4. Transport in a fracture network

4.1 Experimental site

Tracer tests in a fracture network were performed as a part of the TRUE Block Scale project (TBS) at the Äspö Hard Rock Laboratory. The experimental site of the TBS project is located in the south-western part of the Äspö underground rock laboratory at a depth of 450 m below the ground surface. Experimental geometry, the main hydraulic structures, and the tracer test sink and source locations are shown in Figure 4-1. A description of the tested flow paths C1, C2, and C3 is given in Table 4-1.

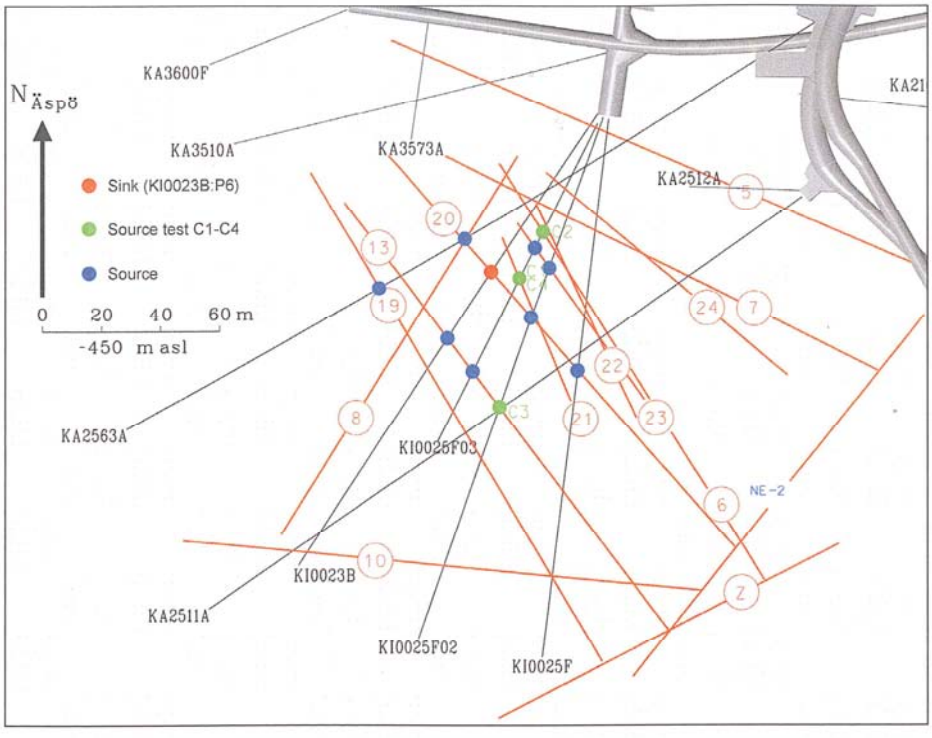

Figure 4-1. Experimental geometry in the tracer tests C1, C2, and C3 (from Andersson et al., 2002a).

Table 4-1. Characteristics of the tracer tests C1, C2, and C3.

Test	Distance [m]	Injection structure	Withdrawal structure	Structures involved in the flow path
C1	14	#20	#21	#20, #21
C2	97	#23	#21	#20, #21, #22, #23
C3	33	#21	#21	#21

4.2 Modelling approach

The goal was to find a model that reproduces observed breakthrough curves and is also consistent with the other data available from the site. The basic questions addressed are: what are the dominant immobile zones along the tested flow paths? What is the role of the advective flow field in the breakthrough curves? Are there indications of diffusion to the immobile zones in the breakthrough curves?

The concept of the transport model is presented in Figure 4-2. The model can be summarised by the following main points:

- Transport takes place along a well-defined transport channel in each tracer test. This means that in the model all the tracer mass eventually goes to the sink. The assumption of the transport channels and weak mixing between the channels has commonly been applied in the performance assessment modelling.
- Transport in the flow channel is characterised by advection and generalised Taylor dispersion. The flow field is characterised by the velocity profile and the correlation length of the spatial velocity variation.
- Solute transport can be retarded by diffusion to an immobile pore space that is adjacent to the transport path.
- Tracers can sorb on the fracture surfaces or on the pore surfaces of the immobile pore space.

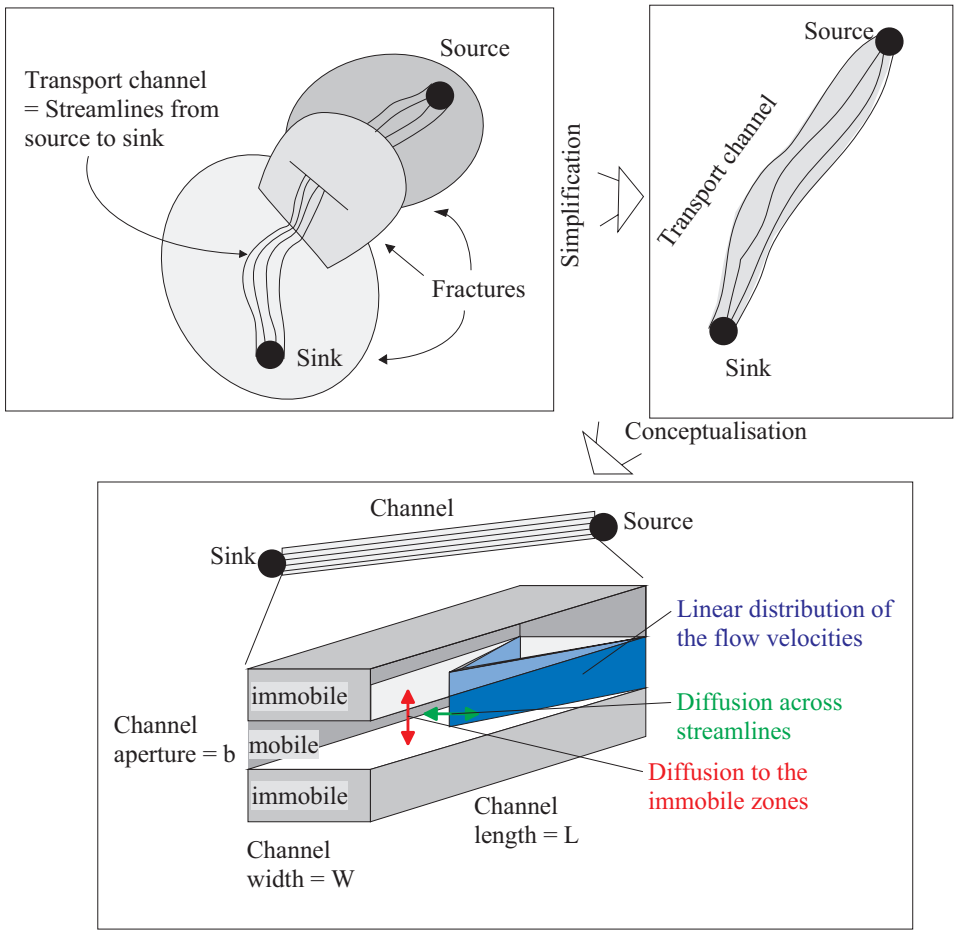

Figure 4-2. Conceptualisation of the tracer transport in the fracture network by transport channel.

Immobile zones may have a significant influence on the tracer transport. Therefore, alternative immobile pore spaces were modelled: only in the rock matrix as an immobile zone, only a fault gouge as an immobile zone, and only stagnant pools in the flow field as immobile zones. In all cases the immobile zone is assumed to be infinite. As an example, Figure 4-3 illustrates the conceptual difference between a model with a fault gouge and a model without a fault gouge.

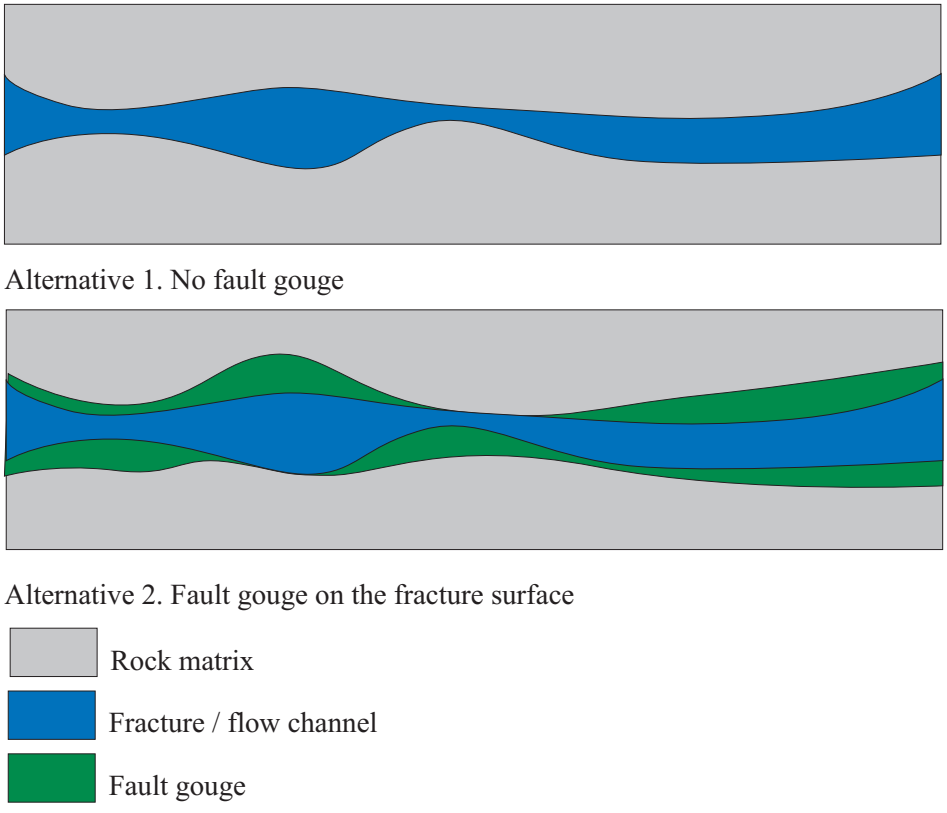

Figure 4-3. Two alternative options of the immobile zones illustrated (vertical view across the transport channel). The stagnant zones of the flow field are also studied, in addition to the alternatives illustrated in this figure.

4.3 Advective transport

Tracer particles follow streamlines (in the steady state flow field) in purely advective transport. In this case the solute residence time distribution is characterised by the lengths of the streamlines and flow velocities. In a homogeneous fracture and under a radially converging flow field streamlines start from the source borehole and converge to the pumping borehole, forming a transport channel that is triangular in shape. In this case the average width of the transport channel is usually smaller than the diameter of the source borehole (Figure 4-4a). The injection of water at the source borehole, i.e. a dipole flow field, changes the shape of the transport channel and the width of the transport

channel may vary considerably along the flow path (Figure 4-4b). Heterogeneous hydraulic properties in the fracture plane increase the variation in the width of the transport channel, depending on the variation in the local hydraulic properties of the fracture (Figure 4-4c). Tracer retention in the model is represented by effective properties for the different cases above.

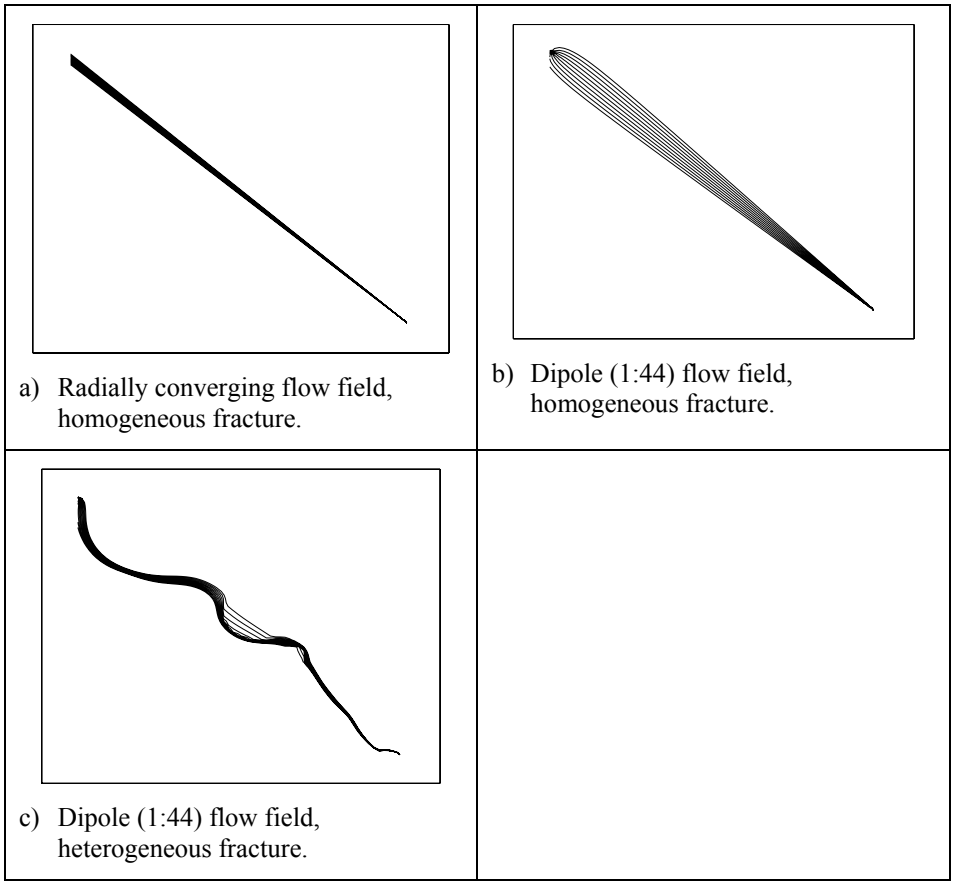

Figure 4-4. Simulated streamlines for three different cases: a) homogeneous fracture and in a radially converging flow field (injection at upper left-hand corner and pumping at lower right-hand corner); b) homogeneous fracture and dipole flow field (strength of the dipole is 1:44, which is approximately the ratio of the dipole strength in the C1 test), and c) heterogeneous fracture and dipole flow field (strength of the dipole is 1:44).

Advective transport in the transport channel is represented in the model by a linear velocity profile and molecular diffusion in the flow field (cf. Figure 3-5). In this case the correlation length of the velocity variation is half of the channel width. The same model also applies for a case in which the correlation length of

the velocity variation is much larger than the width of the transport channel. Figure 4-5 illustrates a case in which the correlation length (*a* in Figure 4-5) is one sixth of the channel width.

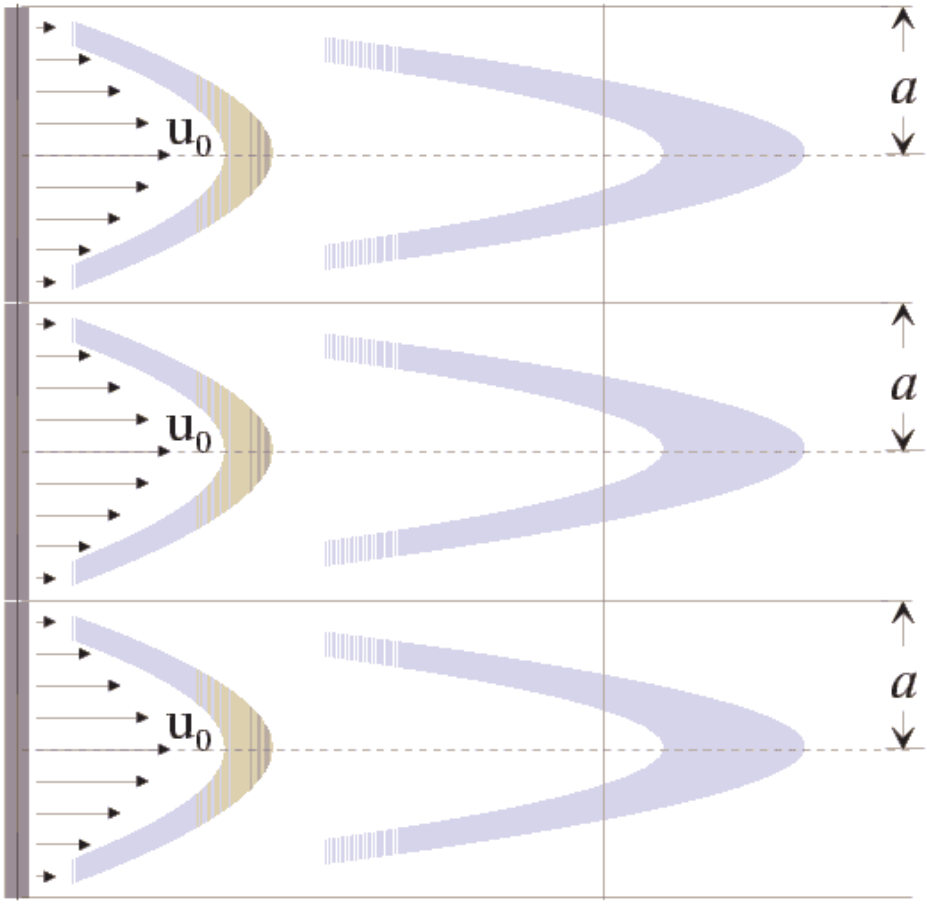

Figure 4-5. An example of the transport channel where the correlation length of the velocity variation is much smaller than the channel width. The released tracer plume is illustrated at three different time steps using different grey scales.

The mean concentration across the solute transport channel in the case of the generalised Taylor dispersion can be solved analytically. For a narrow box-function release it is given by Hautojärvi and Taivassalo (1994):

$$C_m = \frac{1}{2}\left(erf\left[\frac{\frac{1}{2}X_s + X + \xi_1}{2\sqrt{\xi_2}} \right] + erf\left[\frac{\frac{1}{2}X_s - X - \xi_1}{2\sqrt{\xi_2}} \right] \right);$$

$$\xi_1 = -\frac{1}{2}\tau;\ \xi_2 = \left(\frac{1}{(Pe)^2} + \frac{1}{120} \right)\tau - 8\sum_{n=0}^{\infty} \frac{1 - e^{-(2n+1)^2 \pi^2 \tau}}{(2n+1)^8 \pi^8}; \qquad (4\text{-}1)$$

$$\tau = \frac{D\,t}{a^2};\ X = \frac{D\,x}{a^2 v_0};\ X_s = \frac{D\,x_s}{a^2 v_0};\ Pe = \frac{a\,v_0}{D}$$

where D is the molecular diffusion coefficient in water, a is the correlation length of the velocity variation, x_S is the initial width of the tracer plume (see Figure 3-5), u_0 is the maximum flow velocity, t is the time, and x is the position along the channel.

Solution (4-1) is not completely accurate for totally advection-dominated cases, i.e. in the case of very small X (Equation (4-1)). This case has been taken into account by replacing Solution (4-1) by the purely advective solute transit time distribution if $X \leq 0.1$.

The tracer residence time distribution for advective transport under a linear velocity profile and well-mixed conditions at the tracer injection point is presented in Equation (4-2). Solute transport in the mobile part of the transport channel is illustrated in Figure 4-6 for a few different flow rates. The transport is advection-dispersion-dominated in case $X > 0.5$ and governed by the velocity profile for small values of X (i.e. the residence time distribution given in Equation (4-2)).

$$\dot{m}(t) = 2m_0 \frac{{t_0}^2}{t^3}. \qquad (4\text{-}2)$$

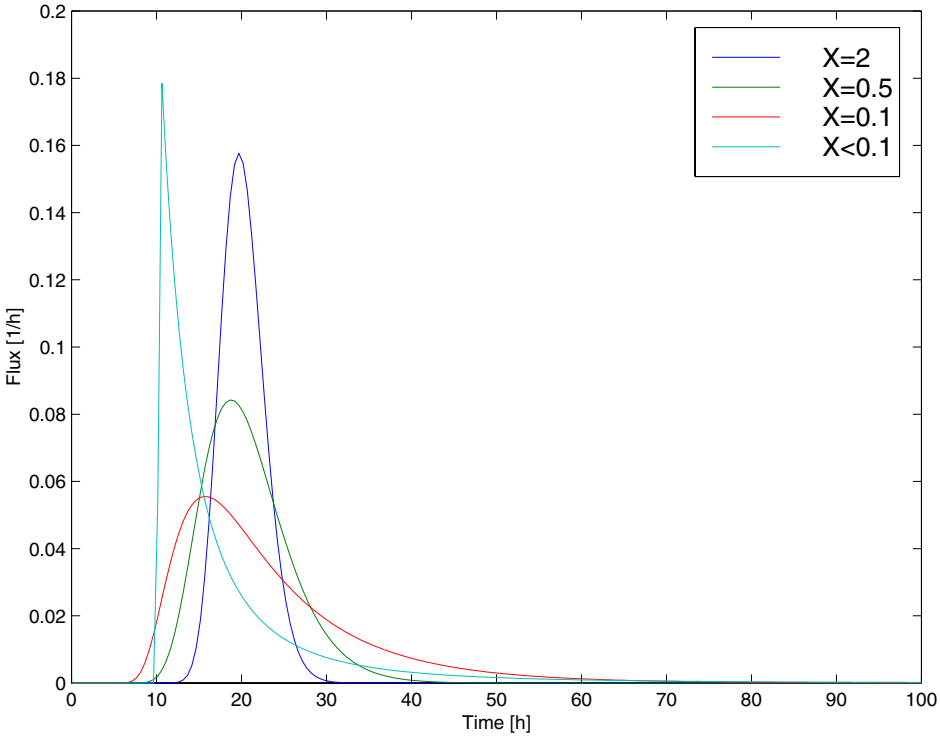

Figure 4-6. Groundwater transit time distributions calculated using Equations (4-1) and (4-2) and parameter values m_0 = 1, t_0 = 10 and X = 2, X = 0.5, X = 0.1, and X < 0.1.

4.4 Retention model

The solute residence time distribution for advection-matrix diffusion-dominated transport follows the approach applied in the modelling of the transport in a single fracture. The tracer residence time distribution is given by Equation (4-3)

$$j(t,t_w,u,R_a) = H(t-R_a t_w)\frac{u}{\sqrt{\pi}\left(t-R_a t_w\right)^{3/2}} e^{-\frac{u^2}{t-R_a t_w}}, \qquad (4\text{-}3)$$

where parameter u determines the strength of the matrix diffusion, t_w is the groundwater transit time, and R_a is the surface retardation coefficient. The strength of the matrix diffusion (parameter u) for different parts of the streamtube is coupled to the advective transit time distribution (t_w) according

$u = u(t_w) = U\ t_w$ given in Equation (3-5). The approach is based on the assumption that the differences in advective transit times are mainly due to different flow rates through different parts of the channel. The tracer residence time distribution with retention by matrix diffusion is calculated by integration

$$k(t) = \int_0^t j(t, t_w, U_t\ t_w, R_a) b(t_w) dt_w \ , \tag{4-4}$$

where $b(t_w)$ is the advective residence time distribution. Equation (4-4) gives the tracer breakthrough curve for the instantaneous release of a unit mass of the tracer in the event of advection and matrix diffusion. The actual tracer injection curve can be taken into account by convoluting the residence time distribution $k(t)$ in Equation (4-4) with the tracer injection function $s(t)$,

$$c(t) = \int_0^t s(t') k(t - t') dt' \ . \tag{4-5}$$

Equation (4-3) shows that surface sorption causes a shift in the residence time distribution towards later breakthrough times, but it does not change the shape of the curve. This means that surface sorption coefficients (R_a) determine the time of the first arrival for a sorbing tracer. This is illustrated in Figure 7-6 by presenting $j(t,tw,u,Ra)$ for two pairs of u and R_a.

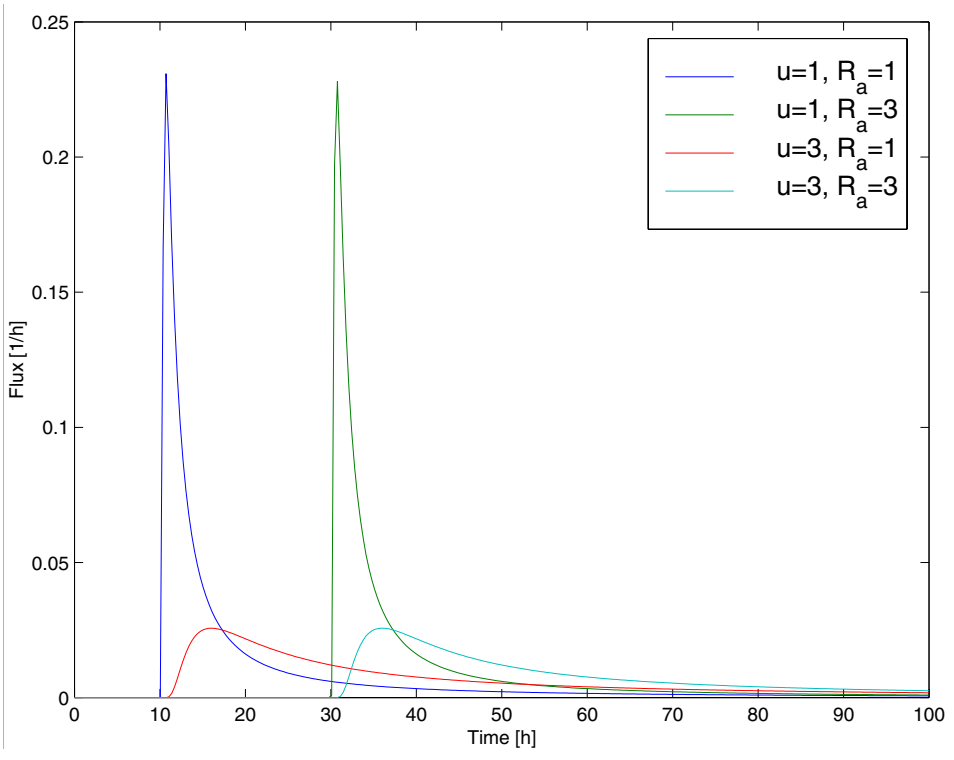

Figure 4-7. Solute discharge rates calculated using Equation (4-3) for different pairs of u and R_a. It is evident that R_a determines the time of the early breakthrough.

4.5 Evaluation of the tracer tests

Tracer tests C1, C2, and C3 were evaluated using the model in order to find a reasonable combination of the individual physical parameters that are able to explain the retention observed in the experiments. Physical retention parameters are determined in two stages. First, in the curve-fitting stage, the parameter groups describing retention by matrix diffusion are fitted. This gives numerical estimates for the parameter groups U and R_a (cf. Equations (3-5), (4-3), and (4-4)) for each test and each tracer. Finally, individual physical parameters in the parameter groups U and R_a are fitted by considering all tests together.

It is easy to compare the sorption coefficients R_a with the measured laboratory data of the Äspö fractures. According to Equation (4-6), R_a depends on the fracture aperture ($2b$) and surface sorption coefficient (K_a).

$$R_a = 1 + \frac{2}{(2b)} K_a . \tag{4-6}$$

The parameter group U is more complicated. It is presented in Equation (4-7).

$$U_t = \frac{\sqrt{D_w G \varepsilon^2 \left(1 + \frac{(1-\varepsilon)}{\varepsilon} K_d \rho \right)}}{2b}, \tag{4-7}$$

where D_w is the coefficient of molecular diffusion in free water, G is the geometric factor for diffusion in the immobile zone (this is calculated from the formation factor; cf. Table 4-2), ε is the porosity of the immobile zone, K_d is the sorption coefficient in the immobile zone, $2b$ is the fracture aperture, and ρ is the bulk density of the immobile zone.

The stagnant pools of the flow field are represented by a slightly different form, U_s, that is given in Equation (4-8). Stagnant zones are assumed to be located in the fracture plane. This means that the diffusion to the stagnant zones takes place in the lateral direction in the fracture plane, in contrast to the transversal direction of diffusion to the rock matrix.

$$U_S = \frac{\sqrt{D_w \varepsilon_S R_a}}{2a_S}, \tag{4-8}$$

where ε_s is the portion of the stagnant zone available along the channel compared to the channel length and $2a_s$ is the mean lateral distance between the stagnant zones.

The geometry of the transport channel is determined by the width of the transport channel when the channel aperture is fitted using Equation (4-7). The flow velocity and flow rate through the transport channel are fixed by the boundary conditions of the tracer test. The model assumes that the flow velocity varies linearly from zero velocity to maximum velocity. The total flow rate through the channel is then given by

$$Q = \frac{v_0 W (2b)}{2}, \tag{4-9}$$

where Q is the flow rate, v_0 is the maximum flow velocity, W is the channel width, and $2b$ is the channel aperture.

The measured tracer test data contain 6 different breakthrough curves for test C1, 2 breakthrough curves for test C2, and 3 breakthrough curves for test C3. Each tracer in each test provides one model fitted U_t, i.e. a total of 11 fitted values of U_t. Unknown physical parameters include K_d for each tracer (9 different tracers), the immobile zone porosity ε, the geometric factor G of the diffusion in the immobile porosity (one immobile zone in each model) and the transport channel aperture $2b$ (three flow paths, C1, C2, and C3). The aperture is fitted separately for each of the three flow paths but the porosity and geometric factor are assumed to be the same for all flow paths. This means that 14 different physical parameters should be determined. The surface sorption coefficients K_a are calculated directly using Equation (4-7) and a channel aperture that is fitted from U.

Fitting K_d, ε, G, and $2b$ values is carried out by minimising the difference between the fitted grouped parameter U values and corresponding U values resulting from Equation (4-7). The process of fitting is constrained by the laboratory data on the K_d's, G, and ε. The constraints applied for the K_d's, G, and ε for the rock matrix and fault gouges are given in Table 4-2.

Table 4-2. Limits of the acceptable values for constraining K_d, matrix porosity, and geometric factor in the fitting of the retention parameters.

	Alternative 1, Rock Matrix		**Alternative 2, Fault gouge**	
Parameter	**Acceptable values [m^3/kg]**	**Source**	**Acceptable values [m^3/kg]**	**Source**
K_d, HTO	0	Non-sorbing	0	Non-sorbing
K_d, Re	0	Non-sorbing	0	Non-sorbing
K_d, Br	0	Non-sorbing	0	Non-sorbing
K_d, Na	$\leq 2.2 \cdot 10^{-4}$	Table 6-3 in [1)]	$\leq 2.2 \cdot 10^{-4}$	Slightly over the value $2.0 \cdot 10^{-4}$ m^3/kg given in Table 7-4 in [2)]
K_d, Ca	$\leq 6.3 \cdot 10^{-4}$	Table 6-3 in [1)]	$\leq 1.3 \cdot 10^{-3}$	Table 7-4 in [2)]
K_d, K	$\leq 4 \cdot 10^{-4}$	K_d of Na in Table 6-3 in [1)], in the fitting stage this was increased slightly over the K_d of Na	$\leq 5.2 \cdot 10^{-3}$	Table 7-4 in [2)]
K_d, Rb	$\leq 2.53 \cdot 10^{-3}$	Table 6-3 in [1)]	$\leq 2.8 \cdot 10^{-2}$	Table 7-4 in [2)]
K_d, Cs	$\leq 1.52 \cdot 10^{-2}$	Table 6-3 in [1)]	$\leq 2.8 \cdot 10^{-1}$	Table 7-4 in [2)]
K_d, Sr	$\leq 2.6 \cdot 10^{-4}$	Table 6-3 in [1)]	$\leq 1.3 \cdot 10^{-3}$	Table 7-4 in [2)]
Porosity, ε	0.1 ... 0.6%	Table 7-1 in [2)] and Section 7.2.6 in [2)]	1.5 ... 3.5%	Based on Table 7-1 in [2)]
Geometric factor, G	0.0125 ... 0.017	See below	0.0125 ... 0.017	See below

[1] Byegård et al. (1998)

The acceptable range of values for the geometric factor G is selected on the basis of the data given by Andersson et al. (2002b). The effective diffusion coefficient can be written as

$$D_e = D_w G \varepsilon = D_w F , \quad (4\text{-}10)$$

where F is the formation factor. The values given in Andersson et al. (2002b) are $F = 5 \cdot 10^{-5}$ and $\varepsilon \approx 4 \cdot 10^{-3}$ for unaltered Äspö diorite and $F = 1.7 \cdot 10^{-5}$ and $\varepsilon \approx 1 \cdot 10^{-3}$ for Feature A. Using Equation (4-10), these values give $G = 0.0125$ and $G = 0.017$ for Äspö diorite and Feature A, respectively. The range between these two values was applied as the acceptable range of the geometric factor G.

4.6 Model parameters

Laboratory data are available on the sorption properties and porosities of the rock samples (e.g. Andersson et al., 2002b and Byegård et al., 1998).

The parameters in Table 4-2 were varied between the given limits to achieve a reasonable fit between the measured and modelled breakthrough curves. Some parameters were varied using a few a priori selected values. This kind of parameter was the correlation length of the velocity profile (four different correlation lengths were tested). Finally, the parameters in Table 4-2 were kept fixed during the modelling.

Table 4-3. Parameters fixed prior to the modelling or varied during the modelling.

Parameter **Test**		**Source**	**Comment**
Path length, *L*			
C1	16	Table 6-1[2]	
C2	97	Table 6-1[3]	
C3	35	Table 6-1[3]	
Correlation length of the velocity profile **{C1, C2, C3}**	{0.01, 0.02, 0.05, 0.1} m	Selected parameter	Selected 4 different variants within the range [0.01, 0.1] m that is considered reasonable
Injection flow rate, *Q*			
C1	2700 ml/h	Table 2-2[3]	C1 forced injection
C2	600 ml/h	Table 2-2[4]	C2 forced injection
C3	112 ml/h	Calculated from HTO injection curve	
Extraction flow rate	117.6 litres/h	TRUE Block Scale Communication #184	From file: "Phase C BTC data 010110.xls"
Molecular diffusion coefficient in free water, D_w	$1.0 \cdot 10^{-9}$ m^2/s	Commonly applied value	$2.4 \cdot 10^{-9}$ m^2/s is used in [4]

The channel model applied in the evaluation inevitably and always leads to complete recovery of the tracers. In the tracer tests the recoveries may vary because other sinks than the pumped section of the borehole also exist at the experimental site. This needs to be taken into account when the modelled

[2] Andersson et al. (2002a)
[3] Andersson et al. (2001)
[4] Andersson et al. (2002b)

breakthrough curves are compared with the measured breakthrough curves. In the evaluation this is taken into account by extrapolating the recoveries of the experimental breakthrough curves to very long observation times and adjusting the modelled recoveries to correspond to the extrapolated experimental recoveries.

The extrapolation of the experimental recoveries towards longer observation times is performed by assuming that the flow condition induced by the pumping of the experimental sink is maintained forever. Two different models are fitted to describe the tailings of the observed breakthrough curves: exponential and power-law ($\sim t^{-3/2}$) behaviour. The final tracer recoveries are achieved by extrapolating the breakthrough curves to 10^7 hours. The calculated recoveries are compared to the injected masses given in Table 4-4. The results of the extrapolation are presented in Figures 4-8 to 4-10. The two alternative recovery curves are assumed to bound the region of the feasible final recoveries. In all cases the exponential tailing gives lower recoveries and $\sim t^{-3/2}$ extrapolation gives higher recoveries.

In many cases the extrapolated recoveries exceed the 100% limit. This happens for the Br-82 in the C1 test as early as in the measured part of the recovery curve. Clearly, this indicates full recovery. The problem is that in the single channel model the integrated recovery of the breakthrough should eventually correspond to the total injected mass. To be comparable with the measured breakthrough curve, the calculated recovery should coincide with the integrated mass of the measured breakthrough curve. The extrapolation using $\sim t^{-3/2}$ tailing shows more consistent recoveries, for example among the different tracers of the C1 test. One clear exception is Re-186 in C2, which shows a very high recovered mass. However, in this case the double peak shape of the breakthrough curve may indicate that there were possibly also problems with this tracer in the C2 experiment. On the basis of the more consistent behaviour of the recoveries calculated using $t^{-3/2}$ tailing, this scheme was selected for the evaluation calculations. For all tracers the simulated recovered masses are scaled to the extrapolated mass, although the extrapolated recovered mass can be higher than the corresponding injected total mass.

Table 4-4. Injected masses in the C1, C2, and C3 tracer tests and extrapolated recovered mass.

Test (Tracer)	Injected mass [Bq]	Recovery [%] Exponential extrapolation	Recovery [%] Power law extrapolation
C1 (Br-82)	$1.38 \cdot 10^{8}$	113	124
C1 (Na-24)	$1.56 \cdot 10^{7}$	102	129
C1 (K-42)	$2.29 \cdot 10^{8}$	84	124
C1 (Ca-47)	$1.07 \cdot 10^{7}$	101	123
C1 (Rb-86)	$1.33 \cdot 10^{7}$	81	119
C1 (Cs-134)	$7.79 \cdot 10^{6}$	63	89
C2 (Re-186)	$1.71 \cdot 10^{8}$	108	168
C2 (Ca-47)	$5.64 \cdot 10^{7}$	60	90
C3 (HTO)	$2.44 \cdot 10^{8}$	76	91
C3 (Na-22)	$2.16 \cdot 10^{7}$	81	110
C3 (Sr-85)	$2.21 \cdot 10^{7}$	77	116

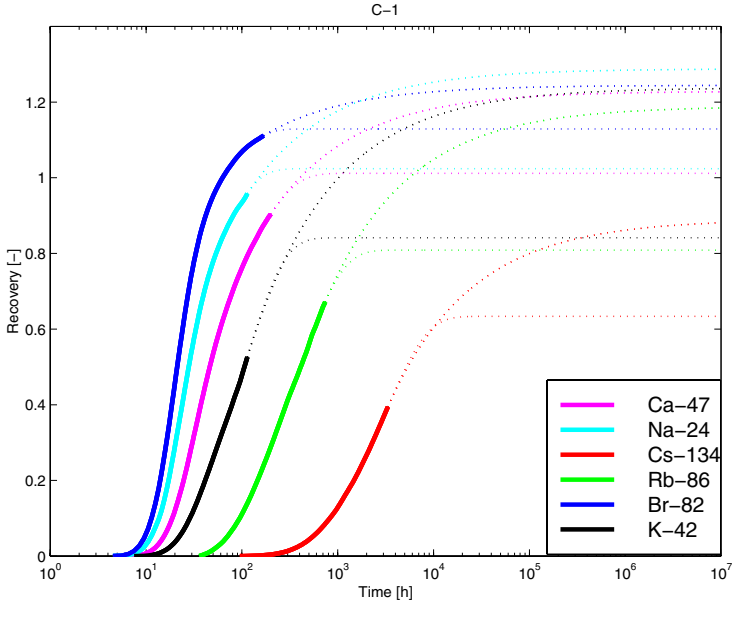

Figure 4-8. Recoveries of the C1 test extrapolated from the measured breakthrough curves. Solid lines represent the measured recovery curves. Dotted lines are for the $t^{-3/2}$ extrapolation (upper lines) and exponential extrapolation (lower lines).

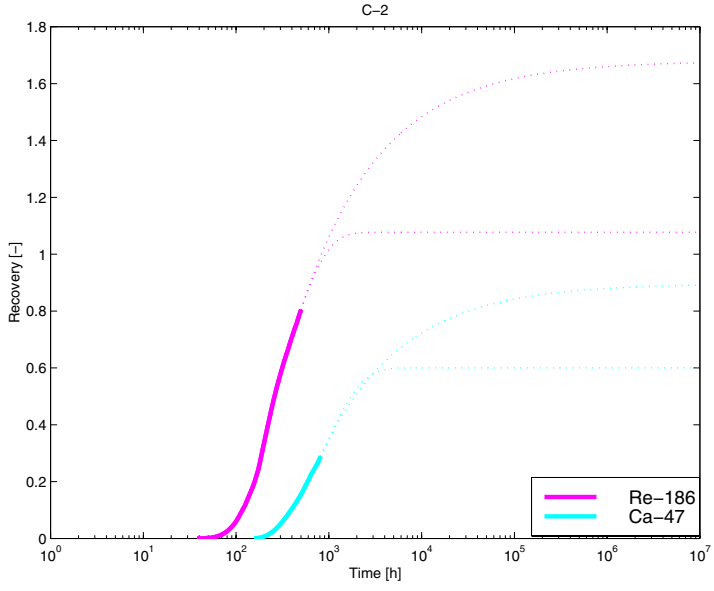

Figure 4-9. Recoveries of the C2 test extrapolated from the measured breakthrough curves. Solid lines represent the measured recovery curves. Dotted lines are for the $t^{-3/2}$ extrapolation (upper lines) and exponential extrapolation (lower lines).

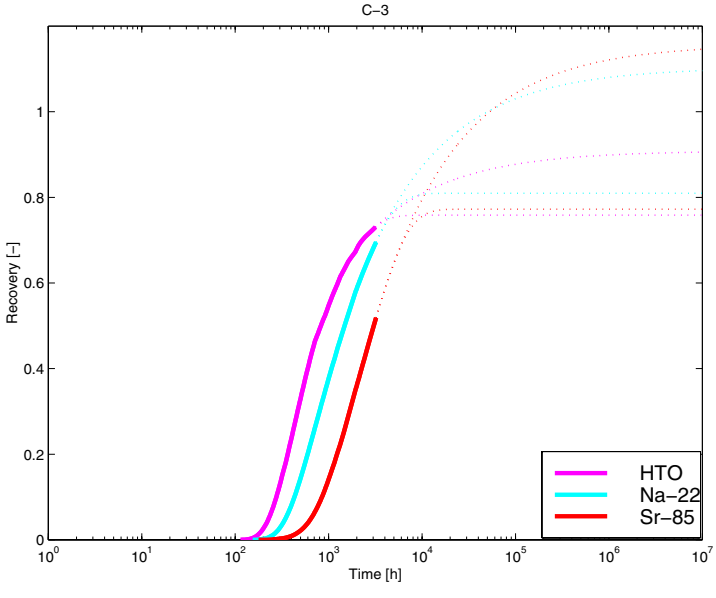

Figure 4-10. Recoveries of the C3 test extrapolated from the measured breakthrough curves. Solid lines represent the measured recovery curves. Dotted lines are for the $t^{-3/2}$ extrapolation (upper lines) and exponential extrapolation (lower lines).

The length, width, and aperture of the channels determine the geometry of the transport channels. Channel lengths are calculated using the in-plane distances of the TRUE Block Scale hydrostructural model (Hermanson and Doe, 2000). Channel length is the only geometrical parameter selected before the modelling. The non-sorbing tracer breakthrough curves fix the volume of the transport channel and the matrix diffusion of the sorbing tracers for the fixed flow rates determine the width of the channel. On the basis of this, the uncertainty in the channel length and in the channel width is coupled. Clearly, a wrong path length should show an unrealistic channel width. The apertures and widths of the channel follow from the evaluation. The channel apertures are calculated from the fitted U parameters (Equation (4-7)). The width of the channel is calculated using a fitted aperture and the flow rate through the transport channel (calculated from the tracer injection curve) and the flow velocity is fitted using Equation (4-9).

Velocity fields are calculated for four different alternatives. The alternatives have different correlation lengths for the variation in velocity: 0.01 m, 0.02 m, 0.05 m, and 0.1 m (cf. Table 4-3). The flow field parameters are calibrated using the breakthrough curves of the non-sorbing tracers. The correlation length has an influence on the calibrated maximum flow velocity.

Different simulation cases are presented in Table 4-5. It is assumed that the flow rate measured in the injection borehole section goes entirely through the transport channel to the sink.

Table 4-5. Simulated alternative flow fields in the Phase C tracer tests. Alternatives "recov. 1" refer to extrapolated final recovery using $t^{-3/2}$ tailing and alternatives "recov. 2" refer to exponential tailing.

Test	Flow rate [ml/h]	Max. flow velocity [m/h]	Channel length [m]	Correlation length in the velocity profile [m]
C1, recov. 1	2700	2.76	16	0.01
C1, recov. 2	2700	2.73	16	0.01
C1, recov. 1	2700	1.67	16	0.02
C1, recov. 2	2700	1.67	16	0.02
C1, recov. 1	2700	1.67	16	0.05
C1, recov. 2	2700	1.67	16	0.05
C1, recov. 1	2700	1.67	16	0.1
C1, recov. 2	2700	1.67	16	0.1
C2, recov. 1	600	2.90	97	0.01
C2, recov. 2	600	2.30	97	0.01
C2, recov. 1	600	2.31	97	0.02
C2, recov. 2	600	1.93	97	0.02
C2, recov. 1	600	1.54	97	0.05
C2, recov. 2	600	1.40	97	0.05
C2, recov. 1	600	1.54	97	0.1
C2, recov. 2	600	1.30	97	0.1
C3, recov. 1	112	0.56	35	0.01
C3, recov. 2	112	0.52	35	0.01
C3, recov. 1	112	0.47	35	0.02
C3, recov. 2	112	0.44	35	0.02
C3, recov. 1	112	0.32	35	0.05
C3, recov. 2	112	0.31	35	0.05
C3, recov. 1	112	0.28	35	0.1
C3, recov. 2	112	0.26	35	0.1

4.7 Influence of different transport and retention processes

4.7.1 Advective transport

The influence of the selected channel geometry and velocity variation on the transport can be analysed using Equation (4-1). Molecular diffusion averages the tracer transit time distribution compared to the transit time distribution resulting from the velocity variation alone. The averaging is more profound when the the velocity variation has shorter correlation lengths or there is a lower flow velocity. Because of the diffusional averaging, the breakthrough curve is symmetric if the velocity correlation length is short enough or the flow velocity is low enough. If the diffusion to the longitudinal direction is omitted, the breakthrough curve gets narrower with a shorter correlation length, eventually approaching plug flow. The opposite case is a very long correlation length or fast flow in which the influence of the molecular diffusion disappears and the breakthrough curve is characterised by the underlying velocity field. A linear velocity profile leads to strongly skewed breakthrough curves, as shown in Figure 4-6. This behaviour is characterised by the dimensionless parameter X, introduced in Equation (4-11) (Hautojärvi, 1989):

$$X = \frac{D_w L}{a^2 v_0}, \tag{4-11}$$

where D_w is the molecular diffusion coefficient in water, L is the channel length, v_0 is the maximum flow velocity, and a is the correlation length of the velocity variation. Values $X < 0.1$ represent advection-dominated transport (Hautojärvi, 1989). In the model these cases are replaced by purely advective transport. The selected range of the correlation lengths produces flow fields that are dominated both by advection and advection-dispersion behaviour. The value of the parameter X and interpretation of the transport characteristics for different alternative models are presented in Table 4-6.

Table 4-6. Characteristics of the flow field in the transport channels. The dimensionless parameter *X* describes the character of the transport. Cases $X < 0.1$ are characterised by purely advective transport. "recov. 1" and "recov. 2" refer to extrapolated recoveries using $t^{-3/2}$ tailing and exponential tailing, respectively.

Tracer test and recovery extra-polation	**Path length [m]**	**Velocity correlation [m]**	**Maximum velocity [m/h]**	**X**	**Character of the transport in flow path**
C1, recov. 1	16	0.01	2.76	0.21	Advection-dispersion
C1, recov. 2	16	0.01	2.73	0.21	Advection-dispersion
C1, recov. 1	16	0.02	1.67	0.086	Advection
C1, recov. 2	16	0.02	1.67	0.086	Advection
C1, recov. 1	16	0.05	1.67	0.014	Advection
C1, recov. 2	16	0.05	1.67	0.014	Advection
C1, recov. 1	16	0.1	1.67	0.0034	Advection
C1, recov. 2	16	0.1	1.67	0.0034	Advection
C2, recov. 1	97	0.01	2.90	1.20	Advection-dispersion
C2, recov. 2	97	0.01	2.30	1.52	Advection-dispersion
C2, recov. 1	97	0.02	2.31	0.38	Advection-dispersion
C2, recov. 2	97	0.02	1.93	0.45	Advection-dispersion
C2, recov. 1	97	0.05	1.54	0.091	Advection
C2, recov. 2	97	0.05	1.40	0.10	Advection
C2, recov. 1	97	0.1	1.54	0.023	Advection
C2, recov. 2	97	0.1	1.30	0.027	Advection
C3, recov. 1	35	0.01	0.56	2.25	Advection-dispersion
C3, recov. 2	35	0.01	0.52	2.42	Advection-dispersion
C3, recov. 1	35	0.02	0.47	0.67	Advection-dispersion
C3, recov. 2	35	0.02	0.44	0.72	Advection-dispersion
C3, recov. 1	35	0.05	0.32	0.16	Advection-dispersion
C3, recov. 2	35	0.05	0.31	0.16	Advection-dispersion
C3, recov. 1	35	0.1	0.28	0.045	Advection
C3, recov. 2	35	0.1	0.26	0.048	Advection

4.7.2 Surface sorption

The retardation coefficients that are caused by surface sorption on the fracture surfaces were estimated by scaling the time axis of the measured breakthrough curves. The breakthrough curves of non-sorbing tracers are left unchanged as reference breakthrough curves. In the C1 test the reference tracer was Br-82 and in C2 and C3 Re-186 and HTO, respectively. Sorbing breakthrough curves were transformed by scaling the time axis linearly until the first breakthrough time coincides with the first breakthrough time of the reference tracer (keeping the mass of the tracer unchanged). The inverse values of the resulting dimensionless scaling factors were selected as the surface retardation factors.

The results of the scaling are presented in Figures 4-11 to 4-13. All the breakthrough curves are normalised to the unit mass to make the comparison easier. Estimated retardation coefficients are presented in Table 4-7. Table 4-7 also includes calculated surface sorption coefficients for a 1-mm fracture aperture. The calculated sorption coefficients are clearly higher than the values reported by Andersson et al. (2002b). This may indicate an aperture smaller than 1 mm or different material on the fracture surface than that investigated by Andersson et al. (2002b).

Table 4-7. Estimated retardation coefficients of surface sorption. As an example, the sorption coefficients are calculated for a 1-mm aperture.

Experiment Tracer	Retardation coefficient, R_a	Aperture [mm]	Sorption coefficient [m]
C1 Br-82	1.0	1	0
C1 Na-24	1.05	1	5.00E-05
C1 K-42	1.3	1	3.00E-04
C1 Ca-47	1.4	1	4.00E-04
C1 Rb-86	3.0	1	2.00E-03
C1 Cs-134	16	1	1.50E-02
C2 Re-186	1.0	1	0
C2 Ca-47	2.4	1	1.40E-03
C3 HTO	1.0	1	0
C3 Na-22	1.3	1	3.00E-04
C3 Sr-85	1.5	1	5.00E-04

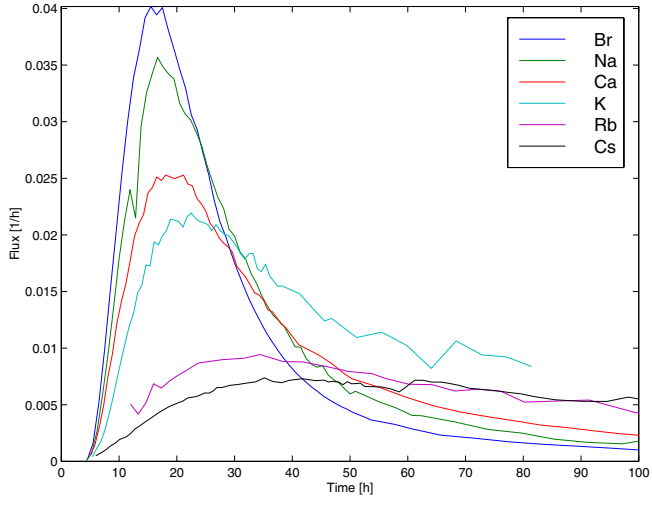

Figure 4-11. Scaling of the C1 test breakthrough curves. Br-82 is the reference breakthrough (assumed to be closest to the ideal non-sorbing tracer) and is left unchanged. The scaling factors of the tracers are adjusted to give the same first breakthrough time as the reference breakthrough curve. All breakthrough curves are normalised to unit mass.

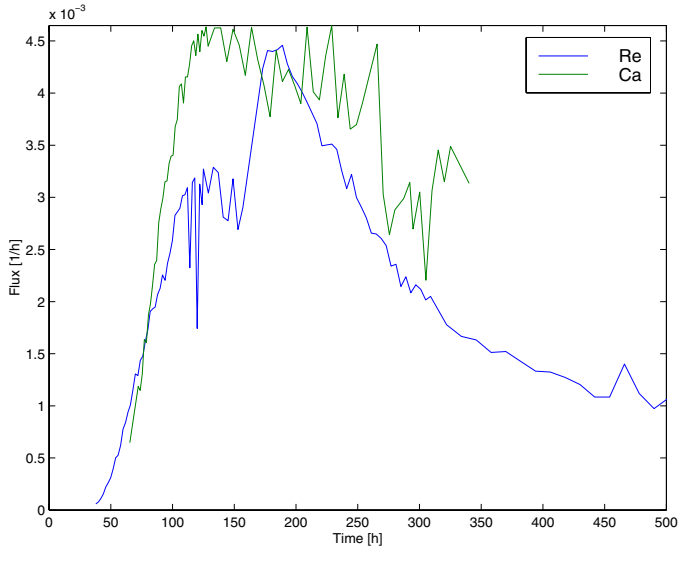

Figure 4-12. Scaling of the C2 test breakthrough curves. Re-186 is the reference breakthrough and is left unchanged. The scaling factors of the tracers are adjusted to give the same first breakthrough time as the reference breakthrough curve. All breakthrough curves are normalised to unit mass.

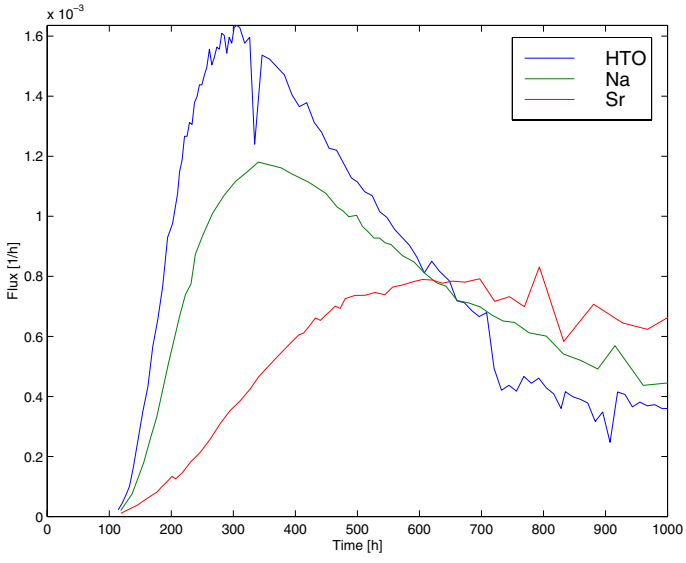

Figure 4-13. Scaling of the C3 test breakthrough curves. HTO is the reference breakthrough and is left unchanged. The scaling factors of the tracers are adjusted to give the same first breakthrough time as the reference breakthrough curve. All breakthrough curves are normalised to unit mass.

4.7.3 Matrix diffusion

The simulated breakthrough curves are calculated by applying Equations (4-4) and (4-5). By adjusting the parameter group U (matrix diffusion) and R_a (surface sorption), the simulated breakthrough curves are fitted to the measured breakthrough curves. The surface sorption R_a has already been estimated (see Table 4-7). However, at this stage the curve fitting of the sorbing tracers is allowed to fine-tune to the surface sorption too. In the fitting the retardation factors in Table 4-7 are used as the lower limit of the R_a. The matrix retention properties are evaluated by comparing the underlying physical retention parameters in the parameter group U (Equations (4-7) and (4-8)) to the corresponding laboratory measurements.

Each tracer test is simulated for 8 different cases. These are four different correlation lengths for the velocity profile (0.01 m, 0.02 m, 0.05 m, and 0.1 m) and two alternatives for the extrapolated final recovery. Variation in the recovered mass is not expected to have a significant influence on the matrix diffusion parameters. However, the outcome of the evaluation basically depends

on the curve fitting to the measured breakthrough curve, which means that this kind of sensitivity study is useful.

The four different correlation lengths for the velocity profile cover both advective and advection-dispersion-type transport behaviour (cf. Table 4-6). In many cases the measured breakthrough curve is characterised by a skewed long tailing. The advection-dispersion model alone cannot produce this kind of breakthrough curve. However, both matrix diffusion and the advective flow field can produce a breakthrough curve with long tailing, but in the model the advection-dominated transport causes a steeper rise in the breakthrough curve than was measured. It seems that advection alone cannot explain the measured breakthrough curves.

4.7.4 Direct fits to the breakthrough curves

The fitted breakthrough curves are presented in Figures 4-14 to 4-24. Simulations that are based on the final recoveries extrapolated using $\sim t^{-3/2}$ tailing seem to give a slightly better fit. Exponential tailing leads to a smaller recovered mass and correspondingly the fitted curves tend to be lower than the measured ones.

The fitted R_a does not vary as much as the matrix diffusion parameter U (Table 4-8). The reason for this is that the estimated R_a values in Table 4-7 were used as the lower limit of the R_a. In most of the cases this lower limit was also reached. The parameter U varies mainly within a factor of two. Higher values for the parameter U are obtained using a shorter correlation length of the velocity variation. In these cases the advective flow field causes symmetric advection-dispersion-type breakthrough curves because molecular diffusion can average the flow velocities over the short correlation length. The actual measured breakthrough curves are asymmetric, with long tailing, which, in these cases, can be produced only by increased matrix diffusion (parameter U). In the case of greater correlation length the advective transport that causes asymmetric tailing is more dominant, thus leading to the strength of the matrix diffusion being less.

The higher recovery estimates ($\sim t^{-3/2}$ tailing) seem to give consistently better fits for every test. In the C1 test the shape of the early breakthrough can be reproduced better by shorter correlation length. The C2 and C3 tests do not show a clear difference between the different correlation lengths of the velocity profile.

Table 4-8. Range of fitted retention parameters U and R_a for simulated breakthrough curves using four different alternatives for the velocity correlation length in the channel and two different alternatives for the extrapolation of the final recovery. In total, the results are based on eight alternative simulations for each tracer and test.

	U [$h^{-1/2}$]		R_a	
Test Tracer	**Min**	**Max**	**Min**	**Max**
C1 Br-82	0.05	0.08	1.00	1.01
C1 Na-24	0.08	0.16	1.05	1.21
C1 K-42	0.17	0.23	1.30	1.31
C1 Ca-47	0.27	0.39	1.40	1.40
C1 Rb-86	0.55	0.89	3.00	3.52
C1 Cs-134	1.60	2.46	16.00	20.09
C2 Re-186	0.05	0.13	1.00	1.00
C2 Ca-47	0.10	0.25	2.40	2.40
C3 HTO	0.03	0.09	1.00	1.00
C3 Na-22	0.06	0.14	1.30	1.34
C3 Sr-85	0.09	0.24	1.50	3.40

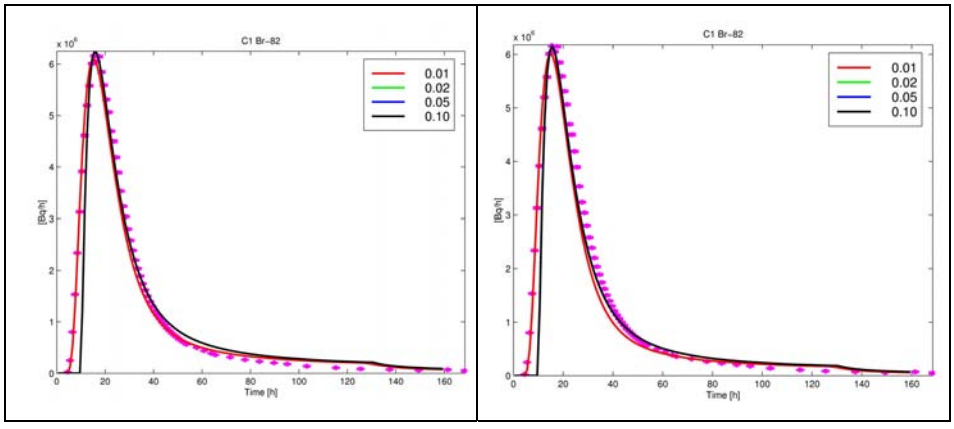

Figure 4-14. Fitted breakthrough curves for Br-82 in C1. Results for the extrapolation of the final recovery by using ~$t^{-3/2}$ tailing (left) and exponential tailing (right). Blue dots and bars indicate measured breakthrough and the given uncertainty region of the measurement. Coloured lines represent fitted breakthrough curves for different correlation lengths of the velocity profile. In both figures the curves for the 0.02-, 0.05-, and 0.1-m correlation lengths overlap.

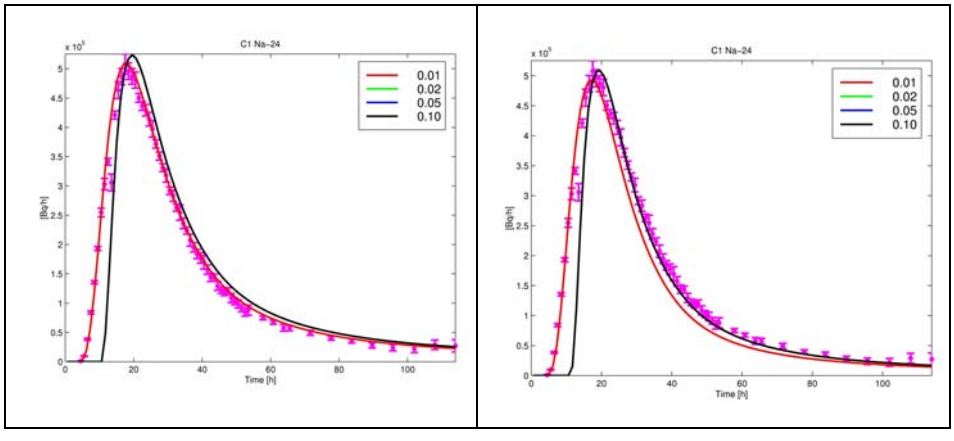

Figure 4-15. Fitted breakthrough curves for Na-24 in C1. Results for the extrapolation of the final recovery by using ~$t^{-3/2}$ tailing (left) and exponential tailing (right). Blue dots and bars indicate measured breakthrough and the given uncertainty region of the measurement. Coloured lines represent fitted breakthrough curves for different correlation lengths of the velocity profile. In both figures the curves for the 0.02-, 0.05-, and 0.1-m correlation lengths overlap.

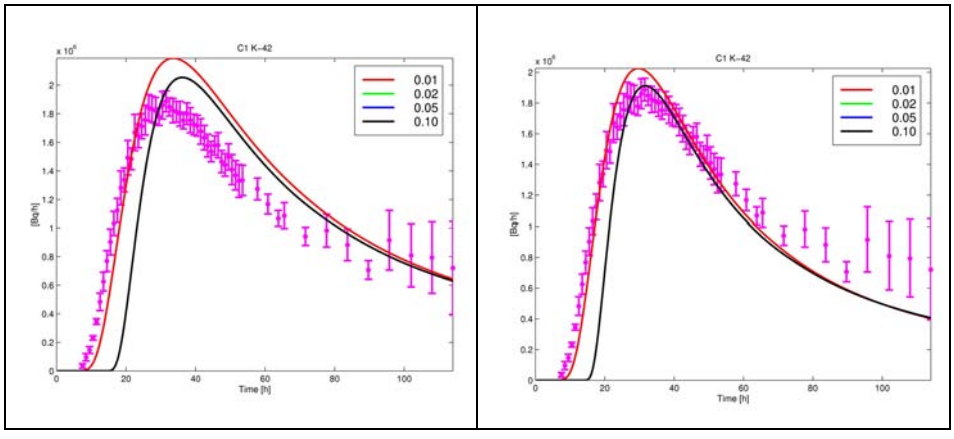

Figure 4-16. Fitted breakthrough curves for K-42 in C1. Results for the extrapolation of the final recovery by using ~$t^{-3/2}$ tailing (left) and exponential tailing (right). Blue dots and bars indicate measured breakthrough and the given uncertainty region of the measurement. Coloured lines represent fitted breakthrough curves for different correlation lengths of the velocity profile. In both figures the curves for the 0.02-, 0.05-, and 0.1-m correlation lengths overlap.

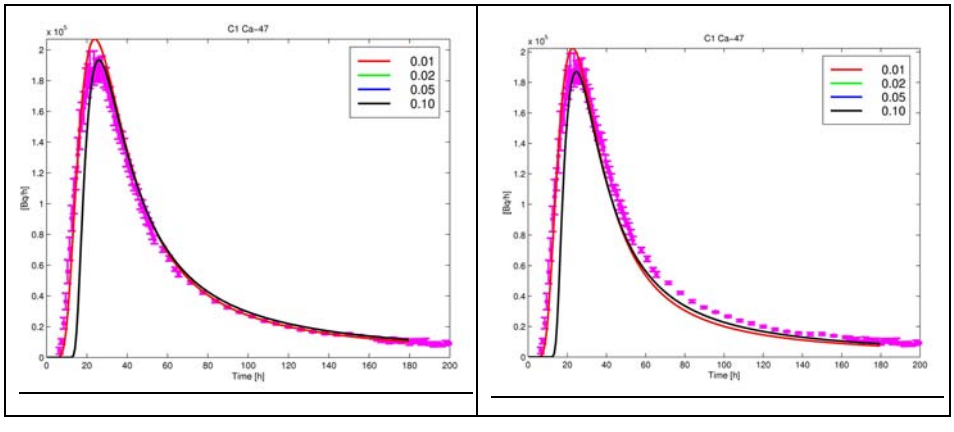

Figure 4-17. Fitted breakthrough curves for Ca-47 in C1. Results for the extrapolation of the final recovery by using ~$t^{-3/2}$ tailing (left) and exponential tailing (right). Blue dots and bars indicate measured breakthrough and the given uncertainty region of the measurement. Coloured lines represent fitted breakthrough curves for different correlation lengths of the velocity profile. In both figures the curves for the 0.02-, 0.05-, and 0.1-m correlation lengths overlap.

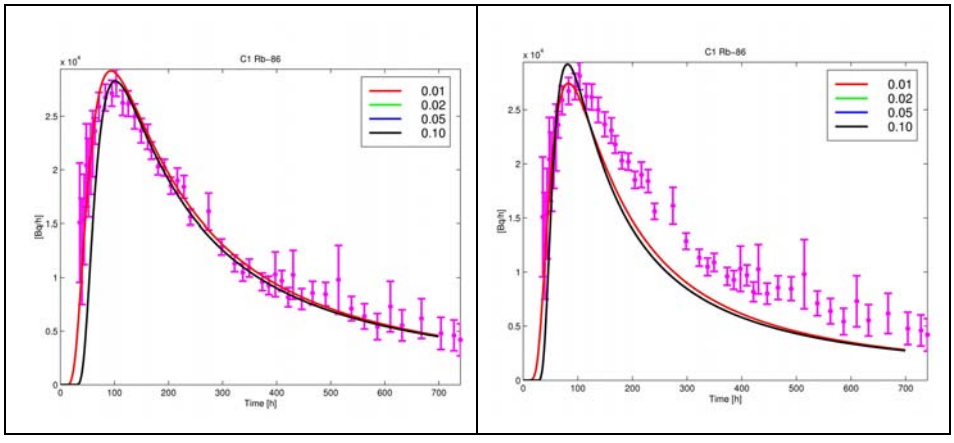

Figure 4-18. Fitted breakthrough curves for Rb-86 in C1. Results for the extrapolation of the final recovery by using ~$t^{-3/2}$ tailing (left) and exponential tailing (right). Blue dots and bars indicate measured breakthrough and the given uncertainty region of the measurement. Coloured lines represent fitted breakthrough curves for different correlation lengths of the velocity profile. In both figures the curves for the 0.02-, 0.05-, and 0.1-m correlation lengths overlap.

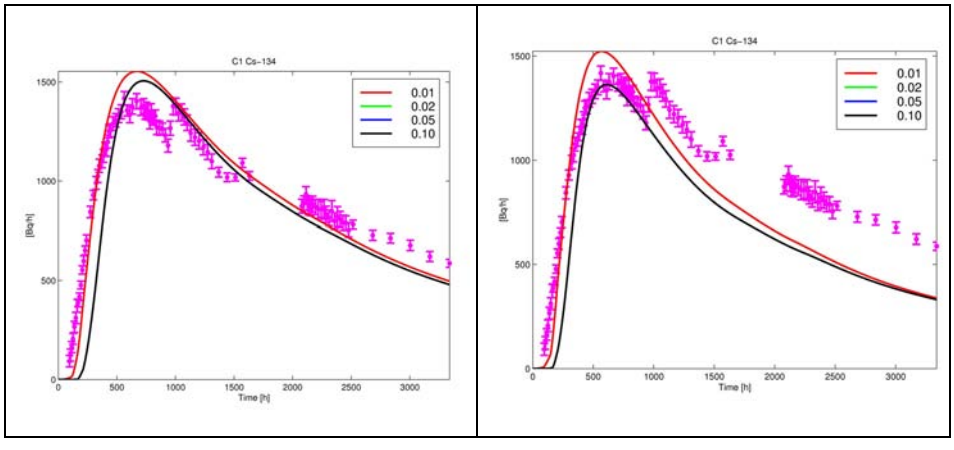

Figure 4-19. Fitted breakthrough curves for Cs-134 in C1. Results for the extrapolation of the final recovery by using ~$t^{-3/2}$ tailing (left) and exponential tailing (right). Blue dots and bars indicate measured breakthrough and the given uncertainty region of the measurement. Coloured lines represent fitted breakthrough curves for different correlation lengths of the velocity profile. In both figures the curves for the 0.02-, 0.05-, and 0.1-m correlation lengths overlap.

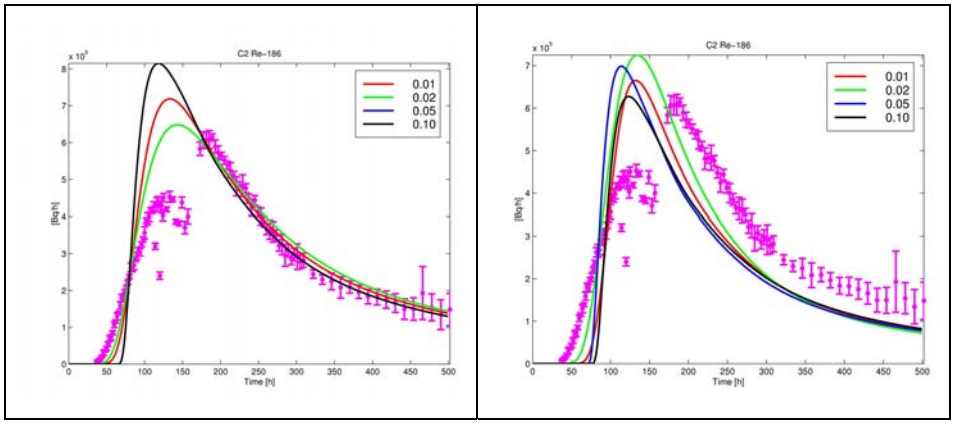

Figure 4-20. Fitted breakthrough curves for Re-186 in C2. Results for the extrapolation of the final recovery by using ~$t^{-3/2}$ tailing (left) and exponential tailing (right). Blue dots and bars indicate measured breakthrough and the given uncertainty region of the measurement. Coloured lines represent fitted breakthrough curves for different correlation lengths of the velocity profile. In the left-hand figure the curves for the 0.05- and 0.1-m correlation lengths overlap.

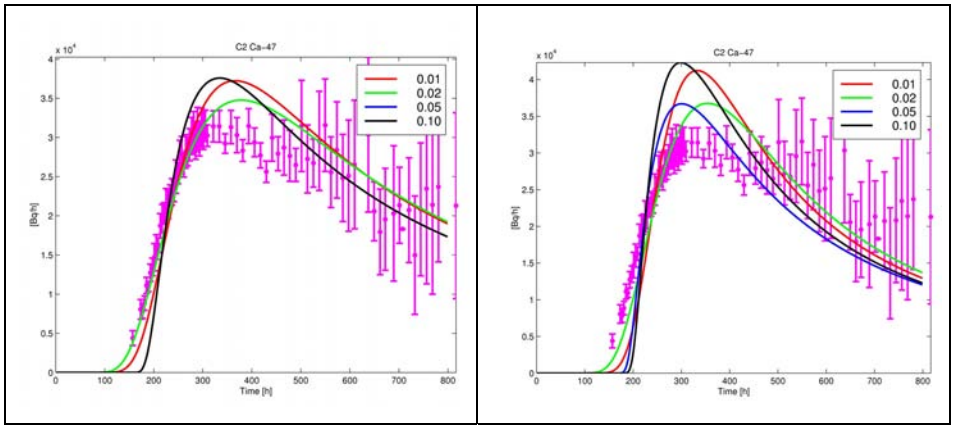

Figure 4-21. Fitted breakthrough curves for Ca-47 in C2. Results for the extrapolation of the final recovery by using ~$t^{-3/2}$ tailing (left) and exponential tailing (right). Blue dots and bars indicate measured breakthrough and the given uncertainty region of the measurement. Coloured lines represent fitted breakthrough curves for different correlation lengths of the velocity profile. In the left-hand figure the curves for the 0.05- and 0.1-m correlation lengths overlap.

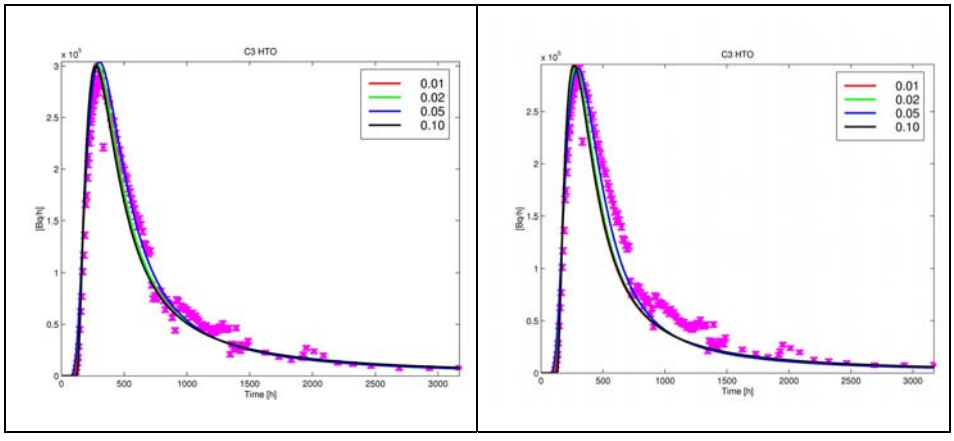

Figure 4-22. Fitted breakthrough curves for HTO in C3. Results for the extrapolation of the final recovery by using ~$t^{-3/2}$ tailing (left) and exponential tailing (right). Blue dots and bars indicate measured breakthrough and the given uncertainty region of the measurement. Coloured lines represent fitted breakthrough curves for different correlation lengths of the velocity profile. In the left-hand figure the curves for the 0.02-, 0.05-, and 0.1-m correlation lengths overlap.

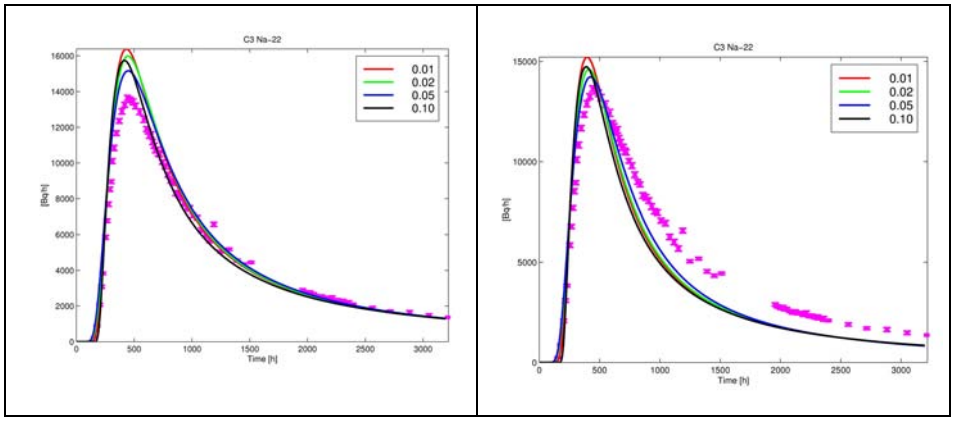

Figure 4-23. Fitted breakthrough curves for Na-22 in C3. Results for the extrapolation of the final recovery by using ~$t^{-3/2}$ tailing (left) and exponential tailing (right). Blue dots and bars indicate measured breakthrough and the given uncertainty region of the measurement. Coloured lines represent fitted breakthrough curves for different correlation lengths of the velocity profile.

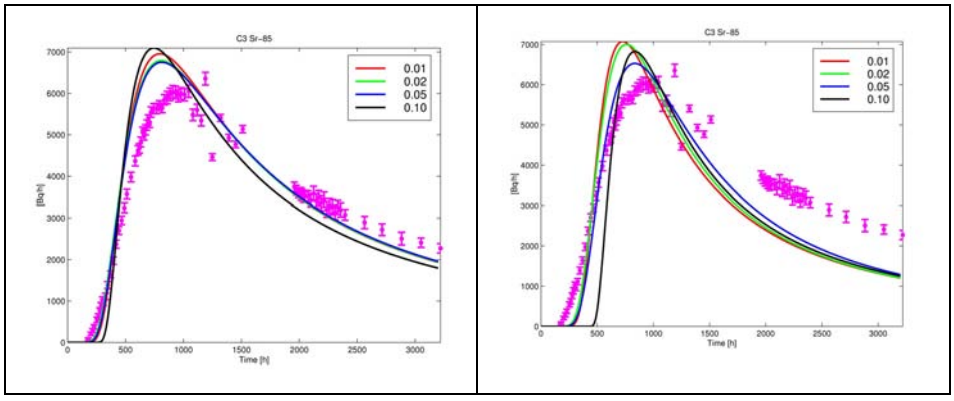

Figure 4-24. Fitted breakthrough curves for Sr-85 in C3. Results for the extrapolation of the final recovery by using ~$t^{-3/2}$ tailing (left) and exponential tailing (right). Blue dots and bars indicate measured breakthrough and the given uncertainty region of the measurement. Coloured lines represent fitted breakthrough curves for different correlation lengths of the velocity profile.

4.8 Variants of the immobile zones

4.8.1 Matrix diffusion to rock matrix only

An attempt was made to explain the measured breakthrough curves by diffusion into the rock matrix. Laboratory data on the sorption and porosity properties in the rock matrix are available (altered and unaltered Äspö diorite, Byegård et al., 1998). The laboratory data were used to narrow down the variability of the evaluated sorption properties along the transport paths. In practice, the laboratory data were applied as the upper limit of the K_d and porosity values (see Table 4-2).

The transport of the tracers is modelled using Equations (4-4) and (4-10). This means that the transport is parameterised by U and R_a. Retention parameters were calculated only for the extrapolated ~$t^{-3/2}$ tailing (alternative 1 in the tables), because it gave a better fit to the measured breakthrough curves. The results of the interpretation are presented in Table 4-9. Porosity, K_d, and geometric factors reach the upper allowed value. In addition, a quite small aperture is required to reproduce the observed retention. The flow rate through the transport channel is fixed in the model, so the small aperture indicates a wide transport channel.

The evaluation results are judged on the basis of the fitted geometry of the transport channel. In practice, this means that the uncertainty of the grouped retention parameter U is accumulated to the flow field part of the parameter U. Note that the flow field part of the retention parameter cannot be constrained by using independent data, because there is information on the flow field only at the injection and pumping locations.

Modelling shows that if the observed retention is caused by diffusion into the rock matrix only, then the width of the transport channels needs to be unrealistically large, almost of the same order of magnitude as the path length. It seems unrealistic that the retention has been caused by diffusion to the rock matrix alone.

Table 4-9. Retention parameters in the case of diffusion into the pore space of the rock matrix. The correlation length of the velocity field is denoted by a_v, the calculated retention parameter of the rock matrix is U_{tr}, and the retention parameter fitted to the measured breakthrough curve is U_{tf}.

		Channel characteristics						
Test Tracer	K_d [m^3/kg]	**flow rate [ml/h]**	v_0 [m/h]	**Aperture [m]**	**width [m]**	a_v [m]	U_{tr} [$h^{-1/2}$]	U_{tf} [$h^{-1/2}$]
C1, Br-82	0	2700	1.67	6.50E-05	49.64	0.02	0.023	0.0600
C1, Na-24	6.00E-05	2700	1.67	6.50E-05	49.64	0.02	0.120	0.1149
C1, Ca-47	1.45E-04	2700	1.67	6.50E-05	49.64	0.02	0.185	0.1990
C1, K-42	4.00E-04	2700	1.67	6.50E-05	49.64	0.02	0.306	0.3351
C1, Rb-86	2.00E-03	2700	1.67	6.50E-05	49.64	0.02	0.683	0.7071
C1, Cs-134	1.52E-02	2700	1.67	6.50E-05	49.64	0.02	1.883	1.8407
C2, Re-186	0	600	1.54	7.30E-05	10.70	0.05	0.020	0.0738
C2, Ca-47	1.45E-04	600	1.54	7.30E-05	10.70	0.05	0.165	0.1652
C3, HTO	0	112	0.32	1.07E-04	6.50	0.05	0.014	0.0387
C3, Na-22	6.00E-05	112	0.32	1.07E-04	6.50	0.05	0.073	0.0727
C3, Sr-85	1.80E-04	112	0.32	1.07E-04	6.50	0.05	0.125	0.1251

4.8.2 Matrix diffusion to fault gouges only

Fault gouges were found in the structures of the TRUE Block Scale site (Andersson et al., 2002b) and the retention properties of the gouge (K_d and porosity) were studied (see Table 4-2). It is possible that the flow paths of the Phase C tracer tests also contain fault gouges and diffusion to the pore space of the fault gouges is a possible retention mechanism.

The transport of the tracers is modelled using Equations (4-4) and (4-10). Interpretation of the alternative models was carried out only for power-law tailings ($\sim t^{-3/2}$, alternative 1 in the tables). The results of the interpretation are presented in Table 4-10. Porosity, K_d, and the geometric factor of the pore diffusivity reach the upper limit that was set for them on the basis of the data in Table 4-2, as in the case of diffusion to the rock matrix. It is not possible to fit an entire set of different tracer tests equally well. It is possible to get the sorbing tracers to behave quite consistently, but then the non-sorbing tracers do not show enough retention (i.e. the U_{tf} fitted to the breakthrough curve is larger than the U_{tg} that is calculated from the selected parameters).

The channel width required to produce the observed retention is much more reasonable than in the case of retention mainly attributed to the rock matrix. In the C1 test (highest flow rate) the channel needs to be about 4 m wide and about 1 m in the C2 and C3 tests. On the basis of the evaluated channel geometry, it seems more reasonable that the observed retention is mainly a result of diffusion to the fault gouge than to the rock matrix. At least, this may explain the retention of the sorbing tracers.

It is noted that the fault gouge variant is evaluated assuming the immobile zone to be of infinite thickness. It is possible that the smallest fault gouge particles get saturated by the tracer, which will cause them to show an equilibrium-sorption type of retention.

Table 4-10. Retention parameters in the case of diffusion to the pore spaces of the fault gouge that are less than 0.125 mm in diameter. The correlation length of the velocity field is denoted by a_v, the calculated retention parameter of the fault gouge is U_{tg}, and the retention parameter fitted to the measured breakthrough curve is U_{tf}.

Test Tracer	K_d [m^3/kg]	Channel characteristics: flow rate [ml/h]	v_0 [m/h]	Aperture [m]	width [m]	a_v [m]	U_{tg} [$h^{-1/2}$]	U_{tf} [$h^{-1/2}$]
C1, Br-82	0	2700	1.67	6.20E-04	5.20	0.02	0.012	0.0600
C1, Na-24	2.20E-04	2700	1.67	6.20E-04	5.20	0.02	0.054	0.1149
C1, Ca-47	1.30E-03	2700	1.67	6.20E-04	5.20	0.02	0.128	0.1990
C1, K-42	5.20E-03	2700	1.67	6.20E-04	5.20	0.02	0.255	0.3351
C1, Rb-86	2.80E-02	2700	1.67	6.20E-04	5.20	0.02	0.592	0.7071
C1, Cs-134	2.80E-01	2700	1.67	6.20E-04	5.20	0.02	1.872	1.8407
C2, Re-186	0	600	1.54	4.80E-04	1.63	0.05	0.015	0.0738
C2, Ca-47	1.30E-03	600	1.54	4.80E-04	1.63	0.05	0.165	0.1652
C3, HTO	0	112	0.32	4.50E-04	1.54	0.05	0.016	0.0387
C3, Na-22	2.20E-04	112	0.32	4.50E-04	1.54	0.05	0.074	0.0727
C3, Sr-85	6.50E-04	112	0.32	4.50E-04	1.54	0.05	0.125	0.1251

4.8.3 Matrix diffusion to the stagnant zones of the flow field

The alternative of diffusion to the stagnant zones was examined mainly because non-sorbing tracers showed too-low retention in the case of diffusion to the fault gouge or rock matrix. The approach is the same one that was applied in the evaluation of retention to the rock matrix or fault gouges. The retention parameter U_t values are explained by diffusion to the stagnant zones. The difference compared to the fault gouge and rock matrix cases is that diffusion does not take place in the direction of the fracture aperture but laterally, in the fracture plane from the flow channel. This means that the fracture geometry, i.e. the fracture aperture, should be determined in advance. The stagnant zone variant is based on the aperture estimates of the fault gouge case.

The porosity constraint for the stagnant zone is selected to be rather high, 50%. This means that on the average the stagnant zone is available for half of

the length of the flow path. The retention parameters for the stagnant zone case are presented in Table 4-11. All the parameters except the mean lateral distance between the stagnant zones ($2a_s$) are fixed ($\varepsilon_s = 0.5$, $D_w = 10^{-9}$ m^2/s and R_a fitted).

The results of the stagnant zone variant appear to be quite consistent with the modelling, resulting in correlation lengths of variable velocity. This model also gives the required additional retention of the non-sorbing tracers but at the same time the contribution to the retention of the sorbing tracers remains at a reasonably low level so that a joint model of the fault gouge and stagnant zones (i.e. $U_{tg}+U_{ts}$ in Tables 4-10 and 4-11) may explain the observed retention. However, the model is based on the unproven assumption that the stagnant zones or fault gouge do not get saturated by the solute. The question of the limited volume of immobile zones is studied later in connection with heterogeneous rock matrix.

Table 4-11. Retention parameters in the case of diffusion to the stagnant zones. The correlation length of the velocity field is denoted by a_v, the calculated mean lateral distance between the stagnant zones in the fracture is a_s, the calculated retention parameter of the stagnant zones is U_{ts}, and the retention parameter that is fitted to the measured breakthrough curve is U_{tf}.

Test Tracer	R_a [-]	Channel characteristics: flow rate [ml/h]	v_0 [m/h]	Aperture [m]	a_s [m]	a_v [m]	U_{ts} [h$^{-1/2}$]	U_{tf} [h$^{-1/2}$]
C1, Br-82	1.00	2700	1.67	6.20E-04	0.0245	0.02	0.055	0.0600
C1, Na-24	1.12	2700	1.67	6.20E-04	0.0245	0.02	0.058	0.1149
C1, Ca-47	1.30	2700	1.67	6.20E-04	0.0245	0.02	0.062	0.1990
C1, K-42	1.40	2700	1.67	6.20E-04	0.0245	0.02	0.065	0.3351
C1, Rb-86	3.00	2700	1.67	6.20E-04	0.0245	0.02	0.095	0.7071
C1, Cs-134	16.05	2700	1.67	6.20E-04	0.0245	0.02	0.219	1.8407
C2, Re-186	1.00	600	1.54	4.80E-04	0.028	0.05	0.048	0.0738
C2, Ca-47	2.40	600	1.54	4.80E-04	0.028	0.05	0.074	0.1652
C3, HTO	1.00	112	0.32	4.50E-04	0.055	0.05	0.024	0.0387
C3, Na-22	1.30	112	0.32	4.50E-04	0.055	0.05	0.028	0.0727
C3, Sr-85	2.09	112	0.32	4.50E-04	0.055	0.05	0.035	0.1251

4.9 Integrated retention model of the Phase C tracer tests

The integrated retention model of the Phase C tracer tests is based on evaluated transport properties caused by advection, advection-dispersion, and solute diffusion to the immobile pore space. The aim is to construct a model of the C1, C2, and C3 flow paths that is able to explain observed retention and, at the same time, give a concrete and consistent picture of the flow path geometries and main retention processes. The approach is to start from the flow field and then take into account the joint effects of surface sorption, diffusion to the immobile pore spaces, and sorption in the immobile pore space.

Flow field

Tracer tests C1, C2, and C3 were evaluated using different correlation lengths of the velocity variation of the flow field. The calculated cases cover both purely advective and advection-dispersion-type transport. Examination of the non-sorbing tracer transport shows that in the case of the C1 test a simple advective velocity field cannot explain the breakthrough curve, especially in the early stages. Shortening the correlation length gives better results. The correlation length of the velocity field in the C1 test needs to be on the centimetre scale. Similar conclusions can also be drawn from the non-sorbing breakthrough curves of the C2 and C3 tests. It seems clear that the spatial correlation length of the velocity variantion cannot be on the decimetre scale in any of the tests.

A conceptual illustration of the flow field is presented in Figure 4-25. Diffusion to the rock matrix or fault gouge has been found to be a secondary retention process for non-sorbing tracers. This means that the non-sorbing tracer data cannot be used for the estimation of the geometry of the flow channel (aperture and width). However, the volume of the flow channel could be constrained by the non-sorbing tracer data (cf. Equation (4-9)).

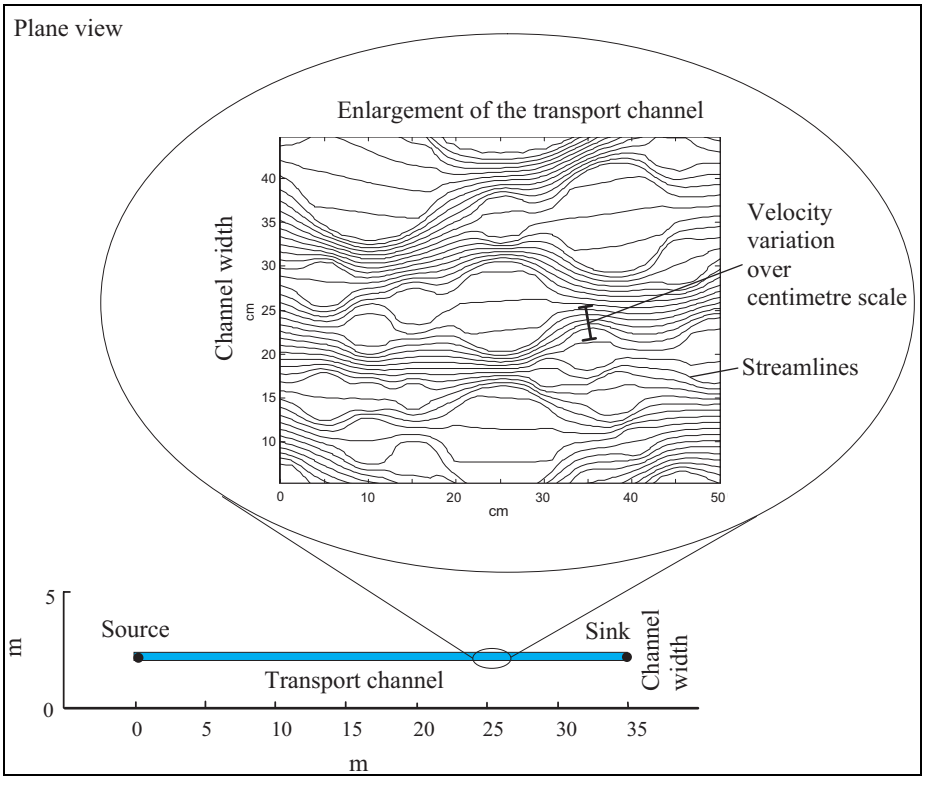

Figure 4-25. Conceptual illustration of the advective flow field based on the evaluation of the non-sorbing tracer test data.

The advective flow field and molecular diffusion between the streamlines (Taylor dispersion) cannot alone explain the measured breakthrough curves. Best-fit breakthrough curves with and without diffusion to the immobile zones were calculated to test this question. Best-fitting breakthrough curves for the case of mobile pore space only are presented in Figure 4-26. Clearly, the observed breakthrough curves show more tailing than the modelled advection-dispersion breakthrough curves. Cases with diffusion to the immobile zones give a better fit. The evaluation also showed that diffusion to the rock matrix or fault gouge was not able to produce enough retention for non-sorbing tracers. This means that diffusion to the stagnant zones of the flow field could be important for non-sorbing tracers.

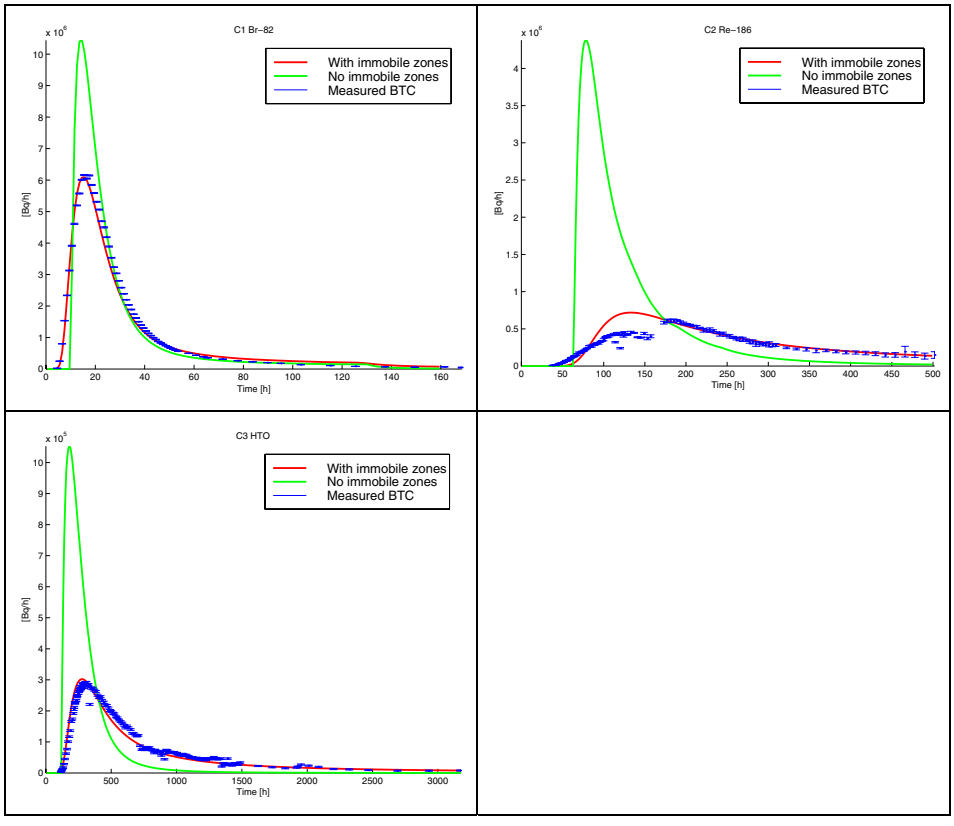

Figure 4-26. Non-sorbing tracer breakthrough curves with and without diffusion to the immobile zones.

Surface sorption

The measured breakthrough curves cannot be explained by flow field and surface sorption alone. This can be tested using measured non-sorbing tracer data. If surface sorption or some other equilibrium sorption is the major retention mechanism, then it should be possible to get the breakthrough curves of different sorbing tracers to coincide by scaling the time axis. This is not the case with the measured breakthrough curves (see Figures 4-11 to 4-13).

Although surface sorption cannot alone explain retention, it is still an important part of the overall retention. In the present modelling approach the overall retention is assumed to follow from both surface sorption and matrix diffusion, but in practice there is no unique way to divide the overall retention between matrix diffusion and surface sorption. It is possible to get a reasonable fit without surface sorption or using very moderate surface sorption, but in that

case the estimated matrix diffusion parameters should show matrix diffusion that is too unrealistically strong to be explained by e.g. available data on sorption and porosity properties.

Rock matrix

It seems quite unlikely that diffusion to the rock matrix is the dominant retention process. Using commonly accepted values for the rock matrix retention properties requires fracture apertures to be less than 0.1 mm. On the other hand, the volume of the channel controls the residence times of the non-sorbing tracers. Integrating these two results indicates that effective transport channel widths should vary from about 6.5 m to 50 m. These average channel widths are too close to the channel lengths to be realistic.

Fault gouge

Assessing the channel width using the retention properties of the fault gouge instead of the rock matrix leads to a much more realistic geometry of the transport channel. The apertures of the fractures need to be approximately 0.4 mm to 0.6 mm, which leads to flow channel widths in the range from about 1.5 m to 5.2 m. These are much more reasonable geometries than in the case of retention in the rock matrix. In particular, it is easier to explain the retention of the sorbing tracers by diffusion to the fault gouge.

The measured breakthrough curves of the non-sorbing tracers show more retention than the fault gouge model is able to provide. This implies the presence of other retention processes that are more dominant for non-sorbing than sorbing tracers. Evaluation of the tracer tests suggests that this process could be diffusion to the stagnant zones of the flow field.

4.10 Conclusions

Evaluation of the Phase C tracer tests indicates that the main retention processes are surface sorption, diffusion to the pore space of the fault gouge for the sorbing tracers, and diffusion to the stagnant zones for the non-sorbing tracers. The relative importance of diffusion to the stagnant zones and fault gouges for the least sorbing tracers was not directly examined but results indicate that diffusion to the stagnant regions may also be an important process for the least sorbing tracers.

The developed transport channels are illustrated and quantified by combining the results of the flow field analysis and diffusion to the fault gouges. Channel apertures vary from 0.45 to 0.62 mm and average channel width from 1.5 to 5.2 m, depending on the flow path. The flow field analysis carried out for the non-sorbing tracers gives the best results if the correlation length of the velocity variation is on the centimetre scale. On the other hand, diffusion to the stagnant zones gives reasonable retention for the least sorbing and non-sorbing tracers if the mean distance between the stagnant zones is about 2-5 cm. These two results are mutually consistent if it is assumed that the same phenomena in the flow field produce both the stagnant zones and the variation in velocity. This kind of process can be, for example, channelling of the flow resulting from obstacles or low-aperture regions in the flow channels.

A conceptual illustration of the developed transport channels that is based on the evaluation is presented in Figure 4-27.

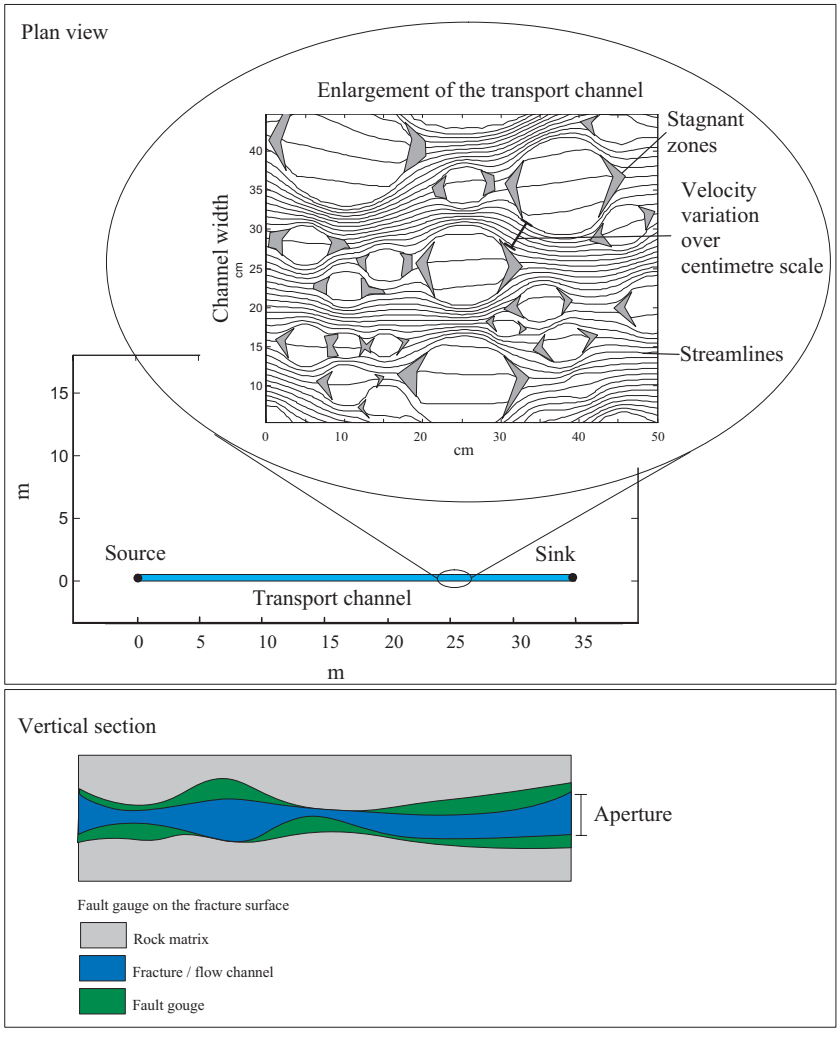

Figure 4-27. Conceptual illustration of the transport channels based on the evaluation. The evaluation suggests that the main retention processes are surface sorption, diffusion to the fault gouge, and diffusion to the stagnant zones of the flow field.

5. Heterogeneous rock matrix

5.1 Experimental site

A new set of tracer tests was performed at the TRUE Block Scale site (cf. Figure 4-1). Earlier tracer tests indicated increased tracer retention in the in situ tracer tests compared to the laboratory data available. The new tracer tests aimed to study the possible influence of high-porosity immobile zones, such as fault gouges and wall rock rim zones (Figure 5-1).

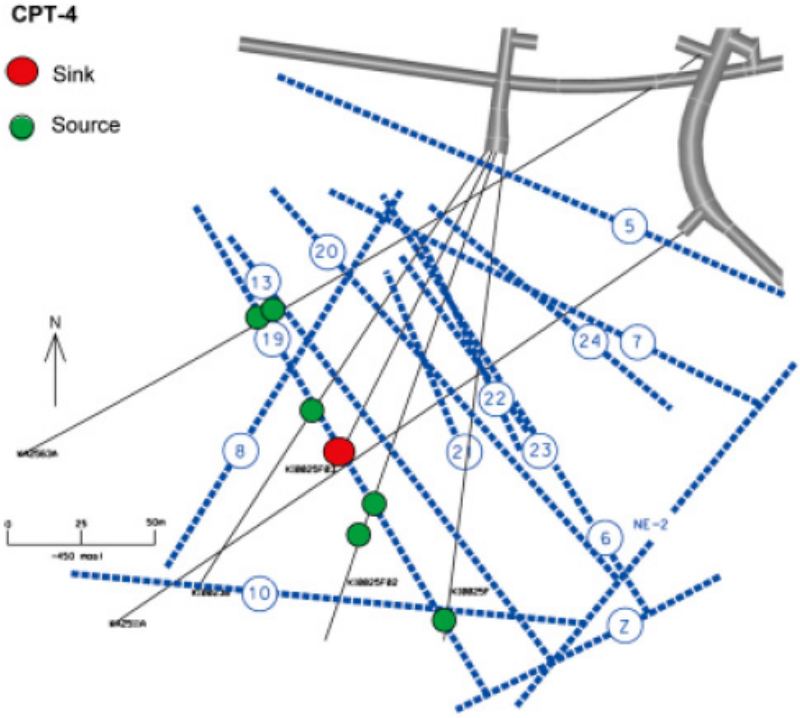

Figure 5-1. Experimental site of the TRUE Block Scale Continuation project. Tracer test were performed around the structure #19 (from Andersson et al., 2007).

5.2 Flow paths

Two flow paths were tested; one of the paths is along a larger and more heterogeneous structure (structure #19) and the other path also involves a low-transmissive background fracture.

Two different injection sections were used. Both injection sections are located in the borehole (KI0025F02). One of the injection locations is in the same hydraulic feature as the extraction borehole. This flow path is denoted as Flow Path I (FPI) and it only goes along Structure #19. The second flow path, Flow Path II (FPII), starts from a background fracture denoted by BG1 that is sub-parallel to Structure #19.

Figure 5-2 shows the overall geometry applied in the tests. Figures 5-3 and 5-4 show the flow paths from different angles and on variable scales. The distance between the injection and extraction points in Structure #19 (Flow Path I) is about 20 m. The length of the flow path from BG1 to the extraction borehole is not known exactly. In this study it is assumed that the connection from BG1 to the extraction borehole takes place directly by way of BG1 alone. Extending BG1 to intersect Structure #19 indicates that the path length along BG1 to Structure #19 is about 15 m, although the shortest distance from the BG1 injection point to Structure #19 is only 3.3 m (i.e. BG1 and Structure #19 are subparallel). The path length along Structure #19 to the sink from the assumed intersection of BG1 and Structure #19 is about 23 m. The distance from the source in BG1 to the sink is about 22 m, i.e. the projected path length along BG1 to Structure #19, and then the added distance along Structure #19 to the sink is 15 m + 23 m = 38 m, which is almost twice the distance from the source to the sink. Predictions were calculated using the assumption that the path length along Structure #19 is 20 m for both Flow Path I and Flow Path II. The path length along BG1 for Flow Path II is also assumed to be about 20 m. This makes the lengths of the flow paths about 20 m for Flow Path I and about 40 m for Flow Path II. It is again stressed that the details of the connection and the length of the path from BG1 to Structure #19 are not fully known.

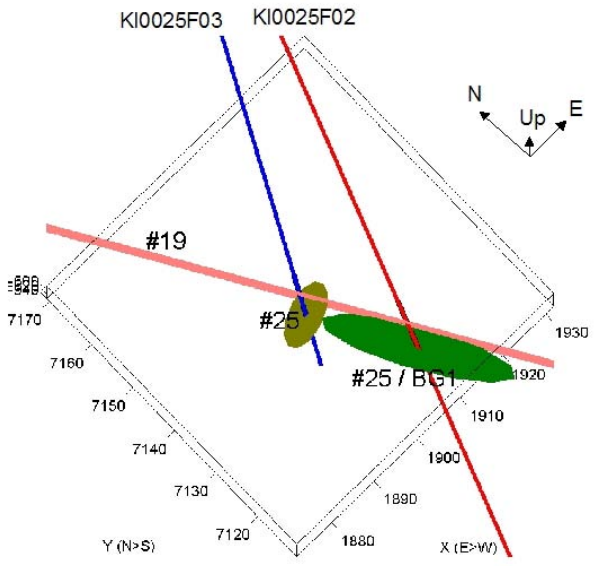

Figure 5-2. Horizontal cross-section of the BS2B area. The view is downward from the upper south-west corner of the BS2B block (in the figure the south-west is at the bottom and the north-east at the top). Extraction borehole KI0025F03 (blue) and injection borehole KI0025F02 (red). Structure #19 is indicated by a pink plane and BG1 is shown in green. Originally BG1 was named Structure #25, which was also identified in borehole KI0025F03. This intersecting feature is also indicated in the figure (light green).

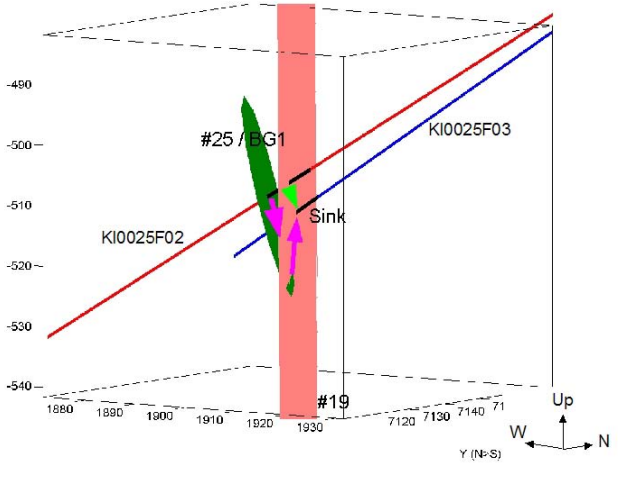

Figure 5-3. Vertical cross-section of the area of the BS2B test showing injection (red) and sink (blue) boreholes together with Structure #19 and fracture BG1. The view is horizontally from the south-east towards the north-west. Flow Path I is shown by a green arrow and Flow Path II by a magenta arrow.

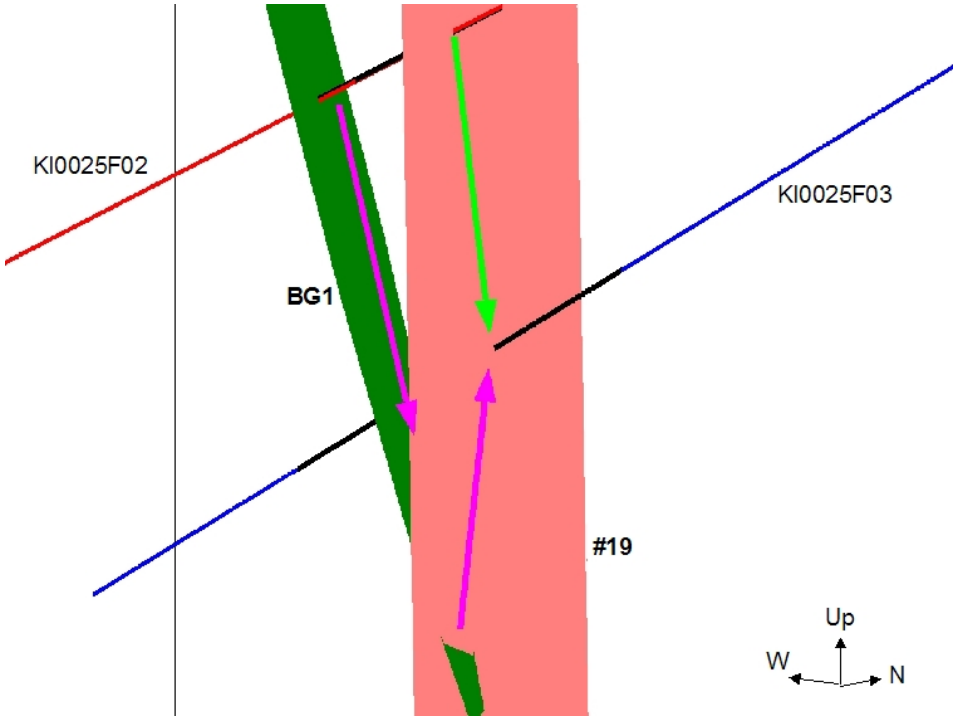

Figure 5-4. Close-up of Figure 5-3. Vertical cross-section of the BS2B area showing injection and sink (blue) boreholes together with Structure #19 and fracture BG1. The view is horizontally from the south-east towards the north-west. Flow Path I is shown by a green arrow and Flow Path II by magenta arrows.

5.3 Immobile pore spaces

The distribution of the immobile pore space has been defined for the structures in the BS2 experimental area (Tullborg and Hermanson, 2004). The definition of the immobile pore space follows the approach applied in Task 6 of the Äspö Task Force (Dershowitz et al., 2003). The hydraulic structures involved in the experiment are divided into two different classes named “Type 1” and “Type 2”. Type 1 is a fault-type feature and Type 2 is a non-fault-type feature. The immobile pore space in both types is made up of layers of different pore spaces, as shown in Figure 5-5. Tullborg and Hermanson (2004) interpreted Structure #19 as a fault-type feature (Type 1) and fracture BG1 as a non-fault type feature (Type 2). Material property parameters for the different layers making up the structure types are given in Table 5-1.

Figure 5-5 also shows that the layers are always arranged in order of decreasing porosity; for example, there is no coating at the top of the fault gouge (cf. also coating, cataclasite, and gouge to e.g. altered rock). In the current evaluation model the microstructural model is equated by an equivalent system of a more symmetric pore space structure, as shown in Figure 5-5.

The micro-structural model also includes a characteristic called the complexity factor. This indicates the number of parallel water-conducting fractures in the structure. In Structure #19 the complexity factor varies from 1 to 3 and for BG1 it is 1. However, in the current modelling both features are assumed to contain one water-conducting fracture. This is based on the observation that the flow rate is usually distributed unevenly between parallel fractures. This means that from a transport point of view one of the subparallel water-conducting fractures dominates. This is also supported by the usually applied estimate that fracture transmissivity depends on the cube of the fracture aperture.

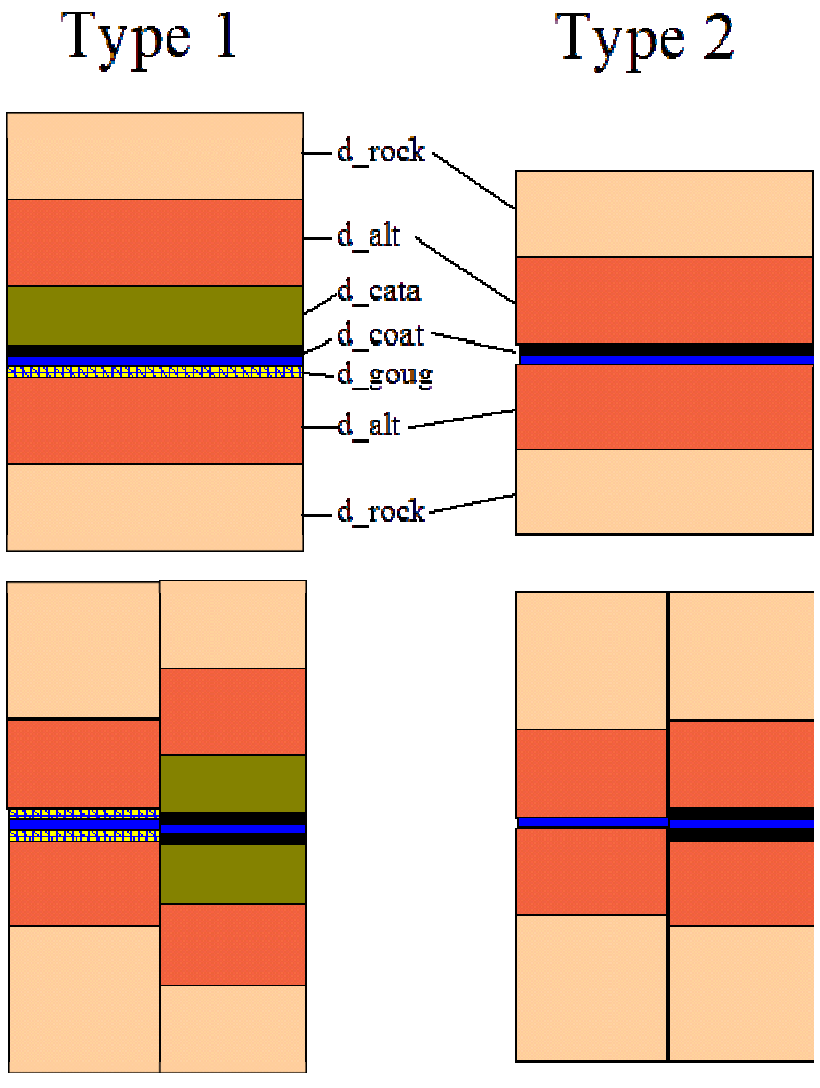

Figure 5-5. Hydraulic features are classified into two different types according to the internal structure of the immobile pore space. The micro-structural model of the different structure types is composed of layers of different geological materials. The notation of Type 1 and Type 2 structures is shown at the top. The representation of the Type 1 and Type 2 features in the current evaluation model is shown at the bottom of the figure. The model cannot directly handle the original asymmetric distribution of the immobile pore space (e.g. coating and gouge). It is represented in the current model by an equivalent but more symmetric structure, as shown at the bottom of the figure. From the transport point of view these two representations are equivalent (retention by matrix diffusion is the same).

Table 5-1. Properties of the immobile pore space for Type 1 and Type 2 structures (Tullborg and Hermanson, 2004); cf. Figure 5-5.

Type 1 (fault)			
Rock type	**Extent [cm]**	**Porosity [%]**	**Formation factor [-]**
Intact wall rock (d_rock)	-	0.3	7.3e-5
Altered zone (d_alt)	15	0.6	2.2e-4
Cataclasite (d_cata)	1	1	4.9e-4
Fault gouge (d_goug)	0.3	20	5.6e-2
Fracture coating (d_coat)	0.05	5	6.2e-3
Type 2 (non-fault)			
Rock type	**Extent [cm]**	**Porosity [%]**	**Formation factor [-]**
Intact wall rock (d_rock)	-	0.3	7.3e-5
Altered zone (d_alt)	5	0.6	2.2e-4
Fracture coating (d_coat)	0.05	5	6.2e-3

5.4 Evaluation of the retention parameters

The evaluation does not aim at the calibration of the retention properties of the individual tracers in order to obtain the best possible fit between the modelled and measured breakthrough curves. Rather, the approach is to critically bring out the problems and possible contradictions in different models. All the tracers are studied in parallel to obtain indications of the dynamics of the system, instead of individual tracers being considered.

The evaluation concentrates on a few key important processes, sorption and matrix diffusion. Matrix diffusion takes place in the immobile pore space of the geological materials that are next to the flowing channel. The immobile pore space is described by the micro-structural model, which includes different immobile pore spaces: fracture coating, fault gouge, cataclasite, altered wall rock, and intact rock. The aim is to test the micro-structural model, which is composed on a geological bases (cf. Figure 5-5 and Table 5-1).

Three cases were modelled: i) all geological layers included, as given in the definition of the micro-structural model; ii) all layers included but using changed properties for the fault gouge, and iii) only the altered zone and intact rock taken into account. Retention of the tracers depends both on the flow field and the micro-structural model of the pore space. This means that the variants of the micro-structural model should also reflect corresponding differences in the flow field. The basis of the current evaluation is to try to consider how realistic the different variants are and what problems they may entail.

5.4.1 Characteristics of the measured breakthrough curves

It is also possible that some other processes than matrix diffusion and linear equilibrium sorption may affect residence time distributions. For this reason, different tracers are examined in order to judge how reliable the information they can provide on the studied retention processes is.

The tracers used in the BS2B sorbing experiment span a large range of diffusivities and sorption properties. This is essential for the evaluation, but an inevitable consequence of the application of the sorbing tracers is that the recoveries of the most sorbing tracers can be quite low at the termination time of the experiment. This is especially true for Flow Path II (injection in the background fracture BG1), where the recovery of both Mn-54 and Ba-133 is less than 10%. The recovery of Mn-54 is in fact only a couple of per cent.

Source terms

Meaningful evaluation also requires the source term of the tracer to be well defined and the breakthrough curve to reflect the process taking place during the transport through the fracture. To investigate this part of the problem the source terms of the different tracers are plotted in Figures 5-6 to 5-8. For Flow Path II (Figure 5-8) all the source terms show the consistent behaviour of a well-mixed source volume that is diluted by the injection flow rate. Along Flow Path I only Ba-133 shows slight deviation from this behaviour. For Flow Path I there seem to be some problems with Cs-137. The source term of Cs-137 (Figure 5-6 and Figure 5-7) does not follow the typical dilution curve of the other tracers at all. It even shows matrix diffusion-type behaviour of $t^{-3/2}$ tailing (Figure 5-7). To some extent a similar type of behaviour can be seen in the source term of Rb-86. Similar behaviour on the part of the Cs (and also Rb) has already been observed

in the TRUE Block Scale experiment. Andersson et al. (2002a) note that it is possible to explain the power-law behaviour of the Cs in the injection curves by applying non-linear sorption with the Freundlich isotherm.

In summary, it can be concluded that evaluation cannot rely very much on the very low recovery tracers Mn-54 and Ba-133. We also need to be cautious with the responses of Cs-137, and possibly also Rb-86, because their behaviour may include more complicated (chemical) processes that cause their injection curves to deviate from the dilution curve.

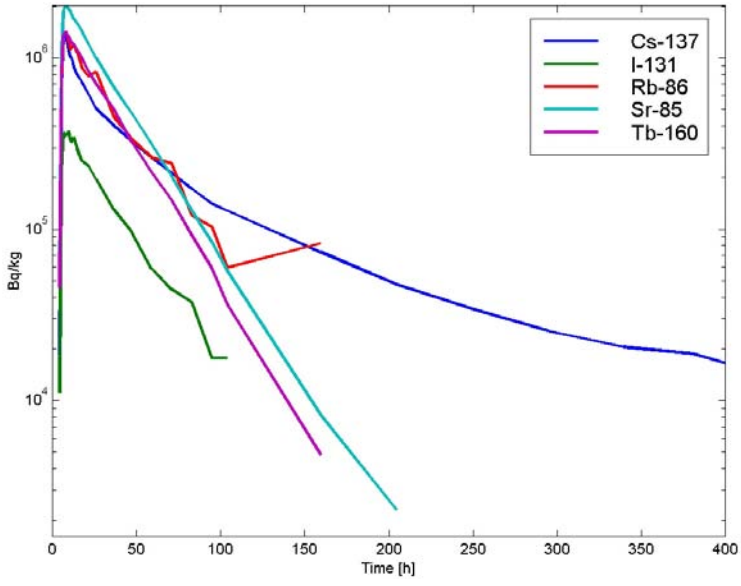

Figure 5-6. Measured source terms of tracers used in Flow Path I (injection in Structure #19) plotted on lin-log scale.

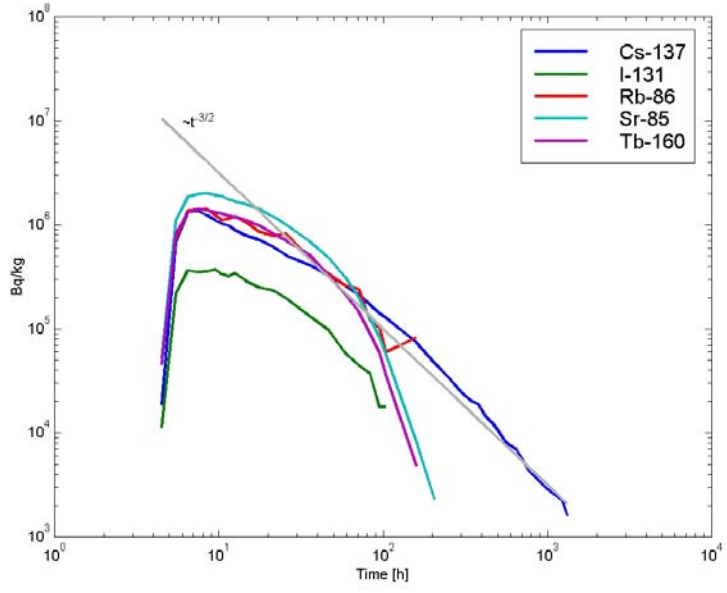

Figure 5-7. Measured source terms of tracers used in Flow Path I (injection in Structure #19) plotted on log-log scale.

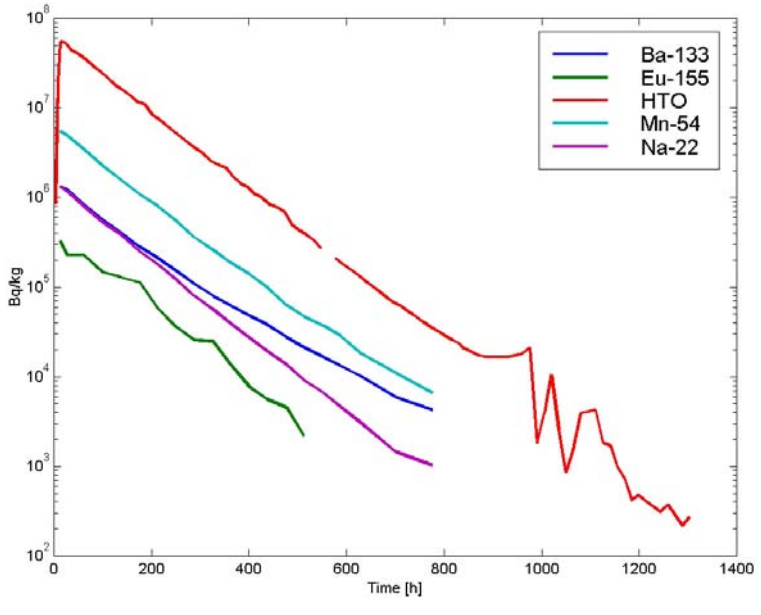

Figure 5-8. Measured source terms of tracers used in Flow Path II (injection in the background fracture BG1) plotted on log-log scale.

Deconvoluted breakthrough curves

The observed tracer breakthrough curves are studied by deconvoluting them with measured source terms. The deconvolutions were performed using Tikhonov regularised inversion of the discretised convolution equations. This should give the response function of the flow path that is characterised only by the transport and retention processes. Figures 5-9 and 5-10 show the deconvoluted response functions and also the reproduced breakthrough curves using the deconvoluted response functions. Deconvolutions were made for non-sorbing tracers that should have the least amount of retention by matrix diffusion. However, along both flow paths the tailings of the response functions show ~$t^{-3/2}$ behaviour, which is typical for unlimited matrix diffusion.

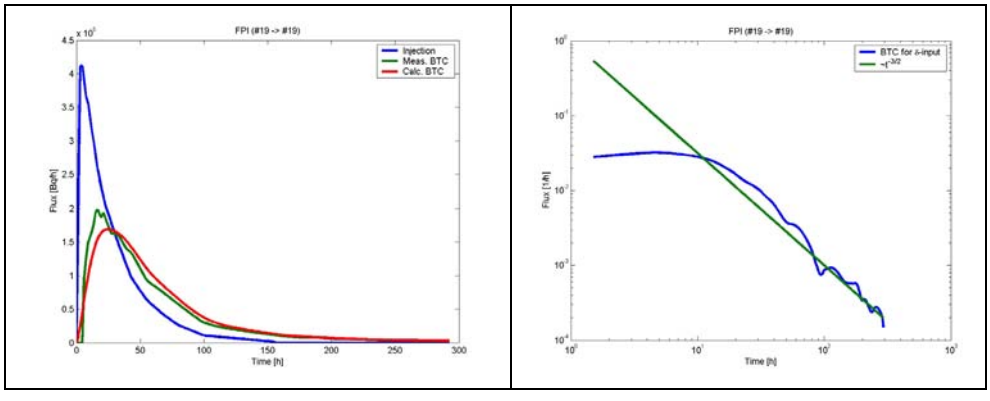

Figure 5-9. Deconvolution of the Tb-160 breakthrough curve for Flow Path I (injection in Structure #19). The right-hand figure shows the deconvoluted response function and the left-hand figure shows the measured injection and breakthrough curves (blue and green) together with the breakthrough curve calculated using the deconvoluted response function (red).

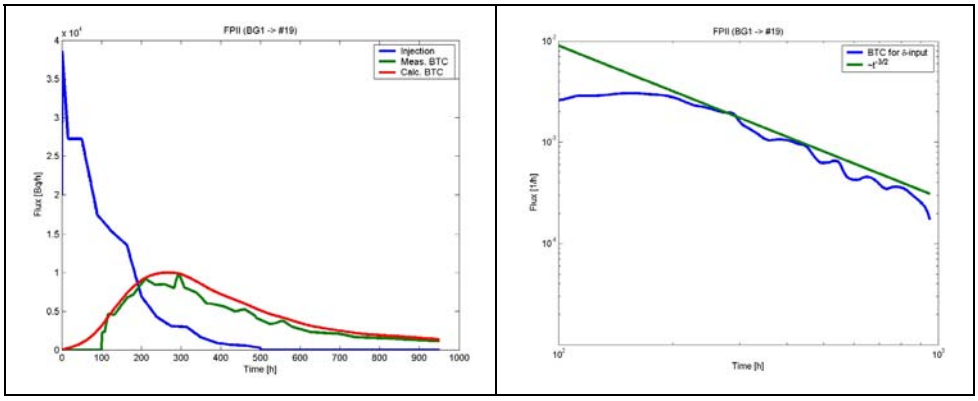

Figure 5-10. Deconvolution of the Eu-155 breakthrough curve for Flow Path II (injection in background fracture BG1). The right-hand figure shows the deconvoluted response function and the left-hand figure shows the measured injection and breakthrough curves (blue and green) together with the breakthrough curve calculated using the deconvoluted response function (red).

It may also be noted that using the solution of the matrix diffusion equation for the delta-input as a response function gives a good fit with the measured breakthrough curves. The procedure is to use the matrix diffusion breakthrough curve for the δ-function release

$$f(t) = \frac{u}{\sqrt{\pi}}\left(t - t_w\right)^{-3/2} \exp\left(-\frac{u^2}{t - t_w}\right). \qquad (5\text{-}1)$$

This function is convoluted with the tracer source term and the resulting breakthrough curve is fitted to the measured breakthrough curve using u as the fitting parameter. It is possible to carry out this fitting procedure with all the other tracers except Cs-137 (Flow Path I), where both the retardation and spreading of the breakthrough pulse were not reproduced by this model, and the low-recovery tracers Ba-133 and Mn-54 (Flow Path II). The resulting calculated breakthrough curves, with the corresponding measured breakthrough curves, are presented in Figure 5-11 and Figure 5-12. The fitted parameters are presented in Table 5-2.

It is also possible to calculate the corresponding u-values for the different layers of the micro-structural model (i.e. coating, fault gouge, cataclasite, altered zones, and intact rock) using Equation (5-2)

$$u = \varepsilon \sqrt{D_p R_p}\, \frac{WL}{Q}, \tag{5-2}$$

where ε is the porosity, D_p is the pore diffusivity, R_p is the retardation factor, and $WL/Q = t_w/2b$ defines the flow field where W is the width of the transport channel, L is the length of the flow channel, Q is the flow rate, t_w is the water residence time, and $2b$ is the transport aperture. Two alternatives for WL/Q are applied; other parameters form the matrix parameter group γ, and are given later in Table 5-7. Parameter values for the flow field applied in this analysis are $WL/Q = 5 \cdot 10^7$ s/m for the tracers along Flow Path I (injection in #19) and $WL/Q = 3.5 \cdot 10^8$ s/m for Flow Path II (injection in BG1). The second alternatives are calculated using a 40-times-higher WL/Q along both flow paths. Estimates of the WL/Q values are based on considerations of the measured (dilution) flow rates in the injection sections during earlier tests and the projected lengths of the flow paths.

The robust comparisons in Figures 5-13 and 5-14 treat all immobile zones as if they were infinite. In particular, limitations on the extent of the coating and fault gouge may affect the results. The charts in Figures 5-13 and 5-14 show the potential retention power of the different geological materials and they also exemplify how large changes in the flow field are required in order to change the principal retention zone retention properties from the fault gouge to the altered zone and still keep the tracer retention unchanged.

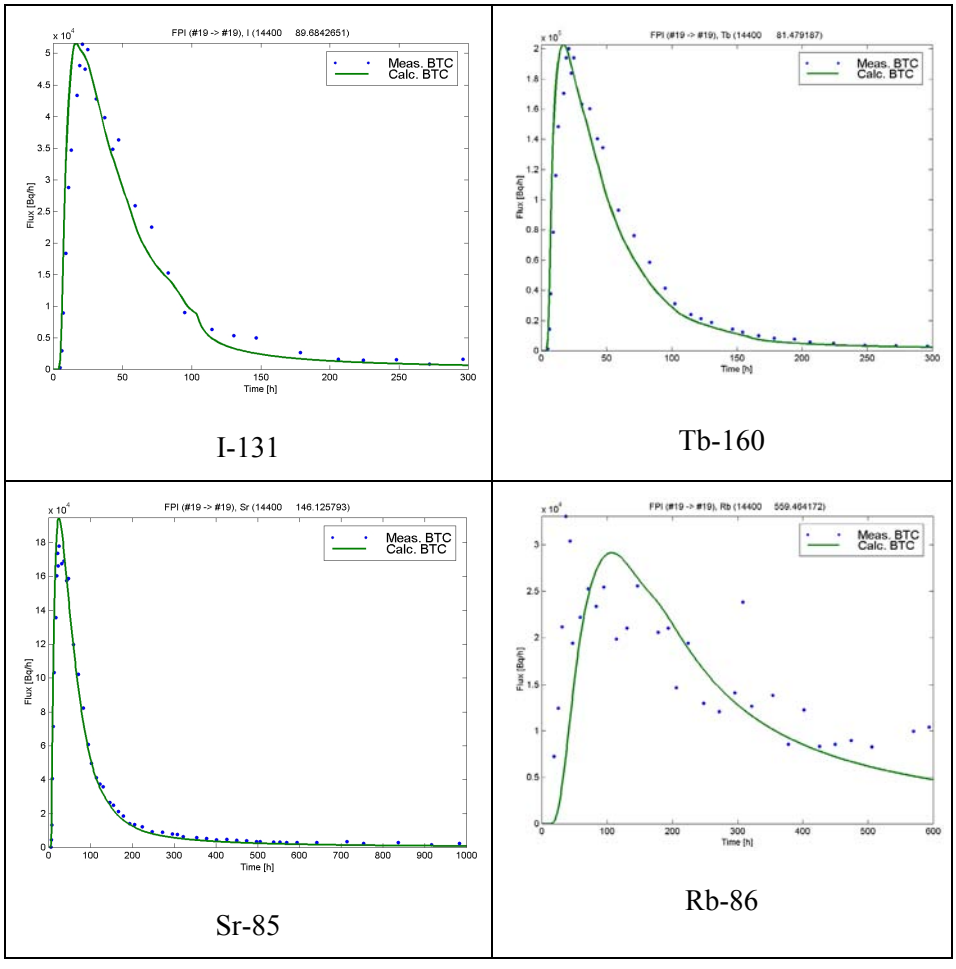

Figure 5-11. Measured (dots) and fitted breakthrough curves for the tracers of Flow Path I (injection in #19). The fitted flow paths are calculated by restricting the tracer response function to the matrix diffusion breakthrough curve for δ-function input (Equation (5-1)) and fitting the parameter *u*. Fitted *u*-values are given in Table 5-2.

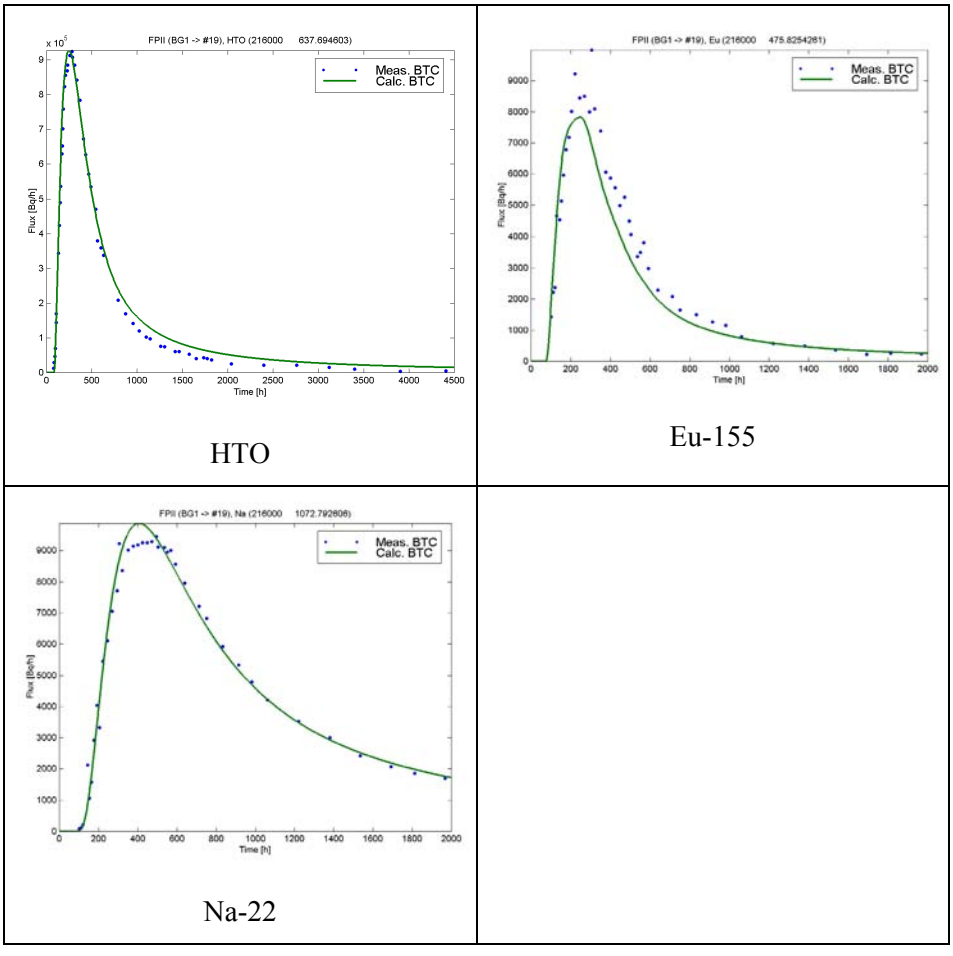

Figure 5-12. Measured (dots) and fitted breakthrough curves for the tracers of Flow Path II (injection in BG1). The fitted flow paths are calculated by restricting the tracer response function to the matrix diffusion breakthrough curve for δ-function input (Equation (5-1)) and fitting the parameter *u*. Fitted *u*-values are given in Table 5-2.

Table 5-2. Parameters of the fitted matrix diffusion response functions (Equation (5-1)) for the different tracers.

Tracer	***u* [sqrt(h)]**	**t_w [h]**
I-131 (Flow Path I)	1.5	4
Tb-160 (Flow Path I)	1.4	4
Sr-85 (Flow Path I)	2.4	4
Rb-86 (Flow Path I)	9.3	4
HTO (Flow Path II)	11	60
Eu-155 (Flow Path II)	7.9	60
Na-22 (Flow Path II)	18	60

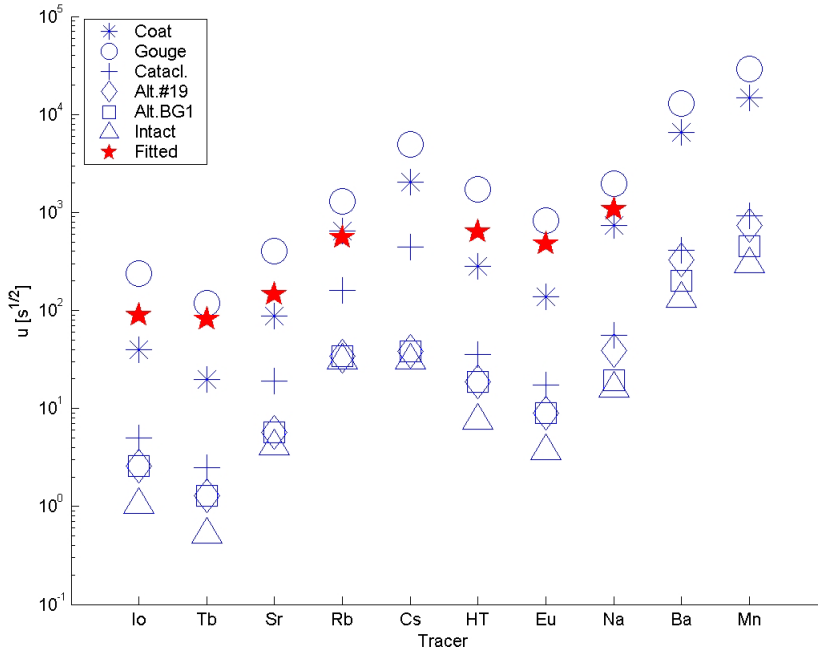

Figure 5-13. Parameter *u*-values (5-2) calculated for different tracers. The *u*-values are calculated using material properties (γ) from Table 5-7 and assuming a flow field that is characterised by the pumping of the borehole sections and the background flow fields ($WL/Q = 5 \cdot 10^7$ s/m for the tracers along Flow Path I and $WL/Q = 3.5 \cdot 10^8$ s/m for the tracers along Flow Path II. The fitted parameter *u*-values (Table 5-2) are indicated by red pentagrams.

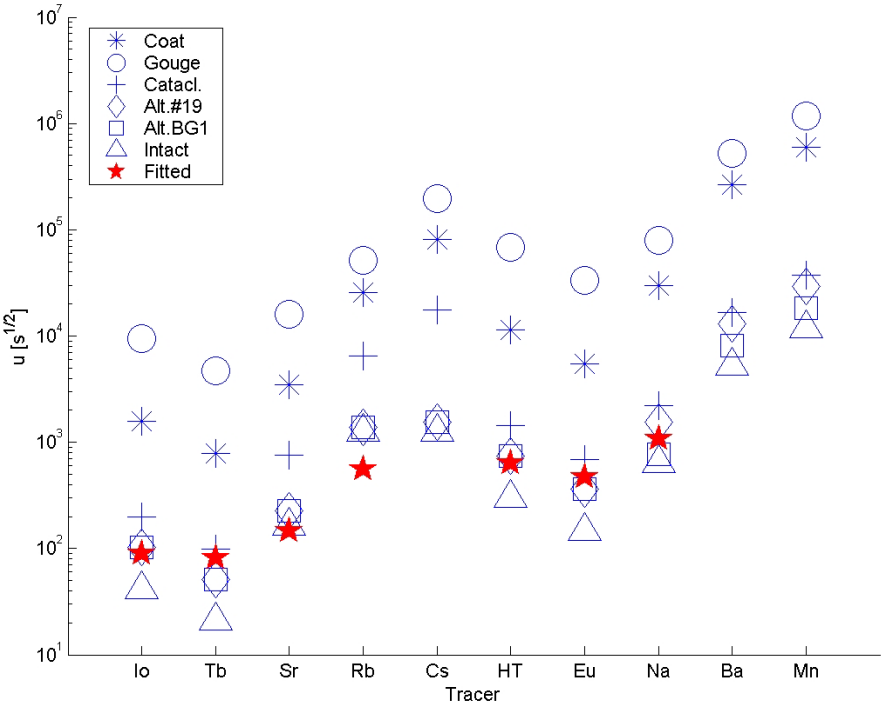

Figure 5-14. Parameter *u*-values (5-2) calculated for different tracers. The *u*-values are calculated using material properties (γ) from Table 5-7 and assuming a flow field that is characterised by a WL/Q 40 times larger than that for Figure 5-13 ($WL/Q = 200 \cdot 10^7$ s/m for the tracers along Flow Path I and $WL/Q = 140 \cdot 10^8$ s/m for the tracers along Flow Path II. The fitted parameter *u*-values (Table 5-2) are indicated by red pentagrams.

5.4.2 Transport model

The transport model takes into account advection along the fractures, matrix diffusion, and sorption in the immobile pore space. Surface sorption on the fracture walls was not modelled, but the diffusion into the pore space of the fracture coating and sorption in the pore space of the coating were directly modelled.

The connection from the source to the sink was described by one transport path for each of the injections. In the prediction model there is no variable advection inside a given transport path. Hydrodynamic dispersion was included only in the evaluation model.

The transport of the tracers is described by applying the advection-matrix diffusion equation

$$\begin{aligned} R_a \frac{\partial c_f}{\partial t} + v\frac{\partial c_f}{\partial x} - 2\frac{D_e}{2b}\frac{\partial c_m}{\partial z}\bigg|_{z=0} &= 0 \\ R_p \frac{\partial c_m}{\partial t} - D_p \frac{\partial^2 c_m}{\partial z^2} &= 0 \end{aligned}, \tag{5-3}$$

where R_a is the retardation coefficient of the surface sorption ($R_a = 1$ for all the tracers in this modelling, i.e. surface sorption is not taken into account in this modelling). The matrix concentration $c_m(x,z,t)$ and fracture concentration $c_f(x,t)$ are coupled by the requirement that $c_m(x,0,t) = c_f(x,t)$. The initial concentration is zero both in the matrix and in the fracture.

The Laplace transform of Equation (5-3) gives

$$\begin{aligned} R_a s\,\bar{c}_f + v\frac{\partial \bar{c}_f}{\partial x} - 2\frac{D_e}{2b}\frac{\partial \bar{c}_m}{\partial z}\bigg|_{z=0} &= 0 \\ R_p s\,\bar{c}_m - D_p \frac{\partial^2 \bar{c}_m}{\partial z^2} &= 0 \end{aligned}, \tag{5-4}$$

where s is the variable of the Laplace domain. Equation (5-4) indicates that the solution could be sought using the product $\bar{c}_m(x,z,s) = f(z)\bar{c}_f(x,s)$ with $f(0) = 1$. This leads to a solution

$$\bar{c}_f(x,s) = C_o \,\mathrm{Exp}\left(-\frac{R_a\, s\, x}{v} + \frac{2\,x\,D_e}{2b\,v} f'(0)\right), \tag{5-5}$$

where *Co* is determined by the source term at the inlet of the flow path (e.g. for step input $c_o\,H(t)$, where H is the Heaviside step-function, it is $C_0 = c_0 / s$. For the Dirac pulse injection $M_0\delta(t)$ it is $C_0 = \frac{M_0}{W(2b)v}\delta(t)$, where W is the width of the flow channel.). Boundary conditions in the immobile pore space of the rock matrix are taken into account by the second equation of (5-4) and they emerge in the solution of the breakthrough curve through the term *f'(0)* (cf. Equation (5-5)). For one homogeneous layer of immobile pore space we get

$$\frac{2\varepsilon D_p}{2bv} f'(0) =$$

$$= -2\sqrt{s}\,\frac{x}{v\,2b}\,\varepsilon\sqrt{D_p R_p}\,\tanh\left(L\sqrt{s\,R_p / D_p}\right), \qquad (5\text{-}6)$$

$$= -\sqrt{s}\,\beta\,\gamma\,\tanh\left(L\sqrt{s\,R_p / D_p}\right)$$

where $\beta = x/(v\,b)$ determines the flow conditions in the transport channel, $\gamma = \varepsilon\sqrt{D_p R_p}$ determines the properties of the immobile region, and L is the thickness of the immobile pore space. This shows that two different immobile regions give the same retention (breakthrough curve) if they have the same γ and $L\sqrt{R_p / D_p}$, i.e. the same grouped matrix properties and the same "diffusion time" through the immobile layer.

Solute transport through the system of layered immobile zones is calculated by constructing an equivalent system of successive flow paths that have homogeneous immobile regions. This can be done if the diffusion property of the immobile layers, i.e. γ, is always smaller for the layer that is deeper in the rock matrix. This is the case in the Type 1 and Type 2 features and for the tracers applied in the BS2B tests. The different layers in both the Type 1 and Type 2 features form a series of decreasing γ from the fracture coating into the intact rock. The modelling approach is explained in greater detail below.

Let us first consider a case where there are two different layers of the immobile pore space that differ only in their porosity (Figure 5-15a). A crucial step of the present approach is to conceptualise the connected porosity that is accessible by diffusion from the fracture as fixed-diameter 1D pipes (Figure 5-15b). This model is not completely equivalent to the concept of a porous medium, because the boundary between the different layers is highly idealised. However, the actual structure of the microfractures and pores in the rock matrix is not known and it is not completely clear how the transition from e.g. more porous altered rock to less porous unaltered rock takes place in reality.

We may arrange the pipes along the flow path in such a way that first there are the long pipes and then the shorter pipes (Figure 5-15c). Changing the order of the pipes does not affect the solute transport, because if the flow path is composed of separate legs then the total output is a convolution between the outputs of the individual legs and the convolution is a commutative operation. This means that a flow path with two layers of immobile pore space is equivalent to a system of two successive flow paths that both have one layer of

immobile pore space according to Figure 5-15d. Note that this is possible only if $\varepsilon_2 < \varepsilon_1$.

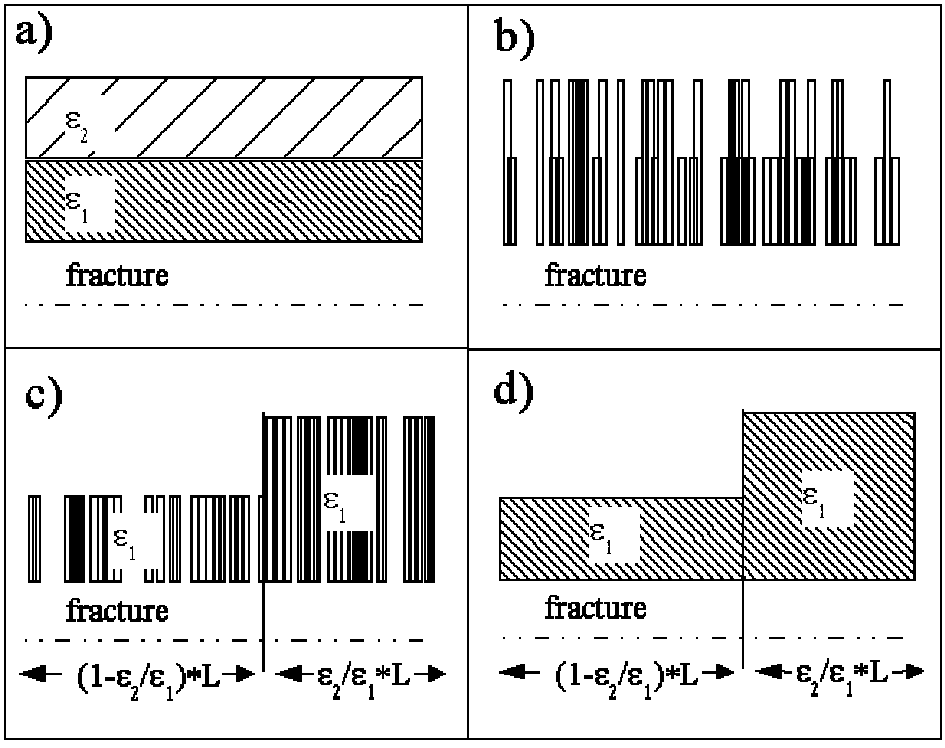

Figure 5-15. Illustration of a flow path along a fracture that is in contact with a heterogeneous immobile pore space. The immobile pore space is composed of two layers that have different porosities ($\varepsilon_2 < \varepsilon_1$, Figure a). The connected porosity is represented by 1D pipes (Figure b). The 1D pores are rearranged to form two successive legs of flow paths that both have one layer of immobile pore space.

The approach used above can be extended to those cases where, in addition to the porosity, diffusivity and sorption properties also vary between the layers. According to Equation (5-6), the breakthrough curve depends on the following parameters: β, which describes the hydrodynamic control of the retention, γ, which describes the properties of the immobile region, and the "diffusion time" through the immobile layer, $\sqrt{T} = L\sqrt{R_p / D_p}$. This means that the breakthrough curves for two flow paths are identical if they have the same β, γ and $L\sqrt{R_p / D_p}$, although the individual ε, D_p, R_p, and L of the immobile regions are different. This is illustrated in Figure 5-16. It shows a breakthrough curve for a transport path that has a groundwater transit time $t_w = 3$ h and

aperture $2b = 1$ mm. The immobile pore space and the tracers are described by two different sets of parameters so that γ and $L\sqrt{R_p / D_p}$ remain unchanged. Figure 5-16 shows that both parameterisations lead to the same breakthrough curves.

Let us now consider a transport path with two layers of immobile regions, such that $\gamma_2 < \gamma_1$, i.e. the layer closer to the fracture has a bigger γ. We may now assign the same D_p and R_p to the second layer as to the first one, but keep the γ_2 unchanged by giving a new porosity for the second layer in such a way that $\gamma_2 = \varepsilon_2 \sqrt{D_{p2} R_{p2}} = \varepsilon'_2 \sqrt{D_{p1} R_{p1}}$. Changing the D_p and R_p of the second layer will affect the "diffusion time" of the second layer. This can be compensated by changing the thickness of the second layer by the factor of $\sqrt{D_{p1} / R_{p1}} \Big/ \sqrt{D_{p2} / R_{p2}}$. It was originally required that $\gamma_2 < \gamma_1$, which means that $\varepsilon'_2 < \varepsilon_1$. After these modifications, the two-layer case, in which all parameters (D_p, R_p, ε, and L) may have been different for different layers, is now represented by, in a transport sense, an equivalent system where the two layers vary only in their porosity. This means that the procedure shown in Figure 5-15 is also applicable for the general case, assuming that $\gamma_2 < \gamma_1$ (cf. Figure 5-17).

It is straightforward to take the next step to a case with several immobile layers. First, to apply this procedure the diffusion properties through the immobile layers should be changed in such a way that $\gamma_m < \gamma_n$ if the layer *m* is deeper in the fracture wall rock than the layer *n* (Figure 5-17). We divide the flow path into as many legs as there are immobile layers. Starting from the layer that has the smallest γ (the layer that is furthest from the fracture), we immediately see that the location of the leg *m* along the flow path is $[\gamma_{m-1}/\gamma_1,\ \gamma_m/\gamma_1]$ L; cf. Figure 5-17. The diffusion property of all the legs is γ_1 and the thickness of the immobile layer *m* should be scaled by $L'_m = L_m \sqrt{D_{p1} / R_{p1}} \Big/ \sqrt{D_{pm} / R_{pm}}$ to keep the diffusion time unchanged (see Figure 5-17).

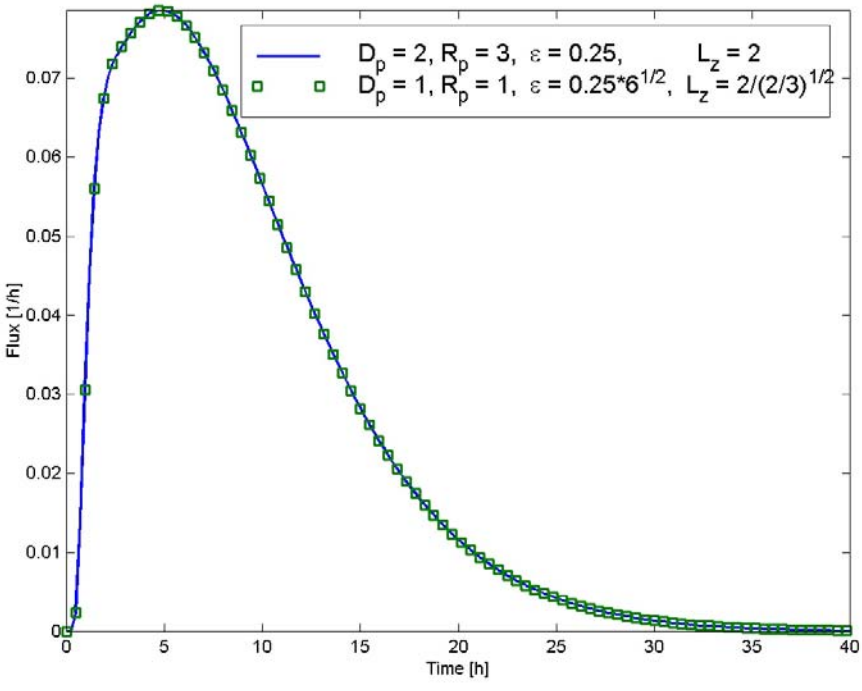

Figure 5-16. Coinciding breakthrough curves for a transport path having the properties t_w = 1 h, 2b = 1 mm and two different immobile layers. The results coincide because in both parameterisations $\gamma = \varepsilon\sqrt{D_p R_p}$ and the diffusion time through the immobile layer $t_{diff} = L_z^{\,2}/(D_p / R_p)$ remains unchanged.

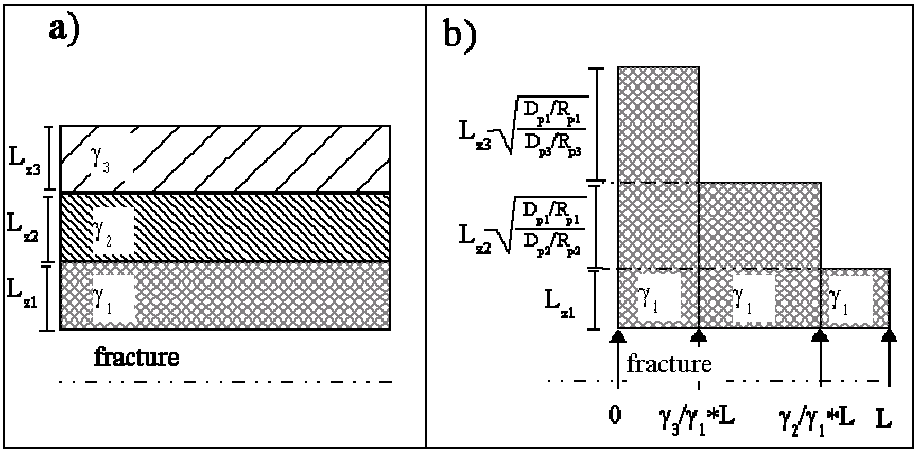

Figure 5-17. Layered immobile pore space along a flow path (a) is divided into a sequence of flow paths that have homogeneous immobile pore space (b).

The transport of tracer through a fracture that is surrounded by one layer of immobile pore space is calculated using an analytical model. It is based on a one-dimensional lattice walk in which the interaction of the solute between the mobile and immobile pore space is described by a waiting time distribution that is applied at the grid points (Cvetkovic and Haggerty, 2002). However, in our approach the waiting time distribution is calculated directly in the time domain, not in the Laplace domain, as was done by e.g. Cvetkovic and Haggerty (2002).

The flow path is represented by a 1D lattice. The discretisation is selected to be such that convergent results are achieved, but, on the other hand, that the calculation time is reasonable. Figure 5-5 shows that a flow path through both Type 1 and Type 2 features is represented by two legs that have symmetric matrix properties (i.e. the structure of the matrix is the same on either side of the fracture). Following the approach presented in Section 3.3.2, both of these two legs, which have layered matrix properties, are represented by a series of flow paths with homogeneous matrix properties (cf. Figure 5-17). This means that e.g. the first part of the Type 1 feature in Figure 5-5 is represented by a series of 3 flow paths (gouge, altered rock, intact rock) and the second part by a series of 4 flow paths (coating, cataclasite, altered rock, intact rock). This means that a flow path through a Type 1 feature should be represented by 7 successive legs. In the same way a Type 2 feature needs 5 successive legs.

5.4.3 Parameters

The transport parameters were based on data given mainly by Byegård and Tullborg (2004). Some data that were not given in the memorandum of Byegård and Tullborg (2004) were taken e.g. from the definition of the Äspö Task Force Task 6C (Dershowitz et al., 2003) or estimated on the basis of the data of other tracers. When calculating the retardation coefficients it was assumed that all geological materials have the same density of 2600 m^3/kg.

The sorption and diffusion data set applied in the calculations is presented in Table 5-3 and Table 5-4. Pore diffusivities calculated using porosity (Table 5-1) and diffusivity data (Table 5-4) are given in Table 5-5. In addition, Table 5-6 shows the calculated γ values for different layers and different tracers. It can be seen that the micro-structural model shown in Figure 5-5 really does exhibit a sequence of decreasing γ from the fracture surface to the inner parts of the matrix for all tracers.

Table 5-3. Sorption properties of geological materials (K_d [m^3/kg]) for different tracers. Data are mainly based on Byegård and Tullborg (2004). Other sources of data are indicated by footnotes.

	Fracture coating (d_{coat})	**Fault gouge (d_{goug}, concept A)**	**Cataclasite /Mylonite (d_{cata}, 20%)**	**Altered zone (d_{alt}, #19)**	**Altered zone (d_{alt}, BG1)**	**Intact wall rock (d_{rock})**
Uranine	0	0	0	0	0	0
Amino G	0	0	0	0	0	0
I	0	0	0	0	0	0
Tb-160	0	0	0	0	0	0
Sr	2.30E-04 [1)]	6.00E-04	1.40E-04	2.60E-05	2.60E-05	4.40E-05 [1)]
Rb	5.20E-03 [1)]	2.70E-03	4.00E-03	4.00E-04	4.00E-04	1.00E-03 [1)]
Cs	5.20E-02 [1)]	4.00E-02	3.00E-02	5.00E-04	5.00E-04	1.00E-03 [1)]
HTO	0	0	0	0	0	0
Eu-155	0	0	0	0	0	0
Na-22	2.00E-04	1.10E-04 [1)]	1.10E-05 [1)]	1.40E-05 [1)]	1.70E-06	7.10E-06 [1)]
Ba-133	2.72E-02	1.40E-02 [1)]	1.30E-03 [1)]	1.80E-03 [1)]	6.90E-04	8.80E-04 [1)]
Mn-54	1.70E-01	8.75E-02 [2)]	8.13E-03 [2)]	1.13E-02 [2)]	4.30E-03	5.48E-03 [2)]

[1)] Task 6C specification (Dershowitz et al., 2003).

[2)] Calculated on the basis of Ba-133, i.e. the ratio between K_d's of Mn-54 and Ba-133 is the same as for fracture coating.

Table 5-4. Diffusivities in free water, D_w [m^2/s] (Byegård and Tullborg, 2004).

	Fracture coating (d_{coat})	**Fault gouge (d_{goug}, concept A)**	**Cataclasite /Mylonite (d_{cata}, 20%)**	**Altered zone (d_{alt}, #19)**	**Altered zone (d_{alt}, BG1)**	**Intact wall rock (d_{rock})**
Uranine	5.00E-10	5.00E-10	5.00E-10	5.00E-10	5.00E-10	5.00E-10
Amino G	5.00E-10	5.00E-10	5.00E-10	5.00E-10	5.00E-10	5.00E-10
I	2.00E-09	2.00E-09	2.00E-09	2.00E-09	2.00E-09	2.00E-09
Tb-160	5.00E-10	5.00E-10	5.00E-10	5.00E-10	5.00E-10	5.00E-10
Sr	7.94E-10	7.94E-10	7.94E-10	7.94E-10	7.94E-10	7.94E-10
Rb	2.06E-09	2.06E-09	2.06E-09	2.06E-09	2.06E-09	2.06E-09
Cs	2.06E-09	2.06E-09	2.06E-09	2.06E-09	2.06E-09	2.06E-09
HTO	2.13E-09	2.13E-09	2.13E-09	2.13E-09	2.13E-09	2.13E-09
Eu-155	5.00E-10	5.00E-10	5.00E-10	5.00E-10	5.00E-10	5.00E-10
Na-22	1.33E-09	1.33E-09	1.33E-09	1.33E-09	1.33E-09	1.33E-09
Ba-133	8.48E-10	8.48E-10	8.48E-10	8.48E-10	8.48E-10	8.48E-10
Mn-54	6.88E-10	6.88E-10	6.88E-10	6.88E-10	6.88E-10	6.88E-10

Table 5-5. Pore diffusivities (D_p [m^2/s]) as calculated using D_w and porosities and formation factors given in Table 5-1.

	Fracture coating (d_{coat})	**Fault gouge (d_{goug}, concept A)**	**Cataclasite /Mylonite (d_{cata}, 20%)**	**Altered zone (d_{alt}, #19)**	**Altered zone (d_{alt}, BG1)**	**Intact wall rock (d_{rock})**
Uranine	6.20E-11	1.40E-10	2.45E-11	1.83E-11	1.83E-11	1.22E-11
Amino G	6.20E-11	1.40E-10	2.45E-11	1.83E-11	1.83E-11	1.22E-11
I	2.48E-10	5.60E-10	9.80E-11	7.33E-11	7.33E-11	4.87E-11
Tb-160	6.20E-11	1.40E-10	2.45E-11	1.83E-11	1.83E-11	1.22E-11
Sr	9.85E-11	2.22E-10	3.89E-11	2.91E-11	2.91E-11	1.93E-11
Rb	2.55E-10	5.77E-10	1.01E-10	7.55E-11	7.55E-11	5.01E-11
Cs	2.55E-10	5.77E-10	1.01E-10	7.55E-11	7.55E-11	5.01E-11
HTO	2.64E-10	5.96E-10	1.04E-10	7.81E-11	7.81E-11	5.18E-11
Eu-155	6.20E-11	1.40E-10	2.45E-11	1.83E-11	1.83E-11	1.22E-11
Na-22	1.65E-10	3.72E-10	6.52E-11	4.88E-11	4.88E-11	3.24E-11
Ba-133	1.05E-10	2.37E-10	4.16E-11	3.11E-11	3.11E-11	2.06E-11
Mn-54	8.53E-11	1.93E-10	3.37E-11	2.52E-11	2.52E-11	1.67E-11

Table 5-6. Matrix property γ [m/sqrt(s)] calculated for different tracers and different geological material. All tracers show a trend of decreasing γ from the fracture towards the inner parts of the matrix.

	Fracture coating (d_{coat})	**Fault gouge (d_{goug}, concept A)**	**Cataclasite /Mylonite (d_{cata}, 20%)**	**Altered zone (d_{alt}, #19 hydro Alt. 80%)**	**Altered zone (d_{alt}, BG1)**	**Intact wall rock (d_{rock})**
Uranine	3.94E-07	2.37E-06	4.95E-08	2.57E-08	2.57E-08	1.05E-08
Amino G	3.94E-07	2.37E-06	4.95E-08	2.57E-08	2.57E-08	1.05E-08
I	7.87E-07	4.73E-06	9.90E-08	5.14E-08	5.14E-08	2.09E-08
Tb-160	3.94E-07	2.37E-06	4.95E-08	2.57E-08	2.57E-08	1.05E-08
Sr	1.74E-06	8.02E-06	3.80E-07	1.13E-07	1.13E-07	8.24E-08
Rb	1.28E-05	2.59E-05	3.23E-06	6.86E-07	6.86E-07	6.25E-07
Cs	4.05E-04	9.81E-04	8.83E-05	7.67E-06	7.67E-06	6.25E-06
HTO	8.13E-07	4.88E-06	1.02E-07	5.30E-08	5.30E-08	2.16E-08
Eu-155	3.94E-07	2.37E-06	4.95E-08	2.57E-08	2.57E-08	1.05E-08
Na-22	2.12E-06	5.65E-06	1.58E-07	1.11E-07	5.51E-08	4.56E-08
Ba-133	1.88E-05	3.73E-05	1.18E-06	9.32E-07	5.78E-07	3.76E-07
Mn-54	4.23E-05	8.38E-05	2.66E-06	2.10E-06	1.30E-06	8.45E-07

5.4.4 Model variants

It is not possible to obtain direct information on the water residence time distribution along the tested flow paths. The non-sorbing and least diffusive tracers show characteristics of matrix diffusion in their deconvoluted response functions. This indicates that it is likely that all the breakthrough curves are affected by retention caused by matrix diffusion-type processes.

The predictions were made using a very simple model that is represented by an average flow rate in the transport calculations. In the evaluation, variable flow is taken into account. Again, quite a simple model is applied and the water residence time distributions of the two flow paths are represented by Gaussian distributions. The estimation of the WL/Q distribution is based on the Gaussian water residence time distributions. This is done by multiplying the water

residence time distribution by a constant factor, so that the resulting average WL/Q of the WL/Q distribution is a given value. In practice, this can be interpreted in such a way that the transport channel has a constant aperture and variable flow rate. The multiplying factor that is used to convert the water residence time distribution to a WL/Q distribution is the inverse of the effective retention aperture of the transport channel, indicating the equality $WL/Q = t_w/2b$.

Three different cases were calculated in the evaluation:

A The original BS2B micro-structural model coupled with a flow field that has an average WL/Q based on the measured flow rates at the injection locations (from the CPT-3C test)

B The same flow field as in Case A, but with increased thickness of the fault gouge

C Only altered rock and intact rock taken into account and increased WL/Q.

The same water residence time distribution was applied for each flow path in all cases. The applied water residence time distributions are the Gaussian distributions presented in Figure 5-18. The WL/Q distributions are calculated by dividing the water residence time distribution by the effective retention aperture. The effective retention aperture for Cases A and B is about $1.5 \cdot 10^{-4}$ m for Flow Path I and about $4.5 \cdot 10^{-4}$ m for Flow Path II. In Case C the aperture is about $4 \cdot 10^{-6}$ m for Flow Path I and $3 \cdot 10^{-5}$ m for Flow Path II (i.e. compared to Cases A and B the average WL/Q is 40 times larger for Flow Path I and 15 times larger for Flow Path II). The water residence time distribution applied in all the calculated cases was selected by the fitting of the Case B breakthrough curves.

The selection of the calculated variants in the evaluation is mainly guided by the information analysed from the measured breakthrough curves in Section 5.4.1 and presented in Figures 5-13 and 5-14.

Case A is regarded as a base case that uses the given micro-structural model and flow measurements. However, in the evaluation the flow field part was partly calibrated to average values of $WL/Q = 5 \cdot 10^7$ s/m for Flow Path I and $WL/Q = 8 \cdot 10^8$ s/m for Flow Path II. The local flow rate measurements of the CPT-3C test indicated $WL/Q = 10^8$ s/m for Flow Path I and $WL/Q = 3 \cdot 10^8$ s/m for Flow Path II. Flow Path II is composed of Type 1 (#19) and Type 2 (BG1) features. The estimated WL/Q values suggest that the total WL/Q is divided in such a way that 1/3 of the WL/Q is along Type 1 features and 2/3 along Type 2

ones. This ratio is maintained during the evaluation. Note that in the predictions Flow Path II is completely along a Type 1 feature. The reason is that in the prediction model (i.e. the WL/Q values and micro-structural model applied) the Type 1 features completely dominated the retention. Therefore, dropping Type 2 fractures from the simulations did not affect the retention, but sped up the calculations.

Case B is a variant that leans towards the effective material properties of the fault gouge as suggested by Figure 5-13. Case C is a variant that is based on the observed unlimited nature of the matrix diffusion (e.g. Figure 5-9 and Figure 5-10). This requirement is fulfilled by the altered zone, but this approach also requires the elimination of the fracture coating, fault gouge, and cataclasite from the micro-structural model and the enhancement of the *WL*/*Q*.

It is also possible to give a geometrical interpretation of the transport channels that are based on the average values of the *WL*/*Q* distributions. The approximate lengths of the flow paths and the injection flow rates of the BS2B experiment are 20 m and 5 ml/min for Flow Path I and 40 m and 2 ml/min for Flow Path II, respectively. The average widths of the flow paths are calculated to be about 21 cm for Flow Path I and 67 cm for Flow Path II ($WL/Q = 5 \cdot 10^7$ s/m for Path I and $WL/Q = 8 \cdot 10^8$ s/m for Path II). A variation of the flow field is also calculated in which the average WL/Q is 15 to 40 times larger. In this case the geometrical interpretation gives transport path widths that are of the order of 10 m, i.e. almost of the same order of magnitude as the length of the path.

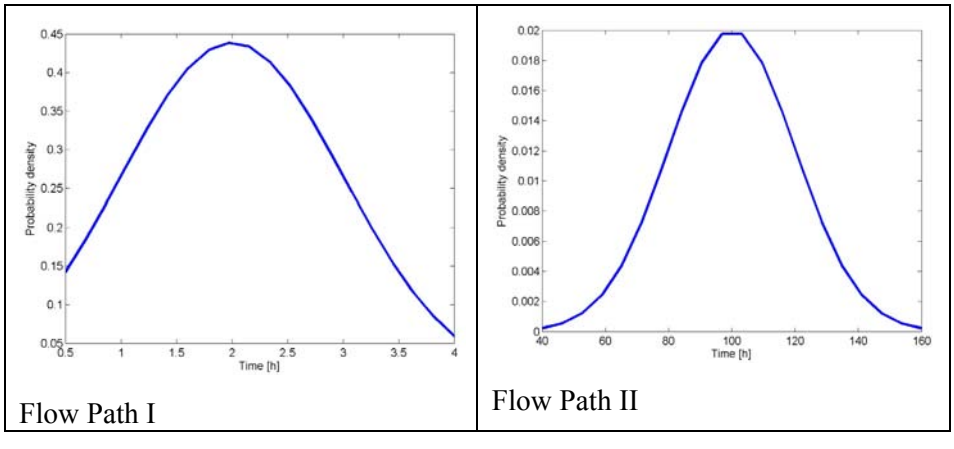

Figure 5-18. Water residence time distributions used in the evaluation of the BS2B experiment.

BS2B micro-structural model variant

In this model variant the breakthrough curves are calculated using the basic micro-structural model of the BS2B features (cf. Section 3.1.2) and a flow model that is based on the dilution flow measurements. The parameters used to calculate this case are presented in Table 5-7 and the resulting breakthrough curves are presented in Figure 5-19 and Figure 5-20, respectively. This is the base case of all the evaluation calculations. The two other cases are variations on this case in which either the micro-structural model or micro-structural model and flow field are altered.

It can be seen that in this model the retention takes place mainly in the immobile pore space, which has a very limited volume. This manifests itself in the results as a more Gaussian type of breakthrough curve. Only a small amount of the tracer mass is in the tailing of the breakthrough curve. Saturation of the fracture coating and fault gouge can also be seen in Figure 5-21, where the contributions of the individual layers to the total breakthrough curve are presented.

The calculated breakthrough curves for the strongly sorbing tracers clearly show later breakthroughs than the measured breakthrough curves. Much of the delay of the sorbing tracers is established in the fracture coating. Figure 5-21 shows the calculated contributions of the different immobile layers for a non-sorbing and sorbing tracer along both flow paths. Especially for Flow Path II (HTO and Mn-54), it can be seen that for Mn-54 the retention caused by the fracture coating is as strong as the retention caused by the fault gouge. For non-sorbing HTO the fault gouge causes much more retention than the fracture coating.

Table 5-7. Specification of the flow field and immobile pore space for the calculation Case A.

Case A	**Immobile zone:** According to the micro-structural model (Table 5-1, Table 5-3, and Table 5-4) **Water residence time distribution:** Flow Path I: Gaussian (mean 2.0 h, std 1.0 h) from about -1.5·std to 2·std Flow Path II: Gaussian (mean 100 h, std 20 h) from about -3·std to 3·std **WL/Q distribution:** Flow Path I: Gaussian (mean $4.8 \cdot 10^7$ s/m, std $2.4 \cdot 10^7$ s/m) from about –1.5·std to 2·std Flow Path II: Gaussian (mean $8 \cdot 10^8$ s/m, std $1.6 \cdot 10^8$ s/m) from about –3·std to 3·std, 2/3 of the WL/Q in BG1 and 1/3 in Structure #19

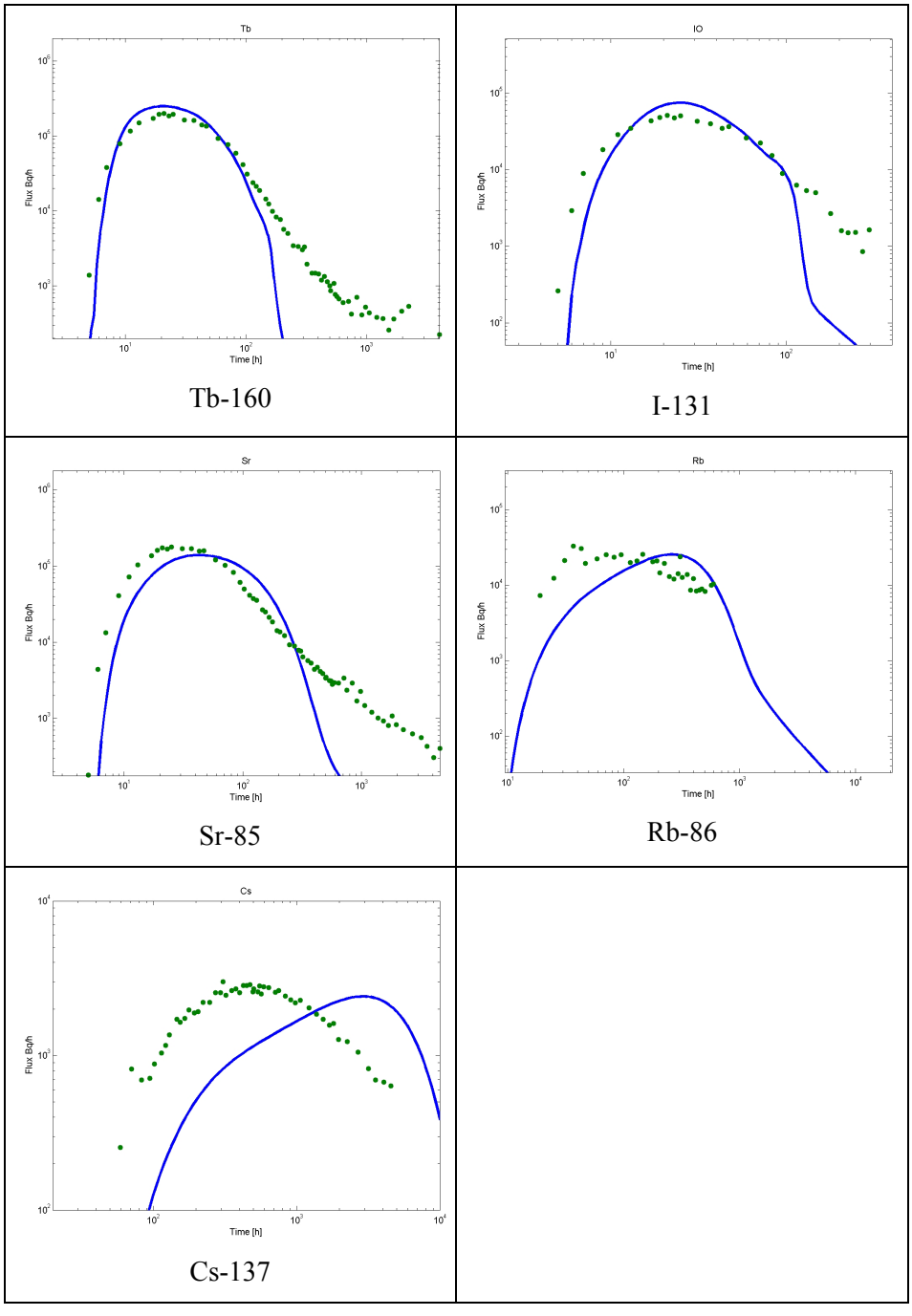

Figure 5-19. Measured (dots) and calculated breakthrough curves for Flow Path I. Breakthrough curves were calculated using the BS2B micro-structural model and a flow field as specified in Table 5-7.

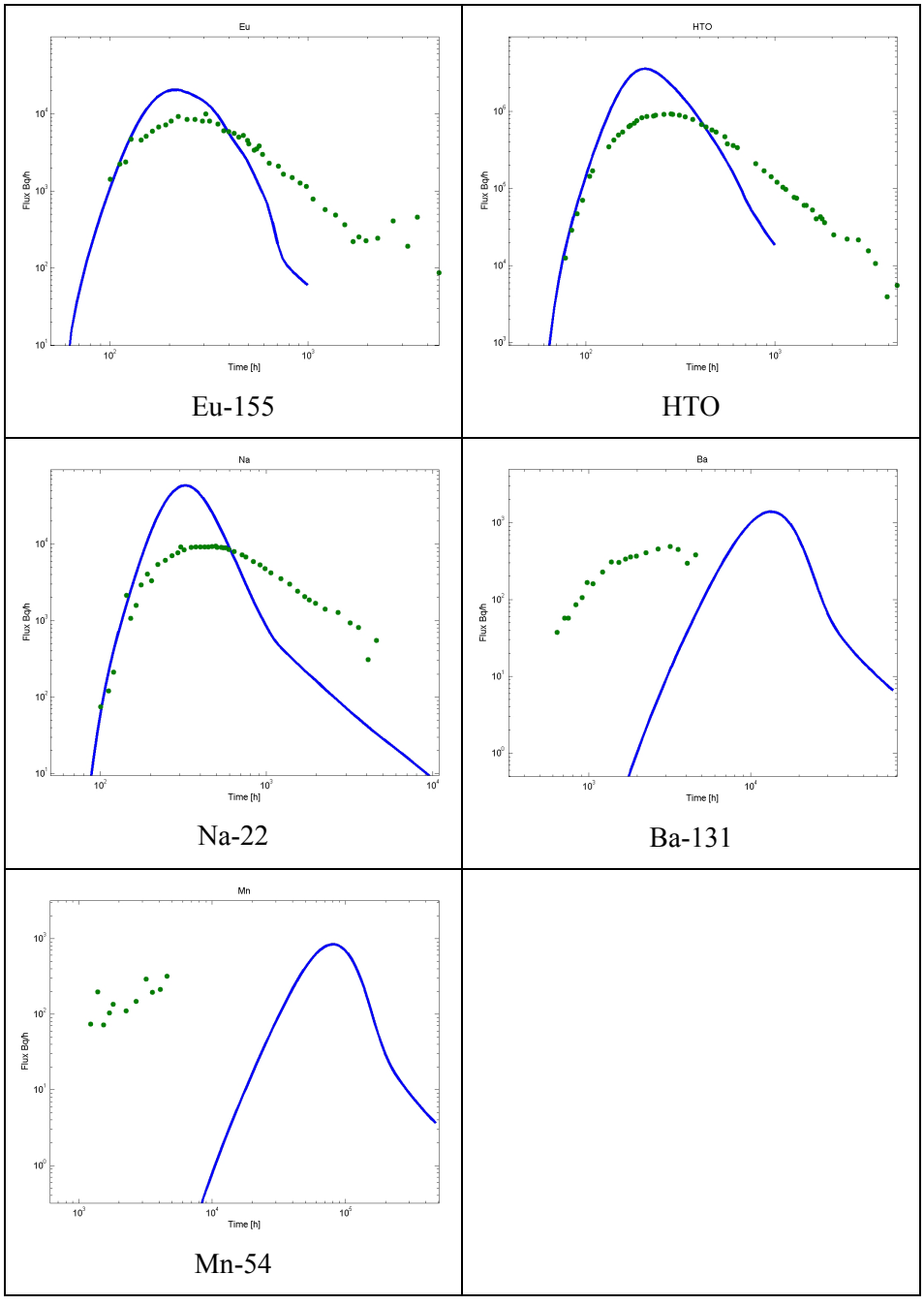

Figure 5-20. Measured (dots) and calculated breakthrough curves for Flow Path II. Breakthrough curves were calculated using the BS2B micro-structural model and a flow field as specified in Table 5-7.

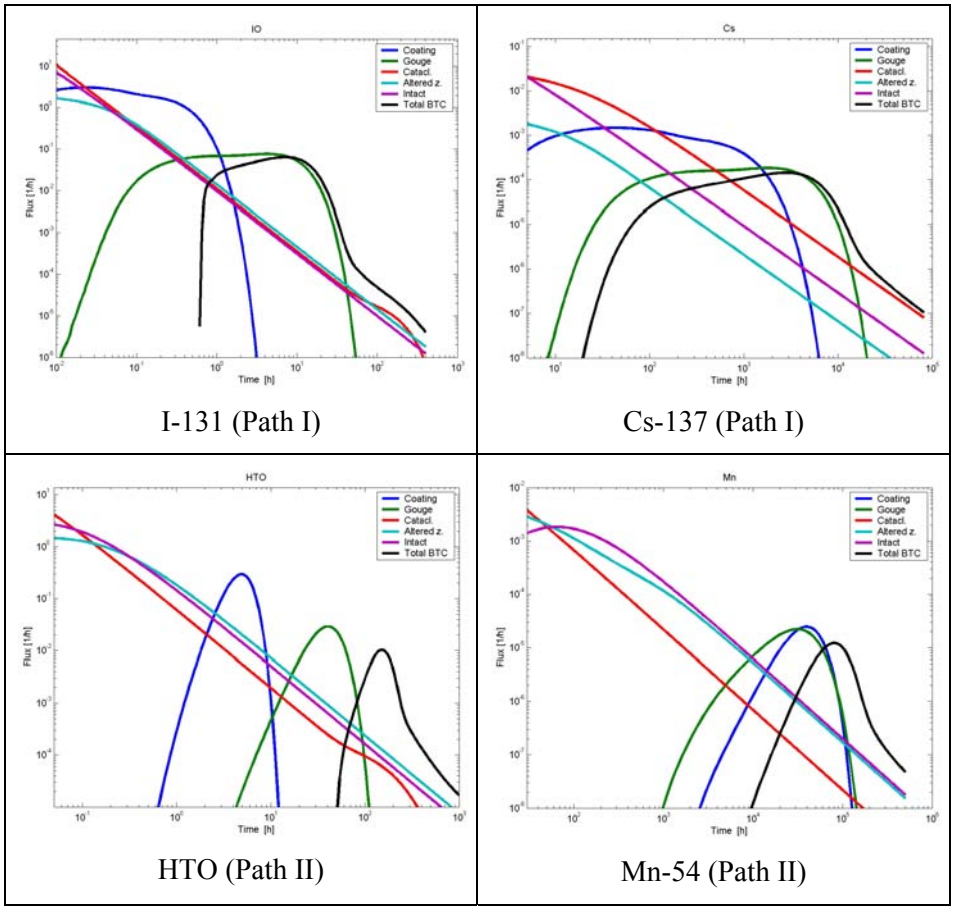

Figure 5-21. Contributions of the different immobile layers to the total breakthrough curve. These curves do not contain advective delay or the injection source term. The total breakthrough curve (black line) is a convolution of the individual contributions presented in these figures. One non-sorbing tracer and one strongly sorbing tracer were selected from both flow paths. It can be observed that the delay caused by the fracture coating, in particular, is more important for sorbing tracers.

Model variant for increased amount of fault gouge

The calculation of this case is motivated by the results presented in Figure 5-13. It suggests that an immobile zone that has properties close to those of a fault gouge can possibly explain the breakthrough curves. Another motivation is that in this case it is possible to use the flow field that was measured in the dilution experiment CPT-3C.

The measured breakthrough curves do not show clear signs of any limited extent of the major retention zone. The results of Case A show that the fault gouge (as defined in the BS2B micro-structural model) will get saturated by the tracers. Especially for Flow Path II, the modelled breakthrough curves (of Case A) are delayed Gaussian pulses that have minor elements of $\sim t^{-3/2}$ tailing.

Two variants of the BS2B micro-structural model are analysed here. First, all the layers of the BS2B micro-structural model are taken into account and the thickness of the fault gouge layer is increased from 3 mm to 6 cm. In the second alternative the fault gouge thickness is increased and the layer of the fracture coating is removed. The reason for omitting the fracture coating is that this thin layer of coating causes delays, especially for the more sorbing tracers. It seems that this kind of delay does not exist in the measured breakthrough curves. These two alternative micro-structural models for Type 1 fractures are presented in Figure 5-22.

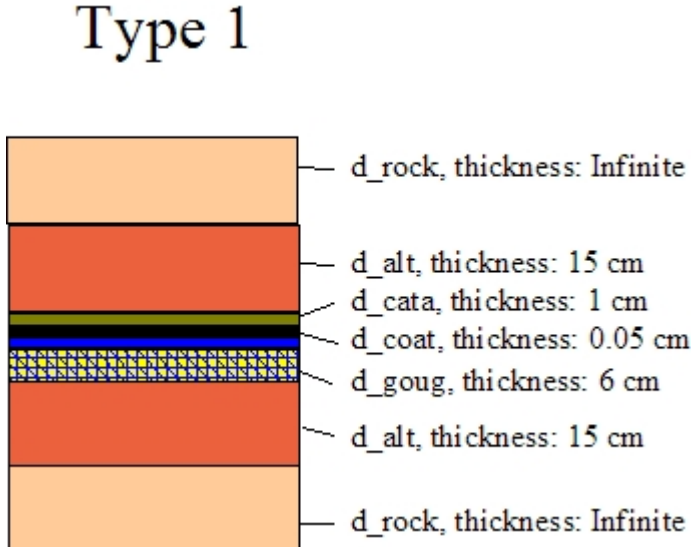

Figure 5-22. Alternative micro-structural model applied for Type 1 fractures in the Case B simulations. In the second variant of Case B the fracture coating was completely removed.

Simulated breakthrough curves for the alternative micro-structural model are presented in Figure 5-23 and Figure 5-24. It may be noted that the non-sorbing tracers HTO and Eu-155 show slightly different behaviour in their modelled breakthrough curves. The limited thickness of the 6-cm fault gouge causes the tailing of the modelled HTO breakthrough curve to rise at around 100 hours,

contrary to the measured breakthrough curve. The modelled Eu-155 breakthrough curve does not deviate from the measured breakthrough curve in the same way. The reason for the behaviour of the modelled breakthrough curves is the contrast between the applied pore diffusivities of Eu-155 and HTO. According to the BS2B micro-structural model, the diffusivity of HTO is over four times greater than the diffusivity of Eu-155. In the measured breakthrough curves the contrast between HTO and Eu-155 pore diffusivities seems not to be as large as it is in the BS2B micro-structural model. This is supported by the observation that in the measured breakthrough curves the times of the maxima of the breakthrough curves are quite close to each other. For the unlimited matrix diffusion the maximum of the breakthrough curve (δ-function release) is directly proportional to the pore diffusivity ($\sim u^2$ of Equation (5-2)). According to Table 5-2, the difference in u^2 between HTO and Eu-155 is about 1.8, whereas the factor is over four in the BS2B micro-structural model.

Clearly, a vertical 6-cm fault gouge layer is a problem. It is probably very hard to explain it from a geological point of view.

Table 5-8. Specification of the flow field and immobile pore space for Case B.

Case B	**Immobile zone:** Same as for Case A (Table 5-7), *but the thickness of the fault gouge is set to 6 cm instead of the 3 mm in the BS2B micro-structural model. In the second variant the fracture coating is also omitted (blue curves).* **Water residence time distribution:** Same as for Case A (Table 5-7). **WL/Q distribution:** Same as for Case A (Table 5-7).

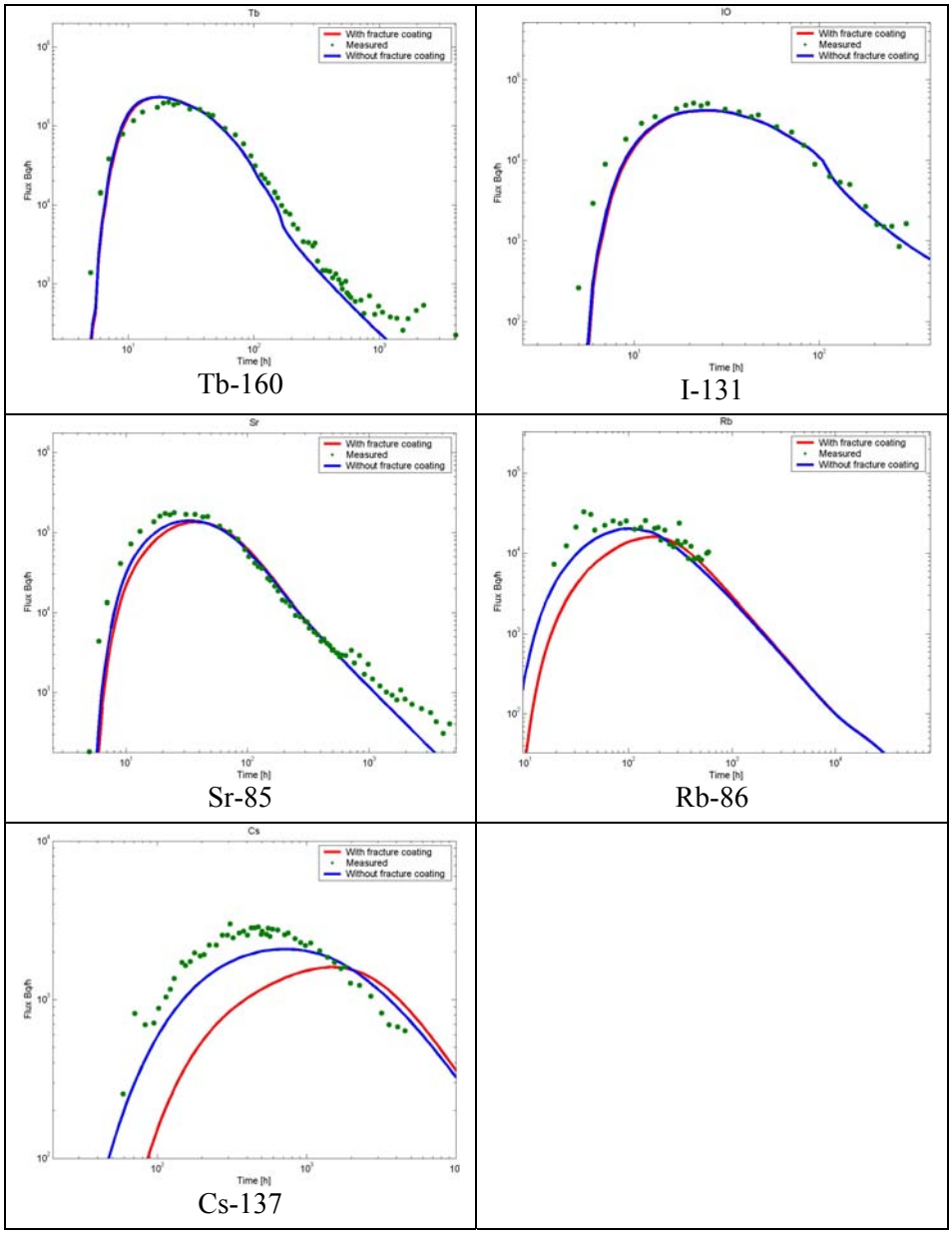

Figure 5-23. Measured (dots) and calculated breakthrough curves for Flow Path I. The breakthrough curves were calculated by retaining the flow field as measured by the dilution experiments (CPT-3C). This implies that the fault gouge is the principal retention zone. Red lines show the calculated breakthrough curves when all layers specified in the BS2B micro-structural model are taken into account. Blue lines show the breakthrough curves for the case where the fracture coating is omitted. Alterations to the BS2B micro-structural model and the applied flow field are specified in Table 5-8.

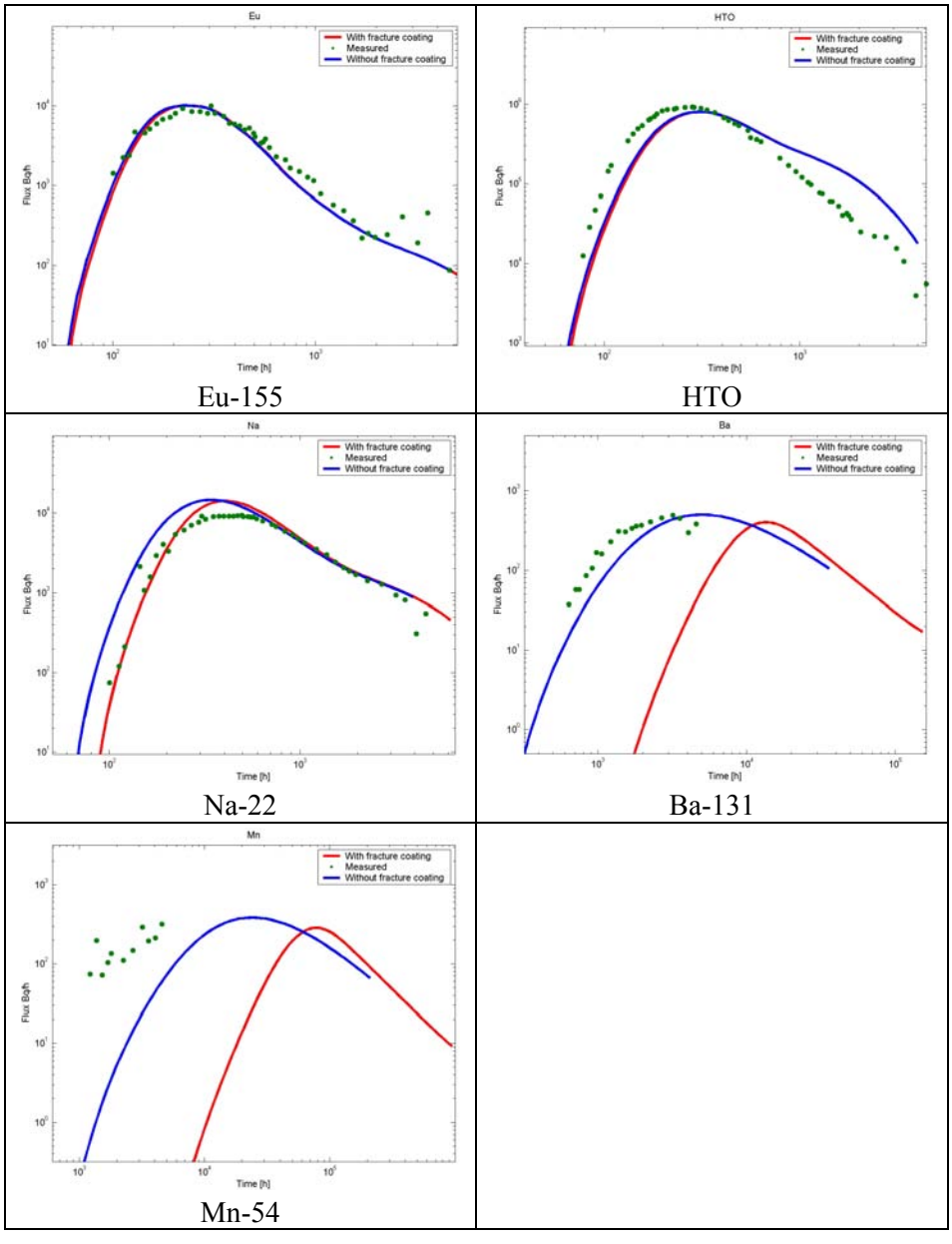

Figure 5-24. Measured (dots) and calculated breakthrough curves for Flow Path II. The breakthrough curves were calculated by retaining the flow field as measured by the dilution experiments (CPT-3C). This implies that the fault gouge is the principal retention zone. Red lines show the calculated breakthrough curves when all layers specified in the BS2B micro-structural model are taken into account. Blue lines show breakthrough curves for the case where the fracture coating is omitted. Alterations to the BS2B micro-structural model and the applied flow field are specified in Table 5-8.

Model variant of altered zone and intact rock only

The calculation of this model case is motivated by the observation that all the breakthrough curves can be explained by unlimited matrix diffusion (i.e. unlimited during the time scale of the experiment). This can be seen, for example, from the fitted results in Figure 5-11 and Figure 5-12. In these figures the response function of unlimited matrix diffusion is used to model the BS2B experiment and the fit to the measured breakthrough curves is good. The response functions of these breakthrough curves are specified in Table 5-2.

Simulated breakthrough curves for this model variant are presented in Figure 5-25 and Figure 5-26. The altered zone, as the primary retention zone, requires much stronger hydrodynamic control of the retention (WL/Q). The water residence time distribution is left unchanged but the average WL/Q is increased. In practice this means that the volume of the flow channel is fixed but the "geometry" of the flow channel is changed. The effective retention aperture is smaller and the flow is distributed over a wider area to balance the weaker matrix diffusion properties of the altered zone (compared to e.g. the fault gouge). In practice this requires quite a large change to the flow geometry. For Flow Path I the average WL/Q needs to be increased by a factor of 40 and for Flow Path II by a factor of 15. The resulting transport channel widths can be estimated by multiplying the widths of the transport channels for the base case by these same factors. For Flow Path I this means a width of the transport channel that is about 8.3 m and for Flow Path II one of about 10 m.

Table 5-9. Specification of the flow field and immobile pore space for Case C.

Case C	**Immobile zone:** Same as for Case A (Table 5-7) *but fracture coating, fault gouge, and cataclasite omitted.* **Water residence time distribution:** Same as for Case A (Table 5-7). **WL/Q distribution:** Flow Path I: As in Case A (Table 5-7) *but 40 times larger values* Flow Path II: As in Case A (Table 5-7) *but 15 times larger values*

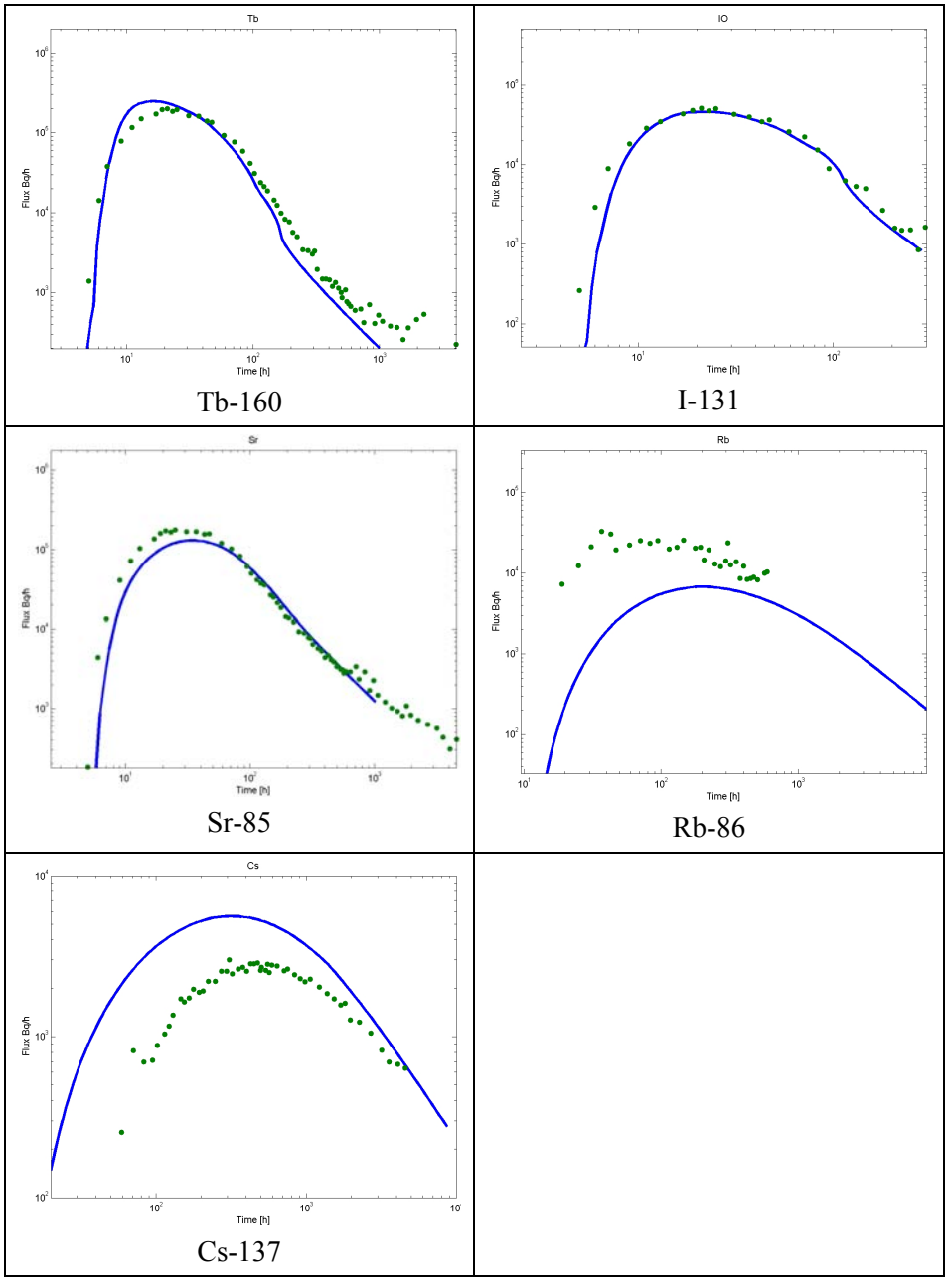

Figure 5-25. Measured (dots) and calculated breakthrough curves for Flow Path I. The breakthrough curves were calculated considering the zone of altered rock to be the principal retention zone. Alterations to the BS2B micro-structural model and the applied flow field are specified in Table 5-9.

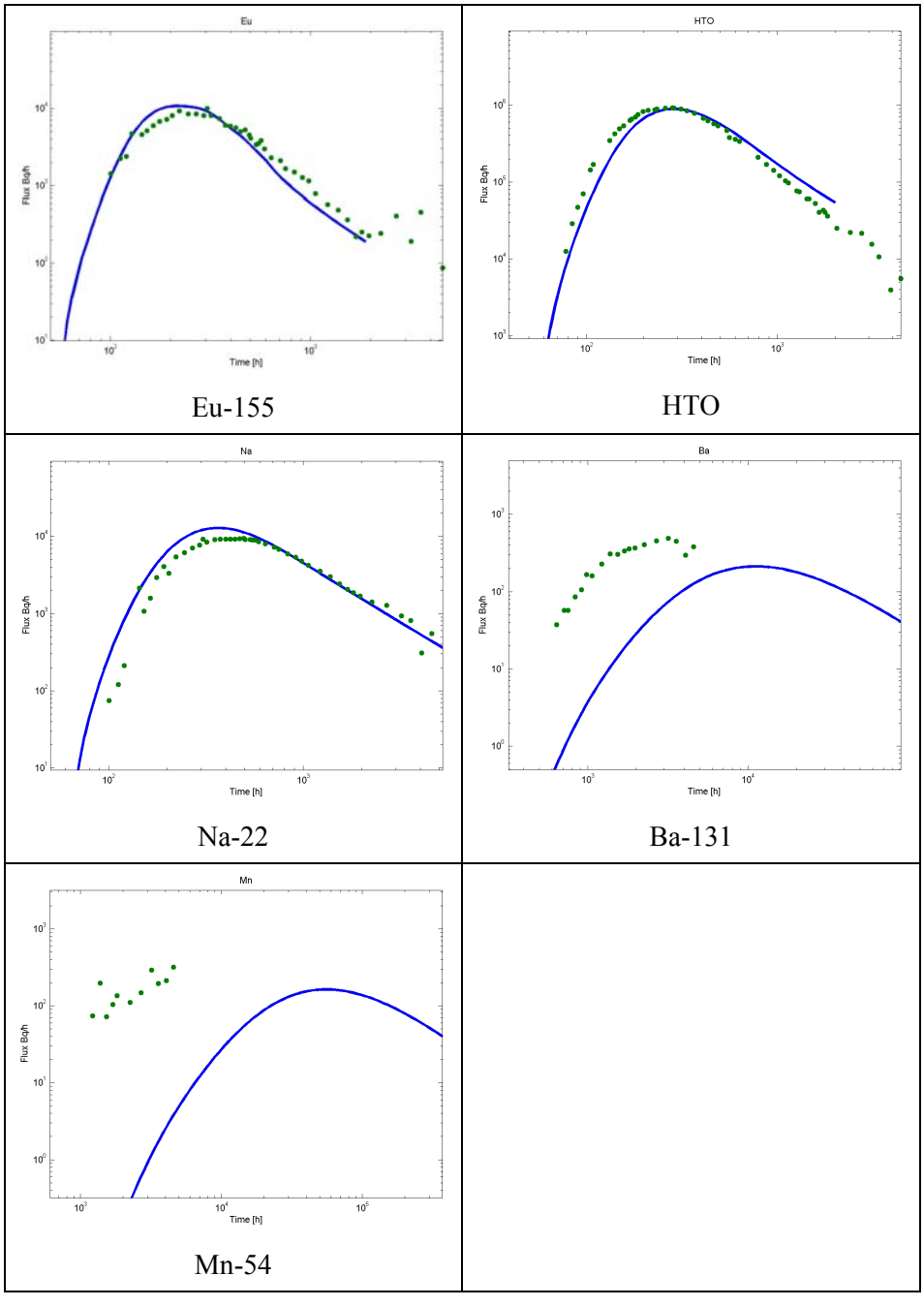

Figure 5-26. Measured (dots) and calculated breakthrough curves for Flow Path II. The breakthrough curves were calculated considering the zone of altered rock to be the principal retention zone. Alterations to the BS2B micro-structural model and the applied flow field are specified in Table 5-9.

5.5 Conclusions

The evaluation applied to the BS2B tracer tests did not aim at the calibration of the individual tracer K_d-values. The main emphasis was on the order-of-magnitude properties of the flow field and principal retention zones. This means that in the evaluation the K_d's were left unchanged compared to the values that were applied in the predictions; they are presented in Table 5-3. It would have been possible to obtain better fits for the sorbing tracers by fine-tuning the K_d's of the tracers.

One of the main findings of the evaluation is that according to the breakthrough curves it seems that the diffusion has taken place to an immobile zone that has a large volume. Matrix diffusion to a single unlimited immobile zone can explain the breakthrough curves very well (Section 5.4.1 and Table 5-2) and no clear signs of limited matrix diffusion can be seen in the breakthrough curves, although it is impossible to distinguish retention in a fully saturated immobile zone from equilibrium sorption.

The immobile zone retention properties along Flow Paths I and II can be directly compared by investigating the measured breakthrough curves. The fitted matrix diffusion parameter (u, cf. Table 5-2) for the non-sorbing tracers is about 1.5 $h^{1/2}$ along Flow Path I and from 8 $h^{1/2}$ to 11 $h^{1/2}$ along Flow Path II. If the effective immobile zone retention properties are equivalent along both flow paths, then the scaling of u should come solely from the scaling of the WL/Q. The statistics of the measured flow rates and roughly estimated path lengths are presented in Table 5-10. Table 5-10 presents a range of flow rates for Flow Path II that is based on the estimate by Andersson et al. (2004) that as a result of the problems with the equipment the real flow rate at the injection location of Flow Path II can be 10 times less than the measured value. Table 5-10 can be interpreted in such a way that the matrix diffusion is 5–7 times stronger along Flow Path II than it is along Flow Path I, but this requires 30 times greater hydrodynamic control of retention, i.e. the effective immobile zone retention property is clearly stronger along Flow Path I than along Flow Path II. This is also reflected by the evaluation of Case C, where the same immobile zone retention properties were applied along both flow paths. The required enhancement for the WL/Q is clearly bigger for Flow Path I, a factor of 40 compared to the factor of 15 for Flow Path II.

Table 5-10. Comparison of the flow paths based on the rough estimates of the path lengths and flow rates. On the basis of Andersson et al. (2004), the lower limit of the given flow rates for Flow Path II is considered more realistic.

	Length [m]	**Flow rate [ml/h]**	**WL/Q**	***u***
Flow Path I	20	68	-	-
Flow Path II	40	4.2–42	-	-
Ratio – FP II / FP I	2	0.062–0.62	3–30	5–7

The basic problem of the evaluation is that the retention depends on both the flow field and the material properties. The material properties are estimated on geological grounds and are presented as the BS2B micro-structural model. The flow field is measured locally at the injection borehole sections in the CPT-3C tracer dilution experiment. Calculations using the BS2B micro-structural model show that the breakthrough curves cannot be explained by directly combining the micro-structural model and measured flow field. Two alternatives to the base case were calculated. First, the flow field was kept unchanged and the material properties were changed. It appeared that the thickness of the fault gouge should be increased to 6 cm, mainly because of the HTO breakthrough curve for Flow Path II. In addition, the sorbing tracers indicate that the fracture coating does not exist, at least not in the way it is defined in the micro-structural model, or conceptualised in the evaluation model. The second alternative was calculated by changing both the flow field and the micro-structural model. In this case the principal retention zone was comparable with altered rock. The fracture coating, fault gouge, and cataclasite were omitted from this model. In this case the hydrodynamic control of retention (WL/Q) needs to be increased by a factor of 15 to 40. This corresponds to an effective transport aperture of about $4 \cdot 10^{-6}$ m for Flow Path I and $3 \cdot 10^{-5}$ for Flow Path II. If the geometry of the transport channel is represented by the average width of the channel applied in the WL/Q expression, then both channels need to be 8-10 m wide (they were 0.2 m to 0.7 m wide in the base case). The main features and outcomes of the evaluation models are summarised in Table 5-11.

Table 5-11. Main features and outcomes of the evaluation models.

Case	Features	Outcome
A	Immobile zones: BS2B micro-structural model. Flow field: CPT-3C dilution measurement flow rates.	Poor fits of the modelled BTC. Modelled BTCs do not have correct tailings. Partial saturation of the centimetre-scale immobile zones cause BTC peaks that are too narrow and high.
B	Immobile zones: BS2B micro-structural model + increased 6-cm thickness of gouge, one variant without fracture coating. Flow field: CPT-3C dilution measurement flow rates.	Acceptable fit to the measured BTC, especially without fracture coating. However, fit gets worse for more sorbing tracers (Note: Kd values not fitted). Tailings of the HTO still show some signs of partial saturation of the fault gouge (the power-law tailing rises and then declines steeply).
C	Immobile zones: Only altered zone and intact rock as defined in the micro-structural model. Flow field: CPT-3C dilution measurement flow rates decreased by a factor of 40 for Flow Path I and a factor of 15 for Flow Path II.	Acceptable fit to the measured BTC. Modelled BTC tailings follow experimental BTC tailings. Fit gets worse for more sorbing tracers (Note: Kd-values not fitted). The fit of Cs-137 BTC is particularly poor.

It is possible that for some of the tracers the tailing of the breakthrough curve is caused by processes that are not considered in this report. Section 5.4.1 shows that the injection curve of Cs-137 deviates from the behaviour of the other tracers and also from what is expected to be the tracer dilution curve in the injection borehole section. Similar behaviour on the part of the Cs (and also Rb) had already been observed in the TRUE Block Scale experiment. Andersson et al. (2002a) noted that it is possible to explain the power-law behaviour of the Cs in the injection curves by applying non-linear sorption with a Freundlich isotherm.

The evaluation modelling results and findings of the direct investigation of the measured breakthrough curves are best summarised by the following observations:

- Effective immobile zone retention properties are clearly stronger for Flow Path I. This supports the hypothesis that during the experimental time scale the effective immobile zone retention properties are stronger in a fault-type feature than in a non-fault-type feature.

- The character of the unlimited matrix diffusion in the breakthrough curves indicates that the major retention zone needs to be thick enough. This holds especially true for Flow Path II, which exhibits more retention. The evaluation model Case C assigns the retention to the altered zone (i.e. non-fault features) with a flow rate about 15 times smaller than the base case. This supports the note by Andersson et al. (2004) that the dilution flow measurement at the injection location of Flow Path II may show a flow rate 10 times too large as a result of problems with the equipment.
- Evaluation shows that very distinct layers of different materials on a centimetre scale (thickness of the material layer) should manifest themselves in the breakthrough curves of the non-sorbing tracers during the experimental period of BS2B.
- The effective immobile zone retention property for Flow Path I is between the properties of the fault gouge and cataclasite. For Flow Path II this property is close to that of the altered zone. This means that Flow Path I is characterised by fault-type features and Flow Path II is characterised by non-fault-type features.

It may be noted that definitive evidence that matrix diffusion is indeed an important retention process requires the employment of different flow rates along the same flow path to show that the dynamic behaviour of the tracer retention follows the expected behaviour of matrix diffusion.

The measured data do not show any major differences in the shape and tailing of the breakthrough curves for Flow Path I and Flow Path II. Both flow paths show features that are typical of matrix diffusion, namely the $t^{-3/2}$ tailing of the breakthrough curves. In addition, the breakthrough curves show a very good match with the model of unlimited matrix diffusion, which is also consistent with the sorption properties of the different tracers.

It is interesting that the unlimited matrix diffusion model explains the observed breakthrough curves so well. This indicates that the immobile layer causing the majority of the retention is quite thick, or that the contrast in the retention properties of the major immobile layers is small.

6. Summary

The time span of the single fracture tracer tests was over five years. The background flow field in the test volume changed during this period. The discharge borehole was at a higher hydraulic potential than the source boreholes during the first tracer tests. The head difference was reversed at the end of the last test. This could have had an influence on the geometry of the active flow path. The experimental data show a weak double peak breakthrough in the STT-1 test and a clear double peak breakthrough in the STT-2 test. The breakthrough curves indicate that two flow paths were active in STT-2 and that one flow path dominated in the STT-1 test. Both tests were performed between the same source and sink, but using a pumping rate in the STT-2 test that was half of the pumping rate of the STT-1 test. The differences in the hydraulic head of the background flow field between the source and discharge locations is of the order of one metre, compared to the drawdowns of about ten metres induced by the pumping during the tests. This indicates that the background flow field can be an important factor in an in situ tracer test and that changes in the strength of the sink easily lead to a completely different flow path. However, this does not suggest that variations in the background flow field are the major source of uncertainty in the modelling of the tracer tests. It shows that the flow paths in in situ conditions, even over a short distance in a single fracture, are sensitive and specific to the set-up configuration of the test. The modelling of the non-sorbing tracer tests performed earlier indicated that a radially converging flow field in a heterogeneous fracture leads to a single flow path in the majority of the simulations (Poteri and Hautojärvi, 1998). Therefore, it is possible that more than one fracture exists between the source and the sink, although the distance between the source and the sink is only a few metres. This shows that controlling the flow field in situ conditions is very challenging, especially if the same flow path needs to be tested using different flow rates.

The blind predictions of the tracer tests performed in a single fracture were based on the laboratory data on the retention properties of the rock matrix. The poor fit of the modelling results for the sorbing tracers showed that the unaltered rock matrix did not give an accurate description of the retention properties along the tested flow paths. This observation has important implications for the methods that should be used when laboratory data are applied in in situ transport modelling. It indicates that the immobile zone retention properties observed in the in situ tracer tests may not be directly applicable to the PA flow conditions.

Tracer tests in a single fracture were followed by experiments over several different fractures. Transport through a fracture network did not introduce new features to the breakthrough curves and the same model based on a concept of the transport channel was also applicable for the block scale tracer tests.

The modelling indicated that surface sorption, diffusion to the pore space of the fault gouge for the sorbing tracers, and diffusion to the stagnant zones for the non-sorbing tracers could explain the observed tracer retention. The relative importance of diffusion to the stagnant zones and fault gouge for the least sorbing tracers was not directly examined but the results indicate that diffusion to the stagnant pools of the flow field may also be important for the retention of the least sorbing tracers.

Alternative transport concepts were examined. The aim was to vary the parameterisation of the transport channels and retention parameters in order to find a consistent and feasible description that applies to all tracer tests simultaneously. The fitted channel apertures vary from 0.45 to 0.62 mm and the average channel width from 1.5 to 5.2 m, depending on the flow path. The flow field analysis carried out for the non-sorbing tracers gives the best results if the correlation length of the velocity variation is on the centimetre scale. On the other hand, diffusion to the stagnant zones gives reasonable retention for the least sorbing and non-sorbing tracers if the mean distance between the stagnant zones is about 2–5 cm. These two results are mutually consistent if it is assumed that the same phenomena produce both stagnant zones and velocity variation. For example, this phenomenon could be the channelling of the flow as a result of the spatial distribution of the gouge material in the fracture.

The influence of the heterogeneity of the immobile zones was revisited by repeating block scale tracer tests in a fracture network, but using another network of fractures. The conceptualisation of the immobile zone heterogeneities was supported by constructing conceptual models of the immobile zones for

faults and joints. The conceptualisation was based on geological observations and site-specific understanding of the hydraulic features.

Two different flow paths were tested. Flow Path I goes along a more heterogeneous fault-type fracture and Flow Path II also contains a less heterogeneous joint type of fracture. The measured data do not show any major difference in the shape and tailing of the breakthrough curves for Flow Path I and Flow Path II. Both flow paths show features that are typical for matrix diffusion, namely the $t^{-3/2}$ tailing of the breakthrough curves.

The breakthrough curves show rather a good match with a model of unlimited matrix diffusion, which is also consistent with the sorption properties of the different tracers. It is interesting that the unlimited matrix diffusion model explains the observed breakthrough curves so well. This indicates either that the active immobile retention layer is quite thick, or that the contrast in the retention properties of the major immobile layers is in reality smaller than in the conceptualised model of the immobile zones.

The modelling results also support the conceptual model of the immobile zones. Faults are parameterised to provide stronger retention and to be more heterogeneous than joints. The evaluated effective immobile zone retention properties are clearly stronger for Flow Path I, which goes mainly through fault-type fractures. The effective immobile zone retention property for Flow Path I is between the properties of the fault gouge and cataclasite. For Flow Path II this property is close to that of the altered zone of the rock matrix. This means that Flow Path I is characterised by fault-type features and Flow Path II is characterised by non-fault-type features.

Strong eveidence that matrix diffusion was the major retention process requires experiments along the same flow path using different flow rates. This makes it possible to examine the dynamic behaviour of the tracer retention when the flow conditions are changed and to compare that behaviour with the expected behaviour of the matrix diffusion. However, the TRUE tracer test campaign on detailed and block scales has shown that because of the background flow field it is almost impossible to maintain the same flow path when the pumping flow rate is changed.

The analysis of the transport and retention along the flow paths in a single fracture and in a network of fractures shows that increasing the complexity of the flow field and extending flow paths over several fractures does not introduce major new retention processes. The same retention processes that are applicable for a single fracture can also be applied for longer pathways that are composed

of several different fractures. Modelling of the tracer tests on a block scale indicates that this is the case even when the hydraulic structures along the flow path are geologically of different origin, as they were in the TRUE Block Scale Continuation project. Eventually, the retention properties are governed by the average properties along the flow path.

The evaluation of the tracer tests on different scales indicated that the heterogeneity of the immobile zone retention properties will affect the effective tracer retention properties. Tracer experiments on a scale of a few metres in a single fracture were performed by applying immobile zone retention properties that were parameterised by the properties of the undisturbed rock matrix. Clearly, undisturbed rock matrix does not provide as much retention as was observed in the tracer tests. The effects of the heterogeneity on the average retention properties along the flow paths were addressed in the modelling of the tracer tests in the TRUE Block Continuation projects. The modelling results showed that there is no straightforward way to assess average retention properties from the geological structure of the different immobile zones. Effective retention properties will depend on the flow field applied and they can be estimated through modelling.

The main outcome of the study is that the assessment of the in situ solute retention properties requires adequate information on the immobile zones and flow paths. Effective retention properties that have been estimated for a given tracer test set-up cannot be directly transferred to another flow field without considering how changes in the flow field will affect the contributions of the different immobile zones to the overall retention.

References

Andersson, P. 1996. TRUE 1st Stage Tracer Test Programme. Experimental data and Preliminary Evaluation of the TRUE-1 Radially Converging Tracer Test (RC-1). Äspö Hard Rock Laboratory. SKB Progress Report HRL-96-24.

Andersson, P. and Wass, E. 1998. TRUE 1st Stage Tracer Test Programme. Preliminary design tests for tests with radioactive sorbing tracers (PDT-1, PDT-2, PDT-3). Experimental description and preliminary evaluation. Äspö Hard Rock Laboratory Progress Report HRL-98-13.

Andersson, P., Nordqvist, R. and Jönsson, S. 1997a. TRUE 1st Stage Tracer Test Programme. Experimental Data and Preliminary Evaluation of the TRUE-1 Dipole Tracer Tests DP1-DP4. Äspö Hard Rock Laboratory. SKB Progress Report HRL-97-13.

Andersson, P., Nordqvist, R. and Jönsson, S. 1997b. TRUE 1st Stage Tracer Test Programme. Experimental Data and Preliminary Evaluation of the TRUE-1 Dipole Tracer Tests DP-1–DP-4. Äspö Hard Rock Laboratory. SKB Progress Report HRL-97-13.

Andersson, P., Byegård, J., Cvetkovic, V., Johansson, H., Nordqvist, R., Selroos, J.-O. and Winberg, A. 1997c. TRUE 1st Stage Tracer Test Program. Experimental Plan for Tests with Sorbing Tracers at the TRUE-1 Site. Äspö Hard Rock Laboratory. SKB Progress Report HRL-97-07.

Andersson, P., Johansson, H., Nordqvist, R., Skarnemark, G., Skålberg, M. and Wass, E. 1998. True 1st Stage Tracer Test Programme. Tracer tests with sorbing tracers, STT-1. Experimental description and preliminary evaluation. Äspö Hard Rock Laboratory. Technical Note TN-98-10t.

Andersson, P., Wass, E., Johansson, H., Skarnemark, G. and Skålberg, M. 1999a. True 1st Stage Tracer Test Programme. Tracer tests with sorbing tracers, STT-1b. Experimental description and preliminary evaluation. Äspö Hard Rock Laboratory. International Progress Report IPR-99-12.

Andersson, P., Wass, E., Byegård, J., Johansson, H. and Skarnemark, G. 1999b. True 1st Stage Tracer Test Programme. Tracer tests with sorbing tracers, STT-2. Experimental description and preliminary evaluation. Äspö Hard Rock Laboratory. International Progress Report IPR-99-15.

Andersson, P., Byegård, J., Holmqvist, M., Skålberg, M., Wass, E. and Widestrand, H. 2001. TRUE Block Scale Tracer Test Stage. Tracer tests, Phase C. SKB International Progress Report IPR-01-33.

Andersson, P., Byegård, J. and Winberg, A. 2002a. Final report of the TRUE Block Scale project, 2. Tracer tests in the block scale. SKB Technical Report TR-02-14. May 2002.

Andersson, P., Byegård, J., Dershowitz, B., Doe, T., Hermanson, J., Meier, P., Tullborg, E.-L. and Winberg, A. (eds.). 2002b. Final report of the TRUE Block Scale project, 1. Characterisation and model development. SKB Technical Report TR-02-13. April 2002.

Andersson, P., Gröhn, S., Nordqvist, R. and Wass, E. 2004. TRUE Block Scale Continuation, BS2 Pretests. Crosshole interference, dilution and tracer tests, CPT-1 CPT-4. SKB International Progress Report IPR-04-25.

Andersson, P., Byegård, J., Billaux, D., Cvetkovic, V., Dershowitz, W., Doe, T., Hermanson, J., Poteri, A., Tullborg, E.-L. and Winberg, A. (eds.). 2007. TRUE Block Scale Continuation project. Final Report. SKB Technical Report TR-06-42.

Bear, J., Tsang, C.-F. and Marsily, G. de (eds.). 1993. Flow and contaminant transport in fractured rock. Academic Press.

Becker, M.W. and Shapiro, A.M. 2000. Tracer transport in fractured crystalline rock: evidence of nondiffusive breakthrough tailing. Water Resources Research 2000 36(7):1677–1686.

Berkowitz, B. 2002. Characterizing flow and transport in fractured geological media: a review. Advances in Water Resources 2002 25:861–884.

Byegård, J. and Tullborg, E.-L. 2004. Proposed sorption, porosity and diffusivity properties for the prediction modelling of the TRUE Block Scale Continuation BS2B sorbing tracer experiment. Technical Memorandum, version 0.1, July 8, 2004, TRUE Block Scale Continuation.

Byegård, J., Johansson, H., Skålberg, M. and Tullborg, E.-L. 1998. The interaction of sorbing and non-sorbing tracers with different Äspö rock types. Sorption and diffusion experiments in the laboratory scale. SKB Technical Report TR-98-18.

Cacas, M.C., Ledoux E., de Marsily, G., Tillie, B., Barbreau, A., Durand, E., Feuga, B. and Peaudecerf, P. 1990a. Modeling fracture flow with a stochastic discrete fracture network: calibration and validation 1. The flow model. Water Resources Research 1990 26(3):479–489.

Cacas, M.C., de Marsily, G., Barbreau, A., Calmels, P., Gaillard, B. and Margritta, R. 1990b. Modeling fracture flow with a stochastic discrete fracture network: calibration and validation 2. The transport model. Water Resources Research 1990 26(3):491–500.

Cvetkovic, V. and Haggerty, R. 2002. Transport with multiple-rate exchange in disordered media. Phys. Rev. E, May 2002, Vol. 65, 051308.

Dershowitz, W., Winberg, A., Hermanson, J., Byegård, J., Tullborg, E.-L., Andersson, P. and Mazurek, M. 2003. Task 6C, A Semi-synthetic Model of Block Scale Conductivite Structures at the Äspö HRL. SKB, International Progress Report, IPR-03-13.

Hautojärvi, A. 1989. Dispersion in transport through fractures. Espoo, Finland: VTT Technical Research Centre of Finland, Nuclear Engineering Laboratory. Technical Report, TOKA-26/89.

Hautojärvi, A. and Taivassalo, V. 1994. The Intraval Project – Analysis of the Tracer Experiments at Finnsjön by the VTT/TVO Project Team. Nuclear Waste Commission of Finnish Power Companies. Report YJT-94-24.

Hermanson, J. and Doe, T. 2000. TRUE Block Scale Project Tracer test stage. March'00 structural and hydraulic model based on borehole data from KI0025F03. SKB, Äspö Hard Rock Laboratory. International Progress Report IPR-00-34.

Long, J.C.S. and Billaux, D.M. 1987. From field data to fracture network modeling: an example incorporating spatial structure. Water Resources Research 1987 23:1201–1216.

Mazurek, M., Jakob, A. and Bossart, P. 2003. Solute transport in crystalline rocks at Äspö – I: Geological basis and model calibration. Journal of Contaminant Hydrology 61:157–174.

Neretnieks, I. 1980. Diffusion in the rock matrix: An important factor in radionuclide retention? Journal of Geophysical Research, Vol. 85, No. B8, 4379–4397.

Nordqvist, A. 1995. Discrete modeling of solute transport in rock with variable aperture fractures. Doctoral Thesis. Division of Hydraulic Engineering, Department of Civil and Environmental Engineering. Stockholm, Sweden: Royal Institute of Technology.

Nordqvist, A.W., Tsang, Y.W., Tsang, C.F., Dverstorp, B. and Andersson, J. 1996. Effects of high variance of fracture transmissivity on transport and sorption at different scales in a discrete model for fractured rocks. J Contam Hydrol 1996 22:39–66.

Posiva Oy. 2008. Safety Case Plan 2008. Eurajoki, Finland: Posiva Oy. Report Posiva 2008-05.

Poteri, A. 2001. Modellling of the TRUE-1 sorbing tracer tests: Äspö Task Force, Task 4E and 4F. Svensk Kärnbränslehantering AB. SKB International Cooperation Report ICR-01-01.

Poteri, A. 2005. TRUE Block Scale Continuation project. Evaluation of the BS2B sorbing tracer tests using Posiva streamtube approach. Svensk Kärnbränslehantering AB. SKB International Progress Report IPR-05-36.

Poteri, A. 2006. Modelling of Task 6D, 6E, 6F and 6F2 using Posiva streamtube approach. Svensk Kärnbränslehantering AB. SKB International Progress Report IPR-06-17.

Poteri, A. and Hautojärvi, A. 1998. Modelling of the tracer tests in radially converging and dipole flow field in the first phase of the TRUE project, Task 4C-D. Äspö Hard Rock Laboratory. International Cooperation Report, ICR 98-03.

Rasmuson A. and Neretnieks I. 1986. Radionuclide transport in fast channels in crystalline rock. Water Resources Research 1986 22:1247–56.

Sahimi, M. 1995. Flow and transport in porous media and fractured rock: from classical methods to modern approaches. Weinheim, Germany: VCH.

Tsang, C.F., Tsang, Y.W. and Hale, F.V. 1991. Tracer transport in fractures: Analysis of field data based on a variable-aperture channel model. Water Resources Research 1991 27(12):3095–3106.

Tullborg, E.-L. and Hermanson, J. 2004. Assignment of distribution of geological structure type, complexity and parameters of the micro-structural model applicable to the predictive modelling of the BS2B sorbing experiment. Technical Memorandum, March 25, 2004. TRUE Block Scale Continuation.

Winberg, A. (ed.). 1996. First TRUE Stage. Descriptive structural-hydraulic Models on Block and Detailed Scales. SKB International Cooperation Report ICR 96-04.

Winberg, A., Andersson, P., Hermanson, J. and Byegård, J. 1998. First TRUE Stage. Updated Structural Model of the TRUE-1 Block and Detailed Description of Feature A. A technical memorandum prepared for the Äspö Task Force, Tasks 4E/4F. December 1998.

Winberg, A., Andersson, P., Hermanson, J., Byegård, J., Cvetkovic, V. and Birgersson, L. 2000. Äspö Hard Rock Laboratory, Final report of the first stage of the tracer retention understanding experiments. SKB Technical Report TR-00-07. March 2000.

Winberg, A., Andersson, P., Poteri, A., Cvetkovic, V., Dershowitz, W., Doe, T., Hermanson, J., Gómes-Hernández, J., Hautojärvi, A., Billaux, D., Tullborg, E.-L., Holton, D., Meier, P. and Medina, A. 2002. Final Report of the TRUE Block Scale Project. 4. Synthesis of flow, transport and retention in the Block Scale. SKB Technical Report TR-02-16.

Series title, number and report code of publication

VTT Research Notes
VTT-TIED-2464

Author(s)
Antti Poteri

Title

Solute transport and retention in fractured rock

Abstract

This work reviews and compiles the analysis of tracer tests that were performed in the Äspö Hard Rock Laboratory in Sweden over a period of several years. The tracer tests were carried out in fractured rock at a depth of about 400 metres below the ground surface. The experimental programme progressed from a simple flow path in a single fracture to multiple flow paths through a network of fractures.

The modelling of the tracer tests on different scales shows that matrix diffusion is an important retention process of solute transport in fractured rock. The tracer breakthrough curves show indications of the diffusive mass exchange between mobile and immobile zones, although in many cases in situ tracer tests should be performed under boundary conditions that favour advective solute transport.

The analysis of the flow paths in a single fracture and in a network of fractures indicates that an increase in the complexity of the flow field and extending flow paths over several fractures does not introduce new retention processes. The same retention processes that are applicable for a single fracture can be applied over longer pathways that are composed of several different fractures. Modelling the tracer tests on a block scale indicates that this is the case even when the hydraulic structures along the flow path are geologically of different origin. Ultimately, the retention properties are governed by the average properties along the flow path.

The main outcome of the study is that the assessment of in situ solute retention properties requires adequate information on the immobile zones and flow paths. The heterogeneity of the immobile zone retention properties affects the effective tracer retention properties. The retention properties estimated for a given tracer test set-up cannot be directly transferred to another flow field without considering how the changes in the flow field will affect the contributions of the different immobile zones to the overall retention.

ISBN
978-951-38-7262-5 (soft back ed.)
978-951-38-7263-2 (URL: http://www.vtt.fi/publications/index.jsp)

Series title and ISSN	Project number
VTT Tiedotteita – Research Notes 1235-0605 (soft back ed.) 1455-0865 (URL: http://www.vtt.fi/publications/index.jsp)	26021

Date	Language	Pages
February 2009	English, Finnish abstr.	141 p.

Name of project	Commissioned by
FEFTRA08	

Keywords	Publisher
solutes, transport, retention, flow path, bedrock, fractured rock, rock matrix, porosity, tracer tests, modelling, matrix diffusion	VTT Technical Research Centre of Finland P.O. Box 1000, FI-02044 VTT, Finland Phone internat. +358 20 722 4520 Fax +358 20 722 4374

Julkaisun sarja, numero ja raporttikoodi

VTT Tiedotteita
VTT-TIED-2464

Tekijä(t)
Antti Poteri

Nimeke

Aineiden kulkeutuminen ja pidättyminen rakoilleessa kalliossa

Tiivistelmä

Tässä työssä analysoidaan Äspön kalliolaboratoriossa Ruotsissa usean vuoden aikana tehtyjä merkkiainekokeita. Merkkiainekokeet suoritettiin rakoilleessa kalliossa noin 400 metrin syvyydellä. Merkkiainekokeissa tutkittiin erilaisia virtausreittejä rakoilleessa kalliossa alkaen virtausreiteistä pitkin yksittäistä vettäjohtavaa rakoa ja päätyen virtausreitteihin useiden rakojen muodostamassa rakoverkostossa.

Merkkiainekokeiden mallinnus osoitti, että matriisidiffuusio on tärkeä pidättymismekanismi aineiden kulkeutumisessa rakoilleessa kalliossa. Merkkiaineiden läpitulokäyristä voidaan tunnistaa piirteitä, jotka viittaavat diffusiiviseen vuorovaikutukseen virtaavan ja paikallaan pysyvän huokoisveden välillä. Useissa tapauksissa kokeet jouduttiin kuitenkin suorittamaan pumppausnopeuksilla, joissa advektiivinen kulkeutuminen oli hallitsevaa.

Yksittäisessä raossa ja rakoverkostossa tapahtuneen kulkeutumisen analysointi osoittaa, että monimutkaisempi virtauskenttä tai kulkeutuminen usean raon kautta ei sinällään aiheuta kulkeutumiseen uusia pidättymismekanismeja. Samoja pidättymismekanismeja voidaan käyttää kuvaamaan kulkeutumista sekä yksittäisessä raossa että useista raoista koostuvalla pidemmällä reitillä. Lohkomittakaavassa tehdyt merkkiainekokeet osoittivat tämän olevan mahdollista, vaikka raot olisivat geologiselta alkuperältään erilaisia. Perimmiltään pidättymisominaisuudet voidaan kuvata keskimääräisillä ominaisuuksilla koko reitille.

Työn päätulos on havainto, että aineiden pidättymisen arviointi vaatii riittävän yksityiskohtaista tietoa itse virtausreitistä ja huokoistilavuuksista kulkeutumisreitin varrella. Heterogeenisuus huokoistilavuuden ominaisuuksissa vaikuttaa efektiivisiin pidättymisominaisuuksiin. Yhdelle kokeelliselle virtauskentälle määritettyjä pidättymisominaisuuksia ei voi soveltaa toisiin virtausoloihin ilman, että erikseen arvioidaan virtauksen vaikutusta pidättymiseen eri huokoisvyöhykkeissä.

ISBN
978-951-38-7262-5 (nid.)
978-951-38-7263-2 (URL: http://www.vtt.fi/publications/index.jsp)

Avainnimeke ja ISSN	Projektinumero
VTT Tiedotteita – Research Notes 1235-0605 (nid.) 1455-0865 (URL: http://www.vtt.fi/publications/index.jsp)	26021

Julkaisuaika	Kieli	Sivuja
Helmikuu 2009	Englanti, suom. tiiv.	141 s.

Projektin nimi	Toimeksiantaja(t)
FEFTRA08	

Avainsanat	Julkaisija
solutes, transport, retention, flow path, bedrock, fractured rock, rock matrix, porosity, tracer tests, modelling, matrix diffusion	VTT PL 1000, 02044 VTT Puh. 020 722 4520 Faksi 020 722 4374

This work reviews and compiles the analysis of tracer tests that were performed in the Äspö Hard Rock Laboratory in Sweden over a period of several years. The tracer tests were carried out in fractured rock at a depth of about 400 metres below the ground surface. The experimental programme progressed from a simple flow path in a single fracture to multiple flow paths through a network of fractures.

The modelling of the tracer tests on different scales shows that matrix diffusion is an important retention process of solute transport in fractured rock. The analysis of the flow paths indicate that the same retention processes that are applicable for a single fracture can be applied over longer pathways that are composed of several different fractures. Modelling the tracer tests on a block scale indicates that this is the case even when the hydraulic structures along the flow path are geologically of different origin.

The main outcome of the study is that the heterogeneity of the immobile zone retention properties affects the effective tracer retention properties. The retention properties estimated for a given tracer test set-up cannot be directly transferred to another flow field without considering how the changes in the flow field will affect the contributions of the different immobile zones to the overall retention.

ISBN 978-951-38-7262-5 (soft back ed.)
ISSN 1235-0605 (soft back ed.)

ISBN 978-951-38-7263-2 (URL: http://www.vtt.fi/publications/index.jsp)
ISSN 1455-0865 (URL: http://www.vtt.fi/publications/index.jsp)